## DISCLAIMER

# Final Technical Report (FTR)

## Cover Page

| | | |
|---|---|---|
| ***a.*** *Federal Agency* | Department of Energy | |
| ***b.*** *Award Number* | DE-EE0009340 | |
| ***c.*** *Project Title* | Unified Universal Control and Coordination of Inverter-Based Resources, and Validation for a PV + Battery Hybrid Plant | |
| ***d.*** *Recipient Organization* | Florida State University | |
| ***e.*** *Project Period* | *Start:* 05/01/2021 | *End:* 4/30/2025 |
| ***f.*** *Principal Investigator (PI)* | Name: Hui "Helen" Li<br>Title: Provost McKenzie Professor<br>Email address: hli@caps.fsu.edu<br>Phone number: (850) 644-8573 | |
| ***g.*** *Business Contact (BC)* | Taylor Dearman,<br>Grants Officer<br>Sra-pre@fsu.edu<br>850-644-5260 | |
| ***h.*** *Certifying Official (if different from the PI or BC)* | Stacey Patterson<br>Vice President for Research SRA<br>Pre@fsu.edu<br>850-644-5260 | |

_____ _____

*Signature of Certifying Official* *Date*

*By signing this report, I certify to the best of my knowledge and belief that the report is true, complete, and accurate. I am aware that any false, fictitious, or fraudulent information, misrepresentations, half-truths, or the omission of any material fact, may subject me to criminal, civil or administrative penalties for fraud, false statements, false claims or otherwise. (U.S. Code Title 18, Section 1001, Section 287 and Title 31, Sections 3729-3730). I further understand and agree that the information contained in this report are material to Federal agency's funding decisions and I have any ongoing responsibility to promptly update the report within the time frames stated in the terms and conditions of the above referenced Award, to ensure that my responses remain accurate and complete.*

## Acknowledgement
This material is based upon work supported by the U.S. Department of Energy's Office of Energy Efficiency and Renewable Energy (EERE) and the Solar Energy Technologies Office under DE-FOA-0002243 (Topic Area 5.3: Control and Coordination of a Hybrid PV Plant) Award Number DE-EE0009340).



## Executive Summary:
As renewable energy deployment grows, hybrid power plants (HPPs) combining photovoltaic (PV) and battery systems must evolve to offer both energy and grid stability services. These systems typically include a mix of **grid-following (GFL)** and **grid-forming (GFM)** inverters, presenting unique coordination and control challenges. This Department of Energy–funded project developed and validated a **Unified Universal Control and Coordination (UUCC)** framework for such PV + battery hybrid plants, enabling seamless and stable operation, including **ultrafast black start**, **autonomous synchronization**, and **robust frequency and voltage regulation**, under different grid conditions.

The project significantly advanced the understanding of inverter-based resource (IBR) control by developing and validating **three complementary system-level approaches** for hybrid GFL/GFM operation:

1. A combined **Virtual Resistance (VR)-based GFL** and **Virtual Oscillator Control (VOC)-based GFM** method, where each inverter type is governed by a specialized control strategy. Together, these achieve stable, fast-response coordination, eliminating inrush current and enabling smooth black start and grid synchronization across a wide range of grid strengths.
2. A **Deadbeat-based UUCC strategy**, which uses discrete-time, switching-cycle-level control for both GFL and GFM inverters. This approach replaces traditional PI/PLL control with a control parameter-free, high-bandwidth framework that supports stable LVRT and instantaneous synchronization under all conditions.
3. A **benchmark comparison with Siemens' commercial GFM microgrid controller**, which provided a fast baseline platform. The commercial approach decoupled v & f control was implemented on a commercial microgrid controller.The baseline

commercial benchmark helped highlight superior transient response and black start performance offered by the deadbeat and VOC approaches.

These technical contributions offer substantial improvements over conventional inverter control schemes, which often rely on slow phase-locked loop (PLL)-based synchronization, require careful control parameters tuning, and prone to unstable in weak grids with GFL inverters and in stiff grid with GFM inverters therefore challenging for hybrid GFL+GFM under all grid conditions. The deadbeat-based UUCC framework enables simpler, faster, and more robust operation of hybrid IBR systems using wide-bandgap (WBG) devices such as SiC power semiconductors.

The rapid expansion of hybrid distributed energy resources (DERs), including residential and commercial PV-BESS installations such as Tesla Powerwall, PV with vehicle-to-grid (V2G) capability, and other integrated configurations, presents complex operational challenges for medium-voltage radial distribution feeders. These networks are subject to frequent disturbances such as faults, switching operations, rapid reclosing sequences, and feeder reconfigurations, all of which introduce dynamic stress on IBRs. In addition, planned feeder segmentation and deliberate islanding for resilience will require DERs that can autonomously perform blackstart, establish voltage and frequency references, and resynchronize with the main grid. The advanced deadbeat-based UUCC control and blackstart functionalities developed in this project directly address these requirements, enabling decentralized and autonomous operation of inverter-dominated DERs in distribution systems under a wide range of fault and reconfiguration scenarios.

From a public benefit perspective, these innovations enable more reliable and cost-effective integration of renewable energy into distribution networks. The ability to autonomously black start and stabilize grids under varying grid conditions support accelerates recovery from outages and support decentralized resilient energy systems. By reducing system complexity and improving performance, this project lays critical groundwork for future inverter-dominated power grids that are clean, reliable, and accessible to all.

## Table of Contents

## 1. Background:

### Limitations of Conventional Inverter Control

Traditional grid-following (GFL) control for inverter-based resources (IBRs) relies on phase-locked loop (PLL) mechanisms to synchronize inverter output with the grid voltage. This method, however, is inherently unsuitable for black start operations and loses control stability under weak grid conditions due to its dependency on an existing voltage reference.

Widely adopted grid-forming (GFM) approaches such as droop control and virtual synchronous machine (VSM) control offer better support for weak grids and islanded operation. Yet, these conventional GFM strategies often fall short in rapid system recovery scenarios, such as black start, due to slow voltage/frequency establishment, limited transient response, and challenges in stiff grid conditions. Their effectiveness frequently depends on complex and highly tuned control systems.

### Virtual Oscillator Control (VOC): Emerging Paradigm for GFM control

Virtual oscillator control (VOC) has emerged as a promising alternative, offering improved transient response and inherent stability by mimicking nonlinear oscillator dynamics to regulate inverter voltage and frequency. Representative VOCs include the Van der Pol oscillator [1], dead-zone oscillator [2], Andronov-Hopf oscillator [3], and Stuart-Landau oscillator [4]. VOC-based inverters achieve decentralized synchronization through oscillator coupling dynamics, removing the need for explicit communication protocols.

Dispatchable VOC (dVOC) [5], [6] enables active power sharing among multiple inverters through setpoint coordination. Unified VOC (uVOC) [7] improves grid compatibility by adjusting voltage control in both grid-connected and islanded modes. These developments demonstrate VOC's potential for black start, due to its fast dynamics and robust stability.

However, challenges remain. Breaker-closing events during black start can cause phase or voltage mismatches, triggering disturbances. Pre-synchronization strategies have been proposed [8] but often require manual switching and extra control loops. Our project advances VOC with a robust synchronization mechanism that eliminates manual intervention, enabling seamless, reliable operation during black start.

**Deadbeat-based Predictive Control: Transforming GFM and GFL control for SiC inverters with switching-cycle dynamics and large-signal stability**

Model predictive control (MPC), particularly finite control set (FCS-MPC) [9], [10], has been introduced in GFL inverters to enhance dynamic performance. However, variable switching frequencies and high computational burden make it less suitable for high-speed SiC inverters [11]. Deadbeat-based predictive control addresses these challenges. Prior work [12], [13] combines deadbeat MPC for current loops with PLL-based PI outer control. PLL-less methods [14], [15] are promising but limited to single-inverter systems with simple models. We propose a deadbeat-based GFL control for multiple paralleled inverters, supporting low-voltage ride-through (LVRT) and resilient performance in weak grids, without requiring PLL or precise parameter tuning.

In GFM applications, MPC has been integrated to enhance dynamic response in PSL-based systems [16], [17] and to improve transient stability [18]. Efforts to hybridize MPC with oscillator-based methods (e.g., Andronov-Hopf dVOC) [19] have seen MPC used merely as a supplementary mechanism. As such, traditional weaknesses in GFM systems — slow recovery and fragile robustness — persist. Our proposed deadbeat control approach resolves these shortcomings by embedding fast predictive control at the core of the inverter operation, enabling ultrafast black start, LVRT, and stable performance even in stiff grid scenarios.

Our proposed deadbeat method revolutionizes GFL and GFM control for SiC inverters by, for the first time, achieving both switching-cycle dyamics (including ultrafast black start) and large-signal stability under LVRT event and different grid condition without requiring control parameter tuning - even for multiple paralleled inverters, which has never been achieved by existing methods.

**Virtual Resistance-Based (VR) Methods: Damping and Robust Stability**

Virtual resistance (VR)-based methods, derived from virtual impedance control, offer improved harmonic damping and robustness. Prior VR implementations [20] focused on power sharing, but did not address weak grid scenarios. Active damping [21], [22] and auto-tuning approaches [23] rely on accurate resonance identification and parameter tuning, which are vulnerable to time-varying system conditions.

Our VR approach in this research project overcomes these issues by damping harmonics irrespective of frequency and enhancing system passivity. Key benefits include independence from PCC voltage sensing, reduced reliance on bulky inverter inductors, and elimination of PLL. The inverter remains capable of grid synchronization with fast response and minimal steady-state error.

**Commercial Approaches**

As a baseline comparison, this research also included demonstration of Siemens proven methodologies validated in previous work. Specifically, Siemens deployed a similar black start scheme in the DOE SETO-sponsored AURORA project [24] (SETO AURORA), testing grid-forming functions with 24 inverters across microgrid fleets. In other microgrid projects, such as the Princeton Resilient Campus [25] and the Galapagos Island Microgrid [26], Siemens grid-forming and black start technologies have been operating successfully for years, demonstrating high reliability and resilience in field deployments. These

approaches were used as baselines in this research project to compare performances of the newly developed controllers.

## 2. Project Objectives:

**Impact:**

This project significantly advances the national goals for clean energy transformation, grid modernization, and economic resilience. By enabling ultrafast, autonomous black start and GFM functionality in hybrid PV + battery systems, the proposed methods increase power system flexibility and security. These developments also facilitate the transition toward 100% renewable energy targets and support disaster resilience for critical infrastructure such as those operated by the City of Tallahassee (COT). The resulting technologies will be scalable for broader adoption across U.S. utilities. Specifically, the project developed multiple universal unified control and coordination (UUCC) methods that enable existing PV power plants to provide GFM functionality. Two methods represent major advancements and breakthroughs in control strategies for grid-tied inverters, while a third has been successfully implemented on a commercial microgrid controller. These methods collectively improve the operational flexibility, stability, and resilience of hybrid PV + battery systems, demonstrating both technical feasibility and industry readiness. The developed methods were successfully tested on lower-power hardware setups, including a commercial industrial microgrid controller. These experiments provided critical evidence for the proposed hybrid PV + battery technologies and demonstrated their potential for future deployment in full-scale utility systems. In the near term, the project supports COT's efforts to enhance energy security, reduce costs, increase disaster preparedness, and meet their goal of 100% renewable energy by 2050. The solutions developed are broadly transferable, offering significant impact for utilities nationwide.

**Project Goals:**

The overarching goal of this project is to develop an innovative control and coordination framework for inverter-based resources (IBRs) in photovoltaic (PV) + battery hybrid power plants. The framework—referred to as Unified Universal Control and Coordination (UUCC)—is designed to enhance system flexibility and stability across a wide range of operating conditions, including grid-connected, grid-isolated, and grid-forming modes.

To achieve this goal, the project is organized around the following key objectives:

(1) **Design and validate the UUCC architecture**, including inner-loop and outer-loop control strategies, along with a comprehensive stability assessment, by the end of Budget Period 1 (BP1);

(2) **Develop and demonstrate ultrafast black start algorithms** for PV + battery hybrid systems, integrating the full suite of control strategies in a laboratory environment during Budget Period 2 (BP2);

(3) **Develop representative use cases and implement the UUCC control strategies in both simulations and hardware testbeds**, including system-level modeling and validation of PV + battery hybrid plants. Validate the control approaches using both a dedicated laboratory-scale testbed and commercial microgrid controllers, providing a practical foundation for future scaling and industry adoption.

**Expected Outcomes:**

1. **Advanced Grid-Forming and Grid-Following Control Development**
   Development of robust, unified control strategies for PV + battery hybrid power plants capable of seamless transitions between grid-following and grid-forming modes. The control methods will meet the following performance targets:
   a. **Ultrafast Black Start Capability**
      - ≤0.2 seconds to energize local critical loads (including combinations of constant impedance, current, and power loads totaling 20–60% of inverter capacity)
      - ≤0.5 seconds to establish stable voltage (0.917–1.05 p.u.) and frequency (59.5–60.1 Hz) setpoints and enable loading above 60% of inverter capacity
      - ≤1 second to resynchronize and reconnect to the main grid

   b. **Robustness Across Grid Conditions**
      - Stable inner-loop voltage and current control performance across a wide grid impedance range (2%–20%)
      - Resilient operation during low-voltage ride-through events

   c. **Tight Voltage and Frequency Regulation**
      - Steady-state voltage error <5% and frequency error <1% under grid-forming operation
      - Transient voltage error <20% and frequency error <5%
2. **Simulation and Laboratory Validation**
   Demonstration of the proposed control strategies through detailed simulations and proof-of-concept hardware testing on dedicated laboratory-scale testbeds and commercial microgrid controllers.
3. **Comprehensive Technical Documentation**
   A final report documenting the developed control strategies, simulation results, case studies, lab test results, and comparative assessments.
4. **Quarterly Progress Reporting**
   Timely submission of quarterly technical and financial progress reports throughout the project duration.
5. **Project Dissemination and Knowledge Transfer**
   Presentation and publication of results through peer-reviewed papers, conference proceedings, and outreach to relevant industry and utility stakeholders.

**Significance, innovation, and fundamental advances**

This project delivers foundational innovations in control, coordination, and operational readiness for hybrid photovoltaic (PV) and battery energy storage plants using inverter-based resources (IBRs). It directly addresses key limitations in the current grid modernization landscape—namely, the lack of fast, black start capability, limited interoperability between grid-forming (GFM) and grid-following (GFL) inverters, and high complexity in achieving seamless operation when different sources are present, such as battery and PV.

The central innovation is the development of a **Unified Universal Control and Coordination (UUCC)** framework that enables hybrid plants to function across the full

spectrum of grid-tied, islanded, and transitional operating conditions, offering a high degree of flexibility, robustness, and control stability.

**Key Advances and Technical Contributions:**

- **Breakthrough in Black Start Speed**:
  The UUCC-based methods achieved **ultrafast black start** capability with stable voltage establishment in under **0.2 seconds** and full synchronization—including load pickup and grid connection—within **1 second**, even when using **multiple inverters operating in hybrid GFM and GFL modes**.
  By comparison, commercial inverter solutions—even when augmented with advanced research-level configurations—exhibited black start times exceeding **5 seconds** under standalone conditions and were unable to achieve coordination in multi-inverter scenarios without significant instability. In fact, in common operation conditions, the proposed approach enables a **10x improvement in black start speed**, a transformational shift with major implications for grid resilience and disaster recovery.
- **Seamless GFM-GFL Coordination in Hybrid Plants**:
  The project introduced a novel **deadbeat-based control scheme**, allowing instantaneous synchronization and stable parallel operation of multiple SiC inverters with diverse roles. This control enabled real-time transitions between GFM and GFL operation, eliminating voltage and current overshoots during synchronization transients. These advances are critical for practical deployment in hybrid PV + battery systems, where inverter roles may dynamically change depending on system conditions, storage availability, or fault response needs.
- **Inrush-Free Transformer Energization via Pre-Fluxing Control**:
  A new method was developed for **instant transformer energization** by inverter-based sources using **pre-fluxing control**. The method ensures zero inrush current and energization within milliseconds, addressing a major historical weakness of IBRs relative to synchronous machines.
  This technique enables direct black start of medium-voltage systems and critical infrastructure with no additional hardware or protective relays, making it highly suitable for field deployment.
- **Predictive Synchronization Without Output Current**:
  Enhancements to virtual oscillator control (VOC) using **predictive current feedback** allow synchronization with the grid even without existing current output. This is especially important for black start, where grid references are absent, and establishes a fast and stable connection point with minimized bus voltage sag and inrush current.
- **Built-in Low-Voltage Ride-Through (LVRT) and Current Limiting**:
  The deadbeat control design includes embedded mechanisms for **current limiting and LVRT**, eliminating the need for mode-switching logic under fault conditions. This simplification improves control reliability and system safety, especially during grid disturbances.
- **Validation of Feasibility through Hardware and Commercial Controllers**:
  The proposed strategies were validated through:
  - **Dedicated lab-scale hardware testbeds** (≤20 kW) specifically constructed for this project;

- **Commercial microgrid controller platforms**, where black start coordination was benchmarked;
- **System-level simulations** representing real-world PV + battery hybrid configurations.

Together, these innovations constitute a **fundamental shift in the role and capability of inverter-based hybrid systems**, enabling them to perform essential grid services once reserved for synchronous generation. The technologies developed lay the groundwork for **fast, autonomous, and resilient restoration of critical loads**, making them especially impactful for grid modernization, renewable integration, and disaster preparedness.

Moreover, the generalizable nature of the UUCC architecture and its compatibility with both commercial and research platforms ensures **broad scalability** across U.S. utilities. As such, the work directly advances national objectives for clean energy transformation, power system resilience, and the safe integration of high-penetration renewables.

**Tasks and Milestones**

| Task | *Description* |
|---|---|
| **Task 1** | Inner-loop controller design -both software and hardware developments, their performance validation, and stability assessment<br>**M 1.1.1**: IBR system follows reference (current/voltage/frequency) within 20ms response time, 5% error for current and voltage over wide 3%-30% grid impedance variation range under the worst-case scenario of no interface inductor/filter.<br>**M 1.1.2**: Inner-loop controller is able to follow reference (current/voltage) operating under 100% load step change, and 0-10% IBR interface impedance.<br>**M 1.1.3**: UUCC's inner-loop controller stability assessment under various quantitative grid conditions. |
| **Task 2** | Outer-loop controller design, implementation, and stability assessment<br>**M 1.2.1**: Model captures a large (>90% uncertainty range or X/R's values from 3 to 30) variation in X/R from small-scale distribution-level realistic model to large-scale transmission-level realistic model.<br>**M 1.2.2**: Design the outer-loop controller based on the developed model in 1.2.1, develop a fault disturbance scenario to verify the voltage response of the controller and develop a load increase (or decrease) scenario to verify the frequency response of the controller.<br>**M 1.2.3**: Assessment of developed controller stability at distribution system level via case studies in a high-fidelity model. |
| **Task 3** | Energy management controller design and development.<br>**M 1.3.1**: Create 20-MW scale economic cost models that utilize different battery chemistries, DOD, operating temperatures.<br>**M 1.3.2**: Showing > 5% cost reduction at least in one typical operation scenario compared to typical rule-based energy scheduled controllers. |
| **Task 4** | Control and use-case development on 1-MW at-scale test platform.<br>**M 1.4.1**: Controller architecture identified and full control integration pathway defined. |
| G/NG | 1. Inner-loop controller design; 2. Outer-loop controller design |
| **Task 5** | UUCC's inner-loop control implementation and lab validation.<br>**M 2.5.1**: Grid-tied inverter hardware and inner-loop controller software implementation.<br>**M 2.5.2**: UUCC's inner-loop controller lab validation under 3%-30% distribution system impedance, 100% load changes. |
| **Task 6** | Develop black start functions for hybrid plant. |
| **Task 7** | Ultrafast black start of PV + battery hybrid power plant. |

| | |
|---|---|
| | **M 2.7.1**: Simulation validation of a hybrid plant picking up local loads within the capacity of the plant, and establishing acceptable voltage (within 0.917 - 1.05 p,u,) and frequency (within 59.5 – 60.1 Hz) set points.<br>**M 2.7.2:** Simulation validation of a hybrid plant synchronized and reconnected to a realistic distribution/sub-transmission system.<br>**M 2.7.3**: Implement UUCC's outer-loop black-start control algorithm on microgrid controller for hybrid plant.<br>**M 2.7.4**: Black start hardware and software implementation. |
| **Task 8** | Evaluation of developed controls and ultrafast black start.<br>**M 2.8.1**: PV plus battery model is developed and modified to integrate inner and outer control layers. Developed controls are evaluated on at-scale plant model on a digital platform. |
| **Task 9** | Control integration for lab validation.<br>**M 2.9.1**: Lab validation of integrated energy schedule controller, outer-loop and inner-loop controller. |
| **Task 10** | Lab HPP validation and evaluations.<br>**M 2.10.1**: Individual system controllers developed are integrated with the controllable grid interface. |

NOTE: Following the project potential assessment at the end of BP1, DOE decided to focus the remaining work on innovations in fast control, stability under disturbances, seamless reconfiguration, black start under load, and other challenges of the real-world medium voltage distribution systems. By mutual agreement, further work on the technoeconomic analysis and MW-scale plant controller work of Task 3 and Task 4 was discontinued, Task 5 was modified with more aggressive success metrics, Task 7 was added, and Tasks 9 and 10 were modified. For completeness, partial results of discontinued Tasks 3 and 4 are reported below.

## 3. Project Results and Discussion:

### 3.1 High-level comparison of anticipated outcomes and realized results

| | Anticipated Outcomes | Realized Results |
|---|---|---|
| Stability adaption | Guaranteed inner-loop stability (current and voltage control loop) over a wide range of grid impedance of **2-20%** and during low-voltage ride-through. Guaranteed stability during 100% load step change dynamic. | The proposed control strategy demonstrates robust and stable performance across a wide range of grid impedances, spanning from **0.24%** to **22%**. Furthermore, the inverters sustain stable performance under a 100% load step change while effectively eliminating inrush current. |
| Voltage & Frequency regulation | Steady-state voltage error **<5%** and frequency error **<1%** under grid forming. Transient-state voltage error < **20%** and frequency error **<5%.** | The proposed **deadbeat-based** GFM control achieves excellent performance, maintaining a steady-state voltage error of less than **1%** and a frequency error of only **0.2%.** Additionally, the control strategy also demonstrates robust dynamic performance, with a transient voltage error < **2%** and a transient frequency error limited to **0.8%.** The proposed **VOC-based GFM** control also achieves very low voltage and frequency error **<1%,** in both transient states and steady states. |
| Ultrafast black start time | Two tenth of a second or less (**≤0.2 sec**) to support minimum required local critical loads (consist of constant impedance, constant current, constant power loads, or combination of these within 20% - 60% of inverter capacity). Five tenth of a second or less **(≤0.5 sec**) to establish voltage (within 0.917 – 1.05 | The proposed deadbeat-based and **VOC-based** ultrafast black start control method achieves outstanding performance across all required operational benchmarks. Specifically, for **deadbeat-based** method, it establishes voltage and supports the local critical loads **<< 0.2 s**, The system frequency reaches its designated setpoint within **1** switching frequency (**20 µs** for |

| | | |
|---|---|---|
| | p.u.) and frequency (within 59.5 – 60.1 Hz) setpoints, and connect more load (consist of constant impedance, constant current, constant power loads, or combination of these with more than 60% up to full inverter capacity). One second or less (**≤1 sec**) to reconnect to main grid. | **50kHz** switching frequency), ensuring rapid stabilization. Additionally, the grid resynchronization process is completed within **1** switching frequency (**20 µs** for **50kHz** switching frequency), far exceeding the requirement of reconnection within 1 second. While for **VOC-based method**, it establishes the PCC voltage and supports black start critical load in **80ms**, and starts to synchronize with the grid which ensures smooth transients in the following transitions. Two inverters startup sequentially are able to synchronize within **1 cycle (~16.67ms**), and another **1 cycle (~16.67ms)** for grid-reconnection. In conclusion, the proposed VOC method also far exceeding the time requirement of black start within 1 second. |

## 3.2 Project Tasks, Go/No-Go Milestones, and Deliverables

### Task 1 Inner-loop controller design -both software and hardware developments, their performance validation, and stability assessment

| | ***Description*** |
|---|---|
| **T1** | **Task Name: Inner-loop controller design -both software and hardware developments, their performance validation, and stability assessment**<br>**Task Description:** We will develop control algorithms and design the inner-loop controller for IBR based on our virtual resistance (VR) concept. The controller together with the upper controller (an already-developed micro-grid controller) will fulfill functionalities including grid synchronization, grid-forming, grid-following, islanding operation, etc. |
| **T1.1** | Virtual resistance (VR) based IBR system modeling and analysis.<br>**Completion in Q1-FY22:** Developed the mathematical and circuit models of IBR system with VR-based inner-loop control. |
| **T1.2** | UUCC's inner-loop controller design and development of both software and hardware.<br>**Completion in Q2-FY22:** Completed inner-loop design and started to write code and build testbed. |
| **T1.3** | IBR system stability assessment.<br>**Completion in Q2-FY22:** Studied IBR system stability based on the analytical models developed in Task 1.2. |
| **M1.1.1** | IBR system follows reference (current/voltage/frequency) within 20ms response time, 5% error for current and voltage over wide 3%-30% grid impedance variation range under the worst-case scenario of no interface inductor/filter.<br>**100% Completion:** Closed-loop control designed and simulation verified to meet the requirements. |
| **M1.1.2** | Inner-loop controller is able to follow reference (current/voltage) operating under 100% load step change, and 0-10% IBR interface impedance.<br>**100% Completion:** Inner-loop **c**ontrol parameters improved to achieve better steady state error and transient response under the load transients and different grid impedance. |
| **M1.1.3** | UUCC's inner-loop controller stability assessment under various quantitative grid conditions.<br>**100% Completion:** L2-gain method developed for stability assessment. |
| **Deliverables:** Inner-loop control design, analytical model, software code and hardware schematics. | |

**Subtask 1.1: Virtual resistance (VR) based IBR system modeling and analysis.**
In this subtask, the VR-based system was modelled and analyzed. Fig. 1-1 shows the inner-loop control block diagram in this project. Inverter output voltage $v_i$ is pulse-width modulation (PWM) waveform instead of sine waveform, the grid current is fed back to implement grid synchronization and closed-loop control. Further, the controller doesn't use traditional PLL method to synchronize with the grid, which will show benefits on stabilizing the system and improving system dynamic response in future verification. In summary, the controller applied in this project features PLL-less control scheme, which will improve the performance of IBR system in terms of dynamic response, stability, and flexibility.

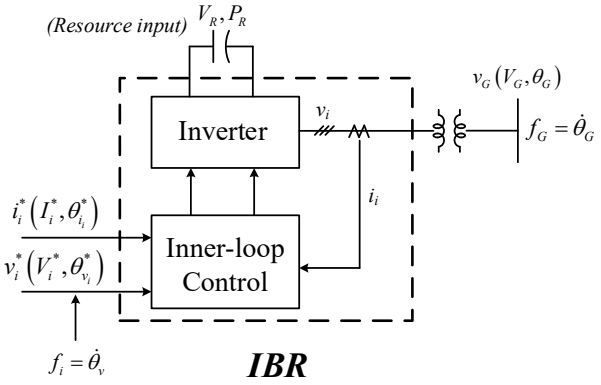


Fig 1-1: Inner-loop control block diagram

In Fig. 1-1, the dc-side of the IBR system is a constant dc power source. The ac-side of the IBR system is a variable ac power source to emulate the power grid. $V_G$ and $\theta_G$ are the ac voltage magnitude and phase, respectively, while $f_G$ is the power grid frequency. $v_i$ and $i_i$ are the inverter output voltage and current, respectively. Only $i_i$ will be utilized as the feedback information in the inner-loop control. $v_i$ is used when conducting comparison and verification and it will not participate into the inner-loop control. The input references can be the current, voltage and frequency. $I_i^*$ and $\theta_{ii}^*$ are the magnitude and phase of the current reference $i_i^*$, respectively. $V_i^*$ and $\theta_{vi}^*$ are the magnitude and phase of the current reference $v_i^*$, respectively. $f_i$ is the frequency of the inverter output voltage, which is the differential of the phase signal.

The mathematical model of the IBR related to the inner loop is as follows:

$$l_g \frac{d}{dt}\boldsymbol{i} = -\left(r_g I - l_g W\right)\boldsymbol{i} + \boldsymbol{v} - \boldsymbol{v_g}, \tag{1-1}$$

where $\boldsymbol{i}$, and $\boldsymbol{v}$, are the inverter current and voltage. Moreover, $\boldsymbol{v_g}$ is an unmeasurable grid voltage disturbance. The parameter $l_g$ is the grid inductance and is known, $r_g$ is the grid resistance, which is uncertain. The control objective is to regulate the current error using the virtual resistance (VR)-based control.
The current error is defined by $\tilde{\boldsymbol{i}} = \boldsymbol{i} - \boldsymbol{i}_0$. Then, the control law is designed to have the following form [27]

$$\boldsymbol{v} = \boldsymbol{v}_0 - r(\tilde{\boldsymbol{i}}) \tag{1-2}$$

where $r(\tilde{\boldsymbol{i}})$ is referred to as the virtual resistance for the control law.

Two scenarios have been identified for inner-loop control simulation verification: 1) Inverter output current/voltage to follow the current/voltage reference when the reference get a step change (amplitude, phase/frequency), where the grid voltage is kept unchanged; and 2) Inverter output current/voltage to follow the current/voltage reference when there is a disturbance (amplitude, phase/frequency step change) from the grid side.

**Subtask 1.2: UUCC's inner-loop controller design and development of both software and hardware.**

In this subtask, FSU team developed an inner-loop control algorithm for IBR system. In this control method, only grid current is fed back to implement grid synchronization and closed-loop control meanwhile the output voltage sensor of the inverter is removed. Further, the controller doesn't use traditional PLL method to synchronize with the grid, which will show benefits on stabilizing the system and improving system dynamic response in future verification.

Fig. 1-2 shows the schematic of IBR system with the proposed inner-loop control. Fig. 1-3 shows the detailed schematic of the proposed inner-loop control. For each phase, control is conducted independently. For each phase, there are three parts: phase detection, reference and feedforward signal generation, and current regulation.

The phase detection uses the voltage reference generated by the inner-loop control as its input. A low-pass filter is applied for noise suppression. The zero-crossing point is detected for further obtaining phase information while the sampling frequency is the fundamental frequency 60 Hz timing a specified frequency $f_0$. When the zero-crossing point is detected, the fixed angle frequency is applied to accumulate and generate phase information. The obtained phase information keeps synchronizing the inverter output voltage with the grid voltage.

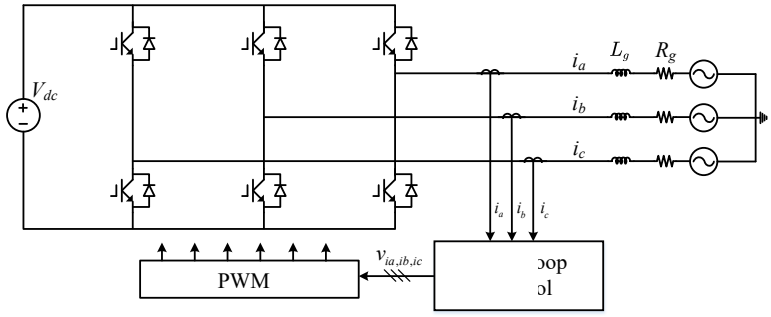


Fig 1-2: The diagram of the IBR system with the inner-loop control

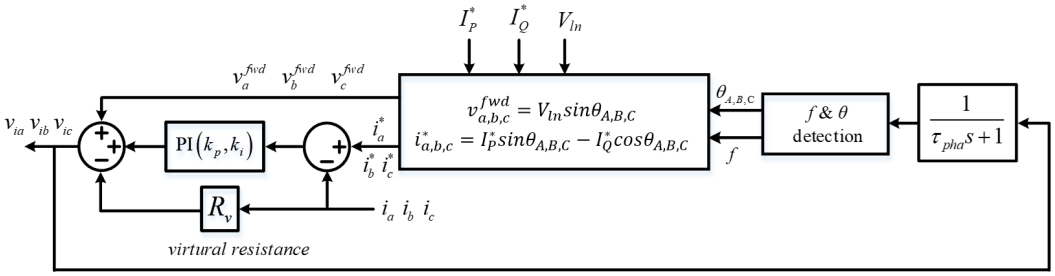


Fig 1-3: The schematic of inner-loop control

Based on the outer-loop control, the control reference $I_P^*$, $I_Q^*$ are applied to generate the three-phase current reference. Furthermore, a constant value based on the phase peak voltage of the grid, $V_{l\text{-}l}$, is employed to generate the three-phase feedforward signal. This feedforward ensures a fast response with stable performance even when there is a system disturbance.

Simulation verifications are performed for 1) current reference step changes from 0 to 1 p.u. within 20 ms; 2) grid voltage disturbance: phase step change, frequency step change, voltage dip. Table 1-1 lists the simulation system specifications and control parameters.

Fig.1-4 shows the simulation results when the current reference ramps up from 0 to 1 p.u. in 20 ms starting from $t$ = 0.2 s. It can be observed the inverter current follows current reference well. The inner-loop control steady state error was about 3.5% in this case, which satisfies the success value of the milestone table for this subtask.

Table 1-1 Inner-loop control simulation system specifications and control parameters

| Symbol | Name | Value | Symbol | Name | Value |
|---|---|---|---|---|---|
| $Z_{base}$ | Base Impedance | 2.304Ω | $R_v$ | Virtual resistance | 0.115 (5%) |
| $L_g$ | Grid Inductance | 0.367 mH (6%) | $k_i$ | Controller | 0 |
| $R_g$ | Grid Resistance | 27.6 mΩ (1.2%) | $k_p$ | Controller | 4.6 (200%) |
| $S_b$ | Inverter Capacity | 100 kVA | $T_{ramp}$ | Ramp time | 10 ms |
| $V_{ac}$ | Grid Voltage | 480 V (L-L RMS) | $R_{ramp}$ | Ramp rate | 10 %*$S_b$/ ms |
| $V_{dc}$ | Inverter dc voltage | 1000 V | $f_s$ | Switching frequency | 20k Hz |

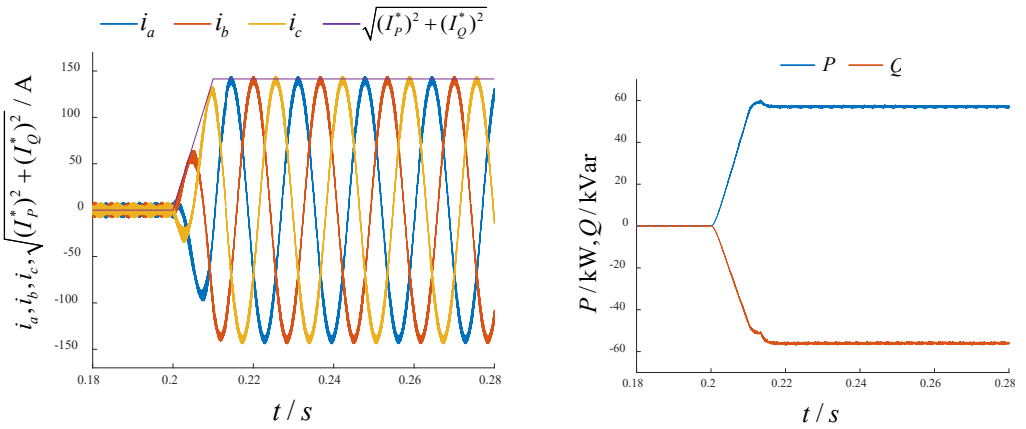


(a) Three-phase inverter output current & current magnitude. (b) inverter output P & Q.

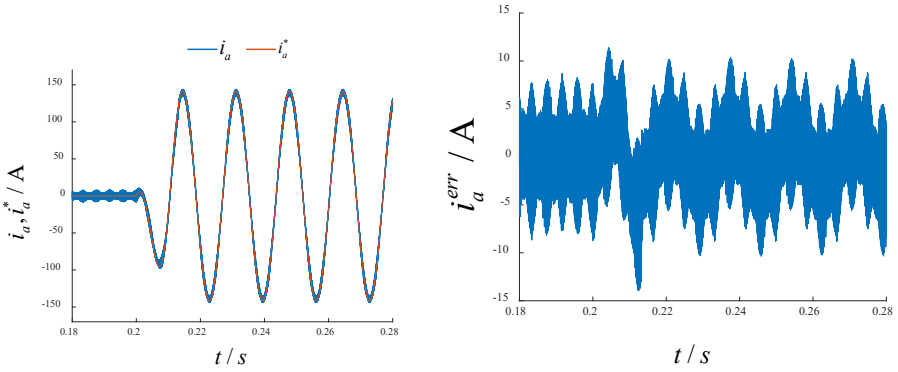


(c) Inverter phase A current and current reference. (d) Error of the inner-loop control.

Fig 1-4: Simulation results (PSCAD) when the current reference ramps up from 0 to 1 p.u. in 20 ms starting from t = 0.2 s.

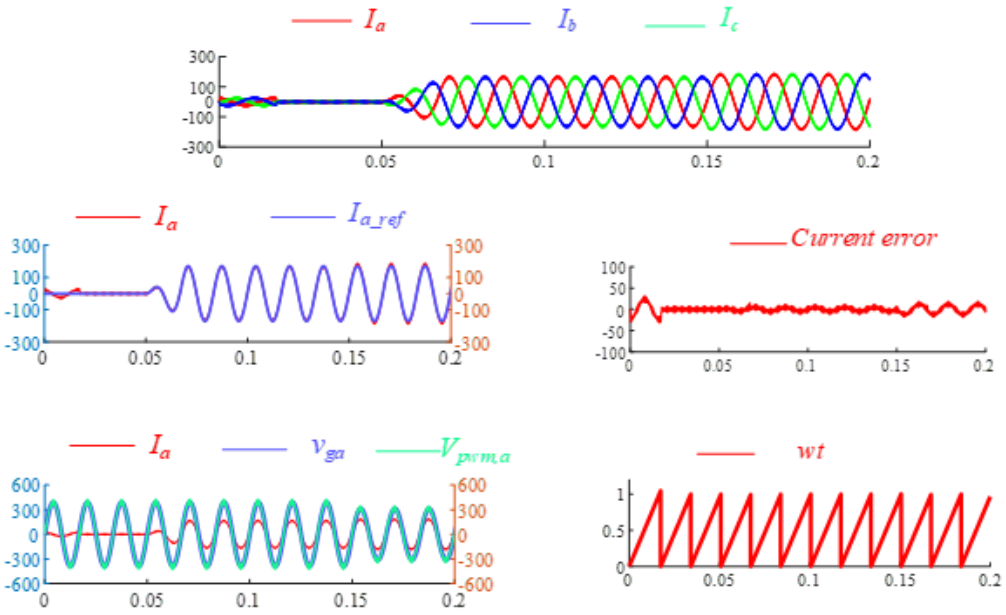


(a) grid voltage dip by 20% at t=0.15s, inverter current, current reference, current error, grid voltage and phase angle

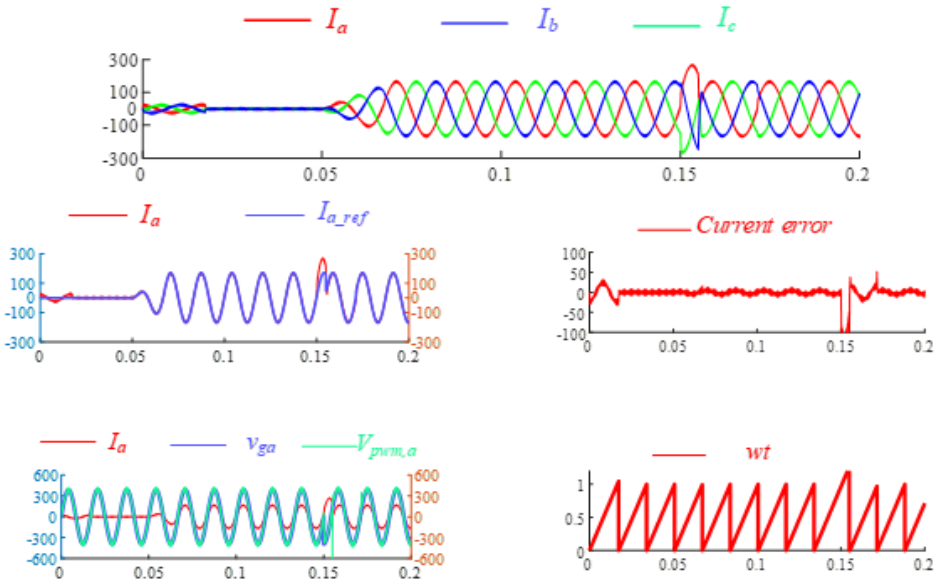


(b) grid voltage phase step change by 90 degrees at t=0.15s, inverter current, current reference, current error, grid voltage and phase angle.

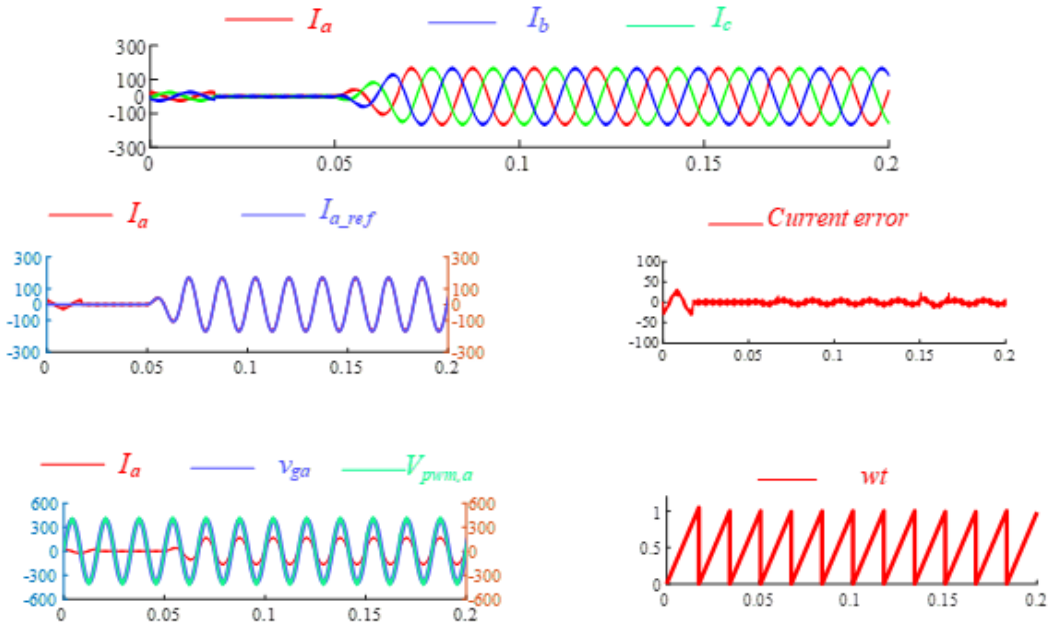


(c) grid voltage frequency step change from 60 Hz to 59.8 Hz at t=0.15s, inverter current, current reference, current error, grid voltage and phase angle.

Fig 1-5: Simulation results (PSIM model) when (a) grid voltage dip by 20%, (b) grid voltage phase step change by 90 degrees, and (c) grid voltage frequency step change from 60 Hz to 59.8 Hz, at t = 0.15 s respectively.

Fig. 1-5 shows the simulation results when 1) grid voltage dip by 20%, 2) grid voltage phase step change by 90 degrees, and 3) grid voltage frequency step change from 60 Hz to 59.8 Hz, at t = 0.15 s respectively. It can be observed that under above mentioned grid

disturbances, the inner-loop control was able to keep the inverter output current to follow the reference, with short transient time and suppressed overshoot.

The simulation has confirmed IBR system response within 20 ms and 5% error to current commend and system disturbances with the proposed inner-loop control.

To further validate the proposed inner-loop control, we established the platform for the inner-loop controller experimental validation platform. R&D inverter (MWINV-9R122B, 10 kVA, 400 V ac) and controller (PE-Expert 4), as shown in Fig. 1-6, were acquired for inner-loop control validation. Fig. 1-7 shows the setup of the established platform. Based on the experimental setup, we performed grid-tie IBR tests for the inner-loop controller verification. The system specifications are shown in Tab 1-2.

Table 1-2 Inner-loop control test system specifications and control parameters

| ***Variable*** | ***Symbol*** | ***Value [Unit]*** |
|---|---|---|
| *Line Frequency* | $f_g$ | *60 [Hz]* |
| *Switching Frequency* | $f_{sw}$ | *10k [Hz]* |
| *Grid Voltage* | $V_g$ | *360 [V]* |
| *DC link Voltage* | $V_{dc}$ | *680 [V]* |
| *Inductance* | $L_s$ | *4.0 [mH]* |
| *Capacitance* | $C_s$ | *4.4 [uF]* |
| *Virtual Resistance* | $R_v$ | *1 [Ohm]* |
| *Proportional Controller* | $k_p$ | *22.6* |

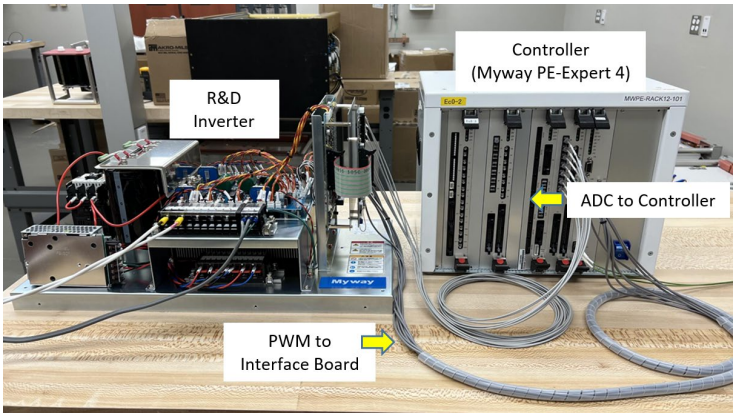


Fig 1-6: Myway R&D inverter and PE-Expert 4 (Controller) for inner-loop control validation.

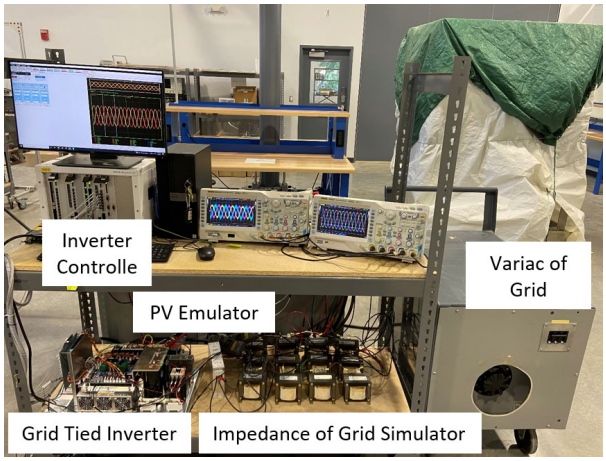


Fig 1-7: The setup of the inner-loop control validation platform.

Due to the voltage senseless feature, the inner-loop control needs a method for startup and grid synchronization. We developed an efficient startup method for the IBR system with the proposed inner-loop control, as shown in Fig. 1-8. The corresponding experimental result for its test is shown in Fig. 1-8 as well. The developed method can effectively avoid inrush current and reduce the grid disturbance when the IBR system starts the synchronization with the grid under grid-following mode.

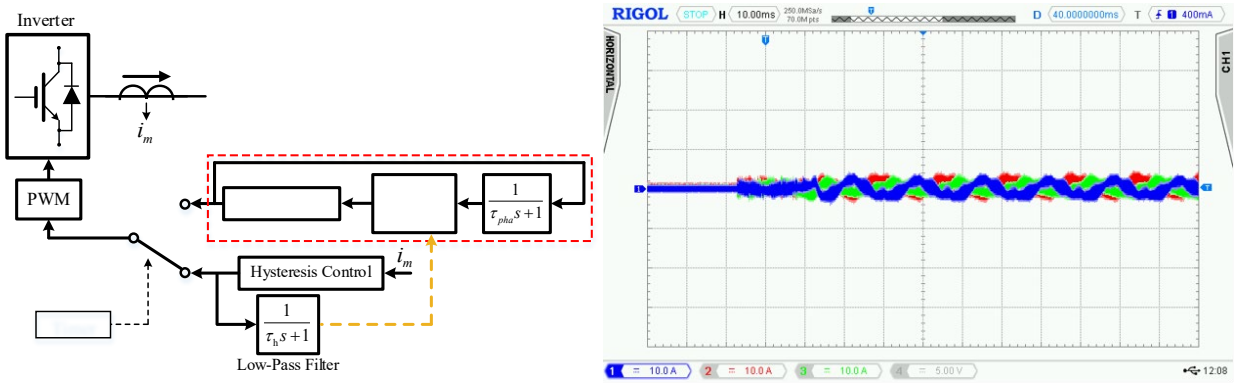


Fig 1-8: The developed startup method for the proposed inner-loop control (left) and the associated current dynamics of the IBR system startup.

The test cases of the full power steady-state operation are shown in Fig. 1-9, as the basic test for our established testbed platform. These test cases showcases that the established testbed is validated for further inner-loop control testing cases. In addition, the FFT of the employed R&D IGBT and SiC MOSFET inverter are separately tested. The test conditions for the SiC inverter are 600V dc voltage, 360V ac voltage, 8 kW standalone load power, and 50 kHz switching frequency. The test conditions for the IGBT inverter are 500V dc voltage, 300V ac voltage, 6 kW standalone load power, and 10 kHz switching frequency. The output L filter is 800μH (2% Zbase). The output L filter for both cases of FFT analysis is is 800μH (2% Zbase). The experimental results are shown in Fig 1-9 (d) and (e) with corresponding FFT analysis of the output currents. The THD of SiC inverter and IGBT inverter are 1.53% and 3.87%, respectively.

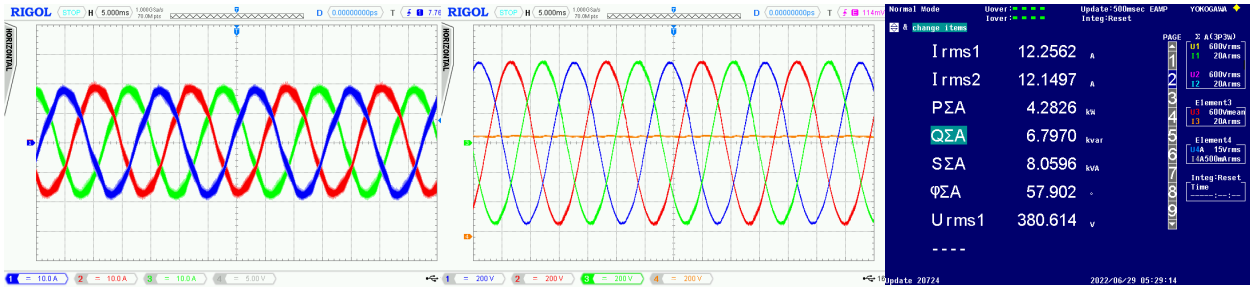


(a) current reference $I_{cmd\_PQ}$ = [13, 13] A

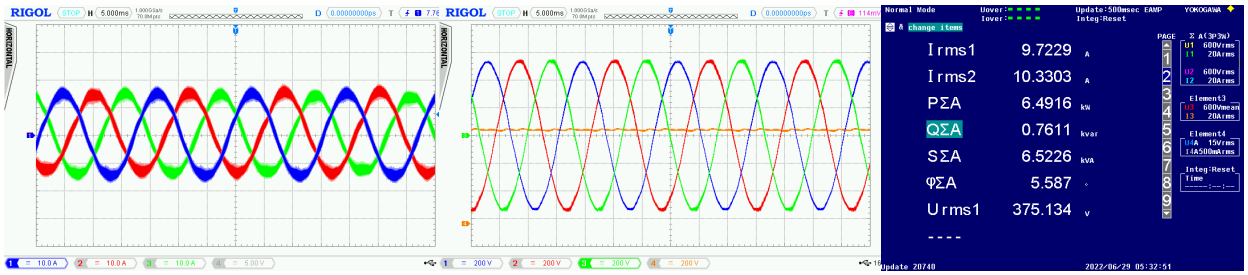


(b) current reference Icmd_PQ = [16, 0] A

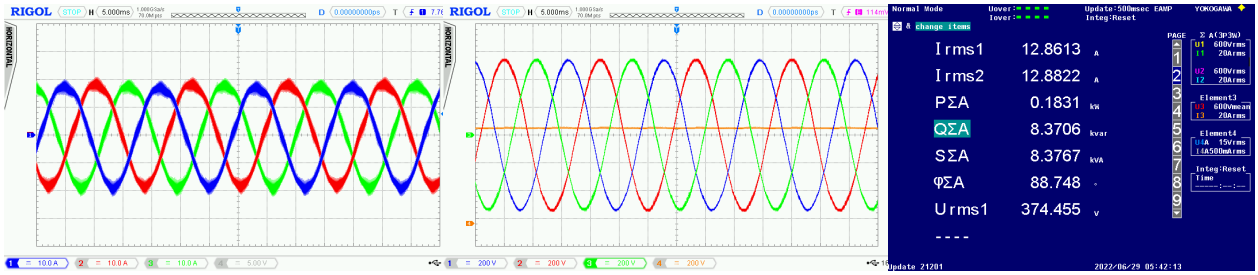


(c) current reference Icmd_PQ = [4, 17] A

Fig 1-9: Experimental results of the current, voltage dynamics and the measurement of power analyzer of the system and device test cases of inner-loop validation platform.

Furthermore, the transient test cases are performed to examine the dynamic response of the proposed inner-loop control. Fig. 1-10 shows 4 different test cases, i.e., full power step changing, output power factor changing with constant power magnitude, feedforward grid voltage magnitude dipping 20%, and feedforward grid voltage phase leading 30 degrees. According to the experimental results shown in Fig. 1-10, our developed inner-loop controller achieves the project requirements, i.e., within 20 ms dynamic response time and 5% error to current commend and system disturbances.

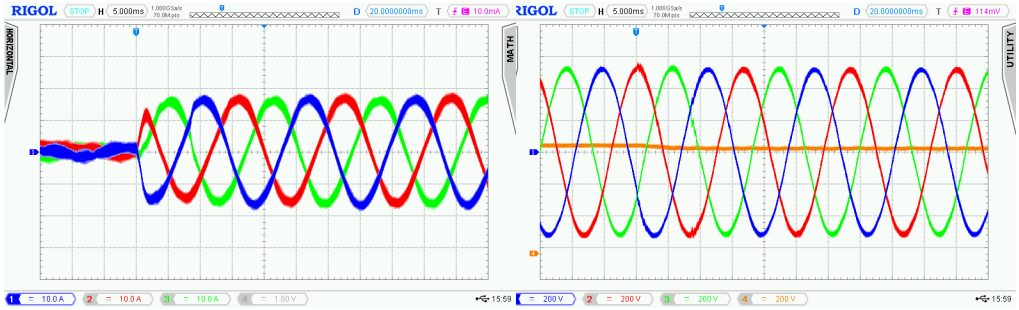

(a) current reference has a full power step change from [0.5, 0] A to [10, -14] A.

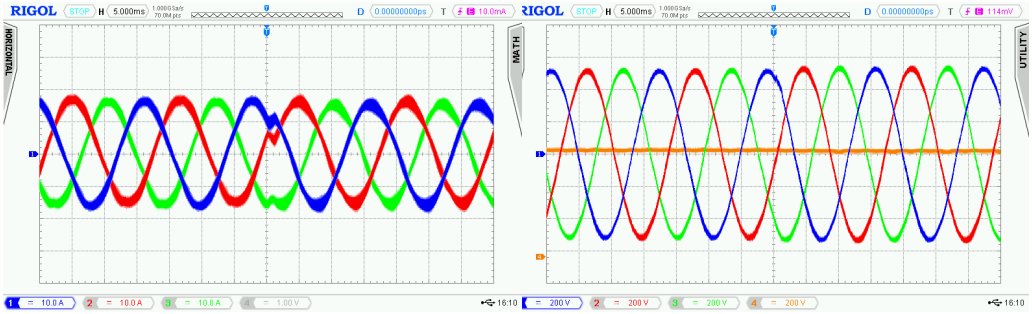


(b) Output power factor has a step change maintaining constant power magnitude with the current reference changing from [10, -14] A to [16, -6.32] A.

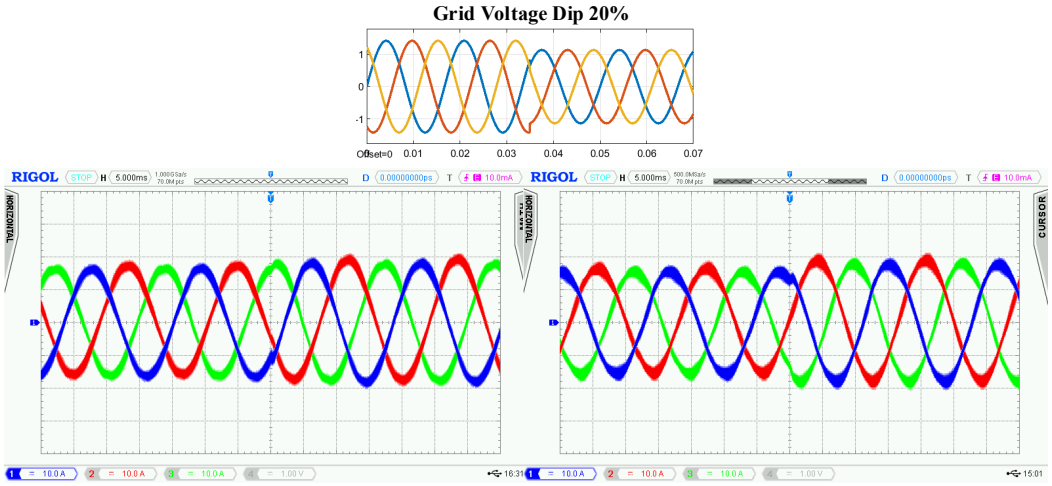


(c) the feedforward grid voltage dip by 20%, while the current reference is [10, -14] A (left), and [16, -6.32] A (right), respectively.

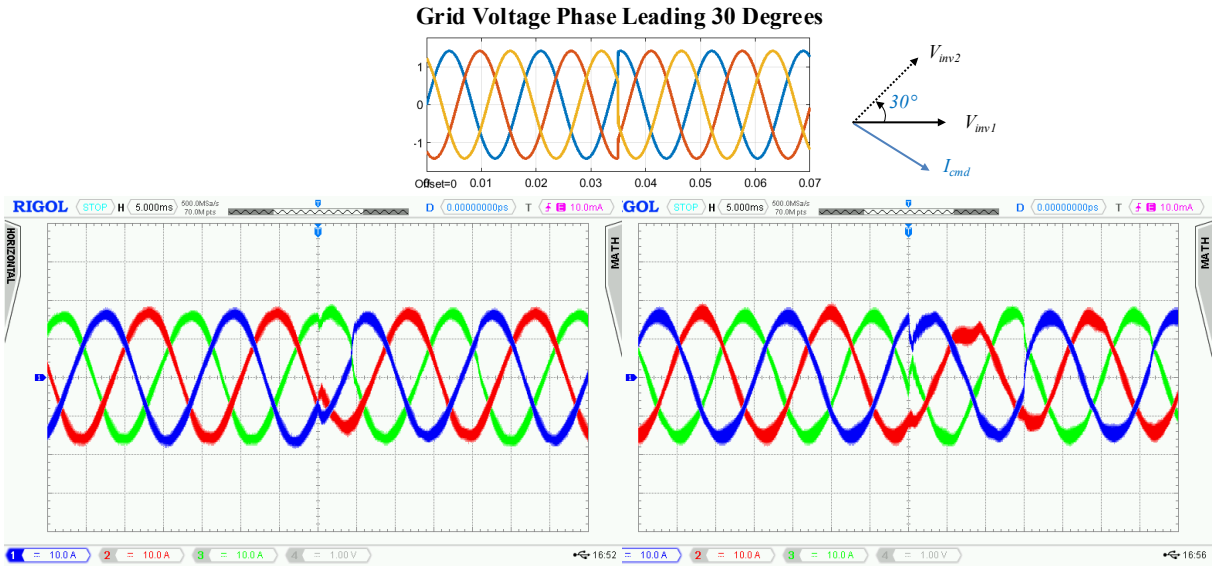


(d) the feedforward grid voltage got a phase step change by 30 degrees leading, while the current reference is [10, -14] A (left), and [16, -6.32] A (right), respectively.

Fig 1-10: Experimental results of the current and voltage dynamics of different test cases.

**Subtask 1.3: IBR system stability assessment.**

To assess the steady-state error of the inner-loop control, an analytic model of the inner-loop control was established in (1-3).

$$\frac{\Delta v}{R_g + j\omega_0 L_g} = i \Rightarrow \frac{\left(i^* - i\right)k_p - R_v i}{R_g + j\omega_0 L_g} = i \tag{1-3}$$

where

$\Delta v$ – compensated voltage from the inner-loop control;

*i, i** – inverter output (AC) current, and its reference, respectively;

$R_g$, $L_g$ – grid impedance;

$\omega_0$ – grid fundamental frequency;

$K_p$, $R_v$ – proportional coefficient, virtual resistance, respectively.

From (1-3), the steady-state error can be derived as

$$\frac{i - i^*}{i^*} = \frac{\left(k_p + R_v + R_g\right)^2 + \omega_0^2 L_g^2 - k_p\left(k_p + R_v + R_g\right) + jk_p\omega_0 L_g}{\left(k_p + R_v + R_g\right)^2 + \omega_0^2 L_g^2} \tag{1-4}$$

Thus, the steady-state error can be examined by (1-4) with specified system parameters when determining the parameters of the inner-loop control.

Several simulation cases under various power factors (cosϕ = 1, or 0), system impedance (6.12%, 30%), and Xg/Rg ratio (5, or 1) were conducted to verify this analytic model. Table 1-2 shows the steady-state error calculated via (1-2), and measured in simulation. The results show the error in calculation is consistent with the observation obtained from the simulation cases. With the influence of low pass filter in simulation, error attenuated compared to the analytic model. In conclusion, (1-4) is an effective analytic model for inner-loop steady-state error estimation.

Table 1-3 Inner-loop steady-state error

| System parameters and control variables | | | | | Error in calculation | Error in simulation |
|---|---|---|---|---|---|---|
| *i** | $Z_g$ / *p.u.* | $X_g/R_g$ | $K_p$ | $R_v$ | $\frac{\lvert i^*-i\rvert}{\lvert i^*\rvert}$ / % | $\frac{\lvert i^*-i\rvert}{\lvert i^*\rvert}$ / % |
| $172\,\boldsymbol{A}\angle 0°$ (1 p.u.) | 6.12% | 5 | 4.6 (200%) | 0.115 (5%) | 4.19% | 3.26% |
| $165\,\boldsymbol{A}\angle 90°$ (0.96 p.u.) | 6.12% | 5 | 4.6 (200%) | 0.115 (5%) | 4.18% | 3.94% |
| $172\,\boldsymbol{A}\angle 0°$ (1 p.u.) | 6.12% | 5 | 10 (434%) | 0.115 (5%) | 1.98% | 1.69% |
| $165\,\boldsymbol{A}\angle 90°$ (0.96 p.u.) | 6.12% | 5 | 10 (434%) | 0.115 (5%) | 1.94% | 2.06% |
| $172\,\boldsymbol{A}\angle 0°$ (1 p.u.) | 30% | 1 | 4.6 (200%) | 0.115 (5%) | 14.88% | 10.99% |
| $165\,\boldsymbol{A}\angle 90°$ (0.96 p.u.) | 30% | 1 | 4.6 (200%) | 0.115 (5%) | 14.88% | 8.67% |
| $172\,\boldsymbol{A}\angle 0°$ (1 p.u.) | 30% | 1 | 18.4 (800%) | 0.115 (5%) | 4.09% | 1.22% |
| $165\,\boldsymbol{A}\angle 90°$ (0.96 p.u.) | 30% | 1 | 18.4 (800%) | 0.115 (5%) | 4.09% | 1.45% |

Grid voltage $v_g$ = $1\angle 0^\circ$ p.u.

The mathematical model of the IBR related to the inner loop is in (1-5)

$$l_g \frac{d}{dt}\boldsymbol{i} = -\left(r_g I - l_g W\right)\boldsymbol{i} + \boldsymbol{v} - \boldsymbol{v_g}, \tag{1-5}$$

where $\boldsymbol{i}$, and $\boldsymbol{v}$, are the inverter current and voltage. Moreover, $\boldsymbol{v_g}$ is an unmeasurable grid voltage disturbance. The parameter $l_g$ is the grid inductance and is known, $r_g$ is the grid resistance, which is uncertain. The control objective is to regulate the current error using the virtual resistance (VR)-based control depicted in Fig. 1-11.

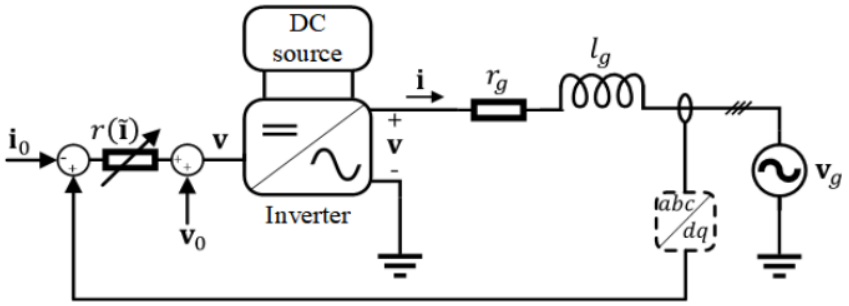


Fig 1-11: VR-based control connected to a power inverter and the grid line model

The current error is defined by $\tilde{\boldsymbol{i}} = \boldsymbol{i} - \boldsymbol{i}_0$. Then, the control law is designed to have the following form:

$$\boldsymbol{v} = \boldsymbol{v}_0 - r(\tilde{\boldsymbol{i}}) \tag{1-6}$$

where $r(\tilde{\boldsymbol{i}})$ is referred to as the virtual resistance for the control law above.
Based on the Proposition. 1 stated in [27], examples of the VR are cubic functions of the current error, hybrid function (linear+cubic), and hyperbolic sine function of the current error.
We provided the stability analysis using dissipative system's theory. The idea is to show that the IBR, together with the control system, is a net dissipator of disturbance energy. To do so, we found a positive definite storage function V (energy function of the current error) such that the following dissipativity inequality holds

$$\mathbf{V(i)} \leq \int_0^t \left( \gamma^2 \left\| \begin{bmatrix} \mathbf{i}_0 \\ \tilde{\mathbf{v}}_\mathbf{g}(\tau) \end{bmatrix} \right\|^2 - \|\mathbf{i}(\tau)\|^2 \right) d\tau \tag{1-7}$$

This shows an upper bound on the L2-gain from the grid voltage variation and the current initial condition to the current error as follows:

$$\frac{\|\boldsymbol{i}(\tau)\|_{\mathcal{L}_2}}{\left\| \begin{bmatrix} i_0 \\ \tilde{\boldsymbol{v}}_g(\tau) \end{bmatrix} \right\|_{\mathcal{L}_2}} \leq \gamma \tag{1-8}$$

Thus, the more $\gamma$ decreases the better the closed-loop system is robust against the grid voltage disturbance and the current initial condition. Consider an energy function candidate with the following form

$$V(\boldsymbol{i}) = \boldsymbol{i}^T P \boldsymbol{i} \tag{1-9}$$

where P is a positive definite matrix to be determined. Since we are interested in minimizing an upper bound for the L2-gain ($\gamma$), we set up the following optimization problem [27]:

$$\text{Minimize: } \gamma^2$$
$$\text{Subject to:}$$
$$\begin{bmatrix} 2\frac{r_g+\kappa}{l_g}P - PW - W^TP - I & P \\ P & 4\gamma^2 l_g^2 I \end{bmatrix} \succcurlyeq 0$$
$$P \succ 0 \tag{1-10}$$

Moreover, by solving the problem analytically to find an upper bound on L2-gain, we obtained the following inequality [27]:

$$\gamma \geq \frac{1}{2(r_g+\kappa)} \tag{1-11}$$

Figure 1-12 depicts the gamma with respect to the VR gain showing that both the optimization solution and the analytical approach gives the same amount for the gamma upper bound.

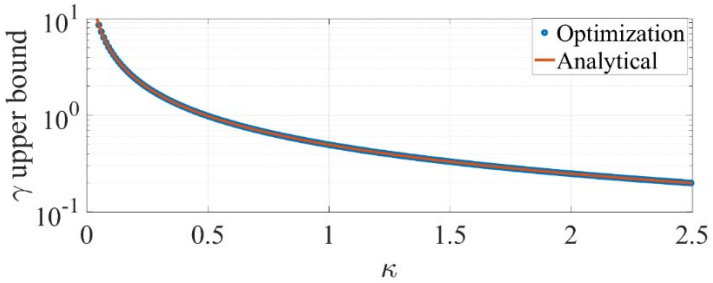


Fig 1-12: L2-gain variation with κ

Moreover, it shows the higher the VR gain, the lower the upper bound on the L2-gain increasing the robustness of the closed-loop system.

To assess the theoretical results, three cases are considered for the simulation.

**Case I: persistent grid voltage disturbance**

For this case we carry out a sine-sweep experiment with 10% variation in the grid voltage. An approximation frequency response from the grid voltage to the current error is computed and shown in Fig. 1-13 using the notion of variance gain.

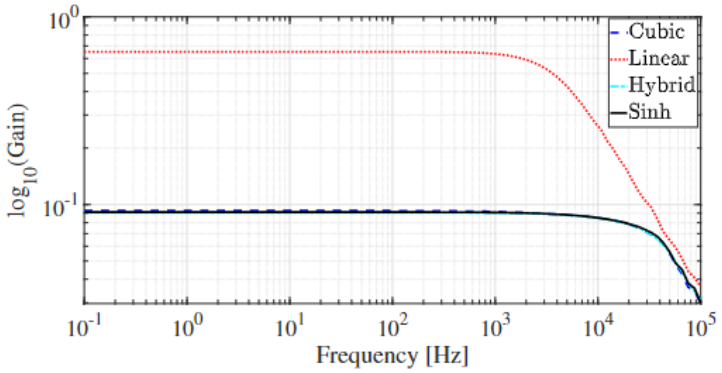


Fig 1-13: Variance gain of the current error for VR-based controllers [27]

Figure 1-13 shows that the upper bound on the L2-gain for other types of VRs are smaller than the linear one over a frequency range showing that they are more robust against the voltage grid disturbance.

**Case II: Rectangular grid voltage pulse**

In this case we injected a rectangular pulse with an amplitude 10% deviation from nominal at t=0.1 sec and lasts 1 msec. Fig. 1-14 shows the current error of the VR-based controllers.

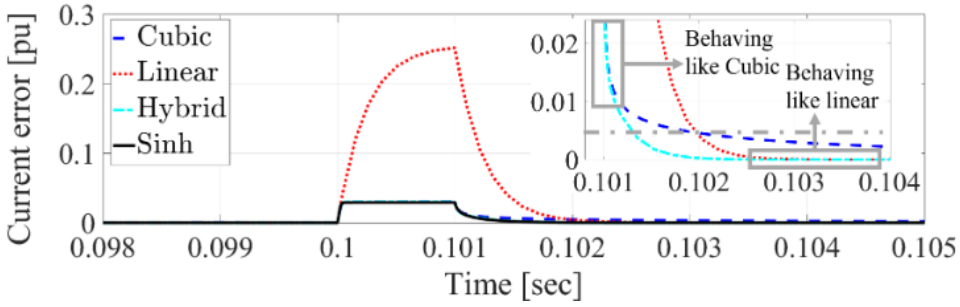


Fig 1-14: The current error of the IBR subject to a rectangular pulse grid voltage [27]

**Case III: Random grid resistance variation**

In this case the grid resistance is varied randomly using a uniform distribution within the range of 70% of the nominal value of the grid resistance starting at t =0.1 sec, and vanishing at t=0.6 sec. Fig. 1-15 shows the current error response subject to such grid resistance variation.

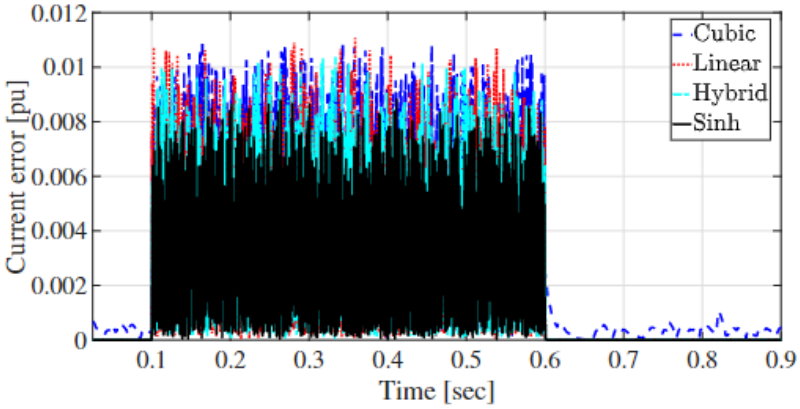


Fig 1-15: The current error of the IBR subject to a uniformly distributed grid resistance variation [27]

Figure. 1-16 shows the current error response of the IBR when it is subjected to both a uniformly distributed grid resistance variation and a pulse voltage grid disturbance.

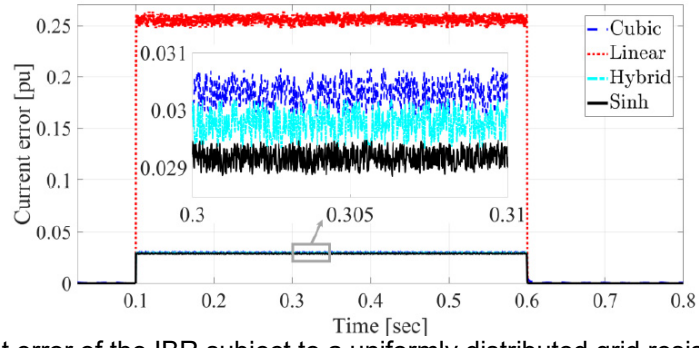


Fig 1-16: The current error of the IBR subject to a uniformly distributed grid resistance variation and a pulse voltage disturbance [27].

## Task 2 Outer-loop controller design, implementation, and stability assessment

| | *Description* |
|---|---|
| **T2** | **Task Name: Outer-loop controller design, implementation, and stability assessment**<br>**Task Description:** We will develop the models and design the outer-loop coordinative controller. The controller will fulfill functionalities of voltage and frequency (V&f) regulation, and the controller will be implemented by industrial control systems partner on industrial hardware-based platform. |
| **T2.1** | Universal decoupled V&f control applied to a realistic power grid system<br>**Completion in Q4-FY22:** Developed a universal decoupled V&f control that is applied to a realistic power grid system. |
| **T2.2** | UUCC's outer-loop controller design and software simulation.<br>**Completion in Q4-FY22:** Designed an outer-loop control different from T2.1, and simulated the control performance based on the developed analytical model. |
| **T2.3** | Outer-loop controller implementation on microgrid controller platform.<br>**Completion in Q4-FY22:** Implemented outer-loop control of T2.1 on the Siemens microgrid controller platform and established communication interface between MGC and inner-loop controller. |
| **T2.4** | Distribution system stability assessment.<br>**Completion in Q4-FY22:** Evaluated stability of control developed in T2.2 using Lyapunov methods and dissipative theory. |
| **T2.5** | Hardware acquisition for microgrid controller.<br>**Completion in Q2-FY22:** Built hardware interface between MGC and inner-loop controller. |
| **M1.2.1** | Model captures a large (>90% uncertainty range or X/R's values from 3 to 30) variation in X/R from small-scale distribution-level realistic model to large-scale transmission-level realistic model.<br>**100% Completion:** The uncertainty model to characterize X/R variation, which varies widely from low X/R ratios (as low as 3) at distribution level to high X/R ratios (as high as 30) for a realistic model of power grid, was successfully established. |
| **M1.2.2** | Design the outer-loop controller based on the developed model in 1.2.1, develop a fault disturbance scenario to verify the voltage response of the controller and develop a load increase (or decrease) scenario to verify the frequency response of the controller.<br>**100% Completion:** UUCC's outer-loop controller design and simulation were finished. |
| **M1.2.3** | Assessment of developed controller stability at distribution system level via case studies in a high-fidelity model<br>**100% Completion:** Stability of outer-loop control developed in T2.2 stability were assessed based on the developed high-fidelity models. |

### Subtask 2.1: Universal decoupled V&f control applied to a realistic power grid system

In this subtask, the universal decoupled V&f control applied to a realistic power grid system was presented in Fig. 2-1, the universal control system architecture integrates both primary and secondary control functions.

The green block in the figure represents the primary control level, which consists of a dual-loop control scheme: an inner current control loop and an outer voltage control loop. This structure is augmented by a droop control mechanism to facilitate decentralized power sharing among parallel inverters.

The orange block is responsible for secondary frequency control and active power load sharing. It calculates distinct active power set points for each inverter based on frequency measurements taken at the point of common coupling (PCC). This ensures coordinated frequency regulation and proportional load distribution across the inverters.

The blue block manages the secondary voltage control, aiming to minimize voltage mismatches among the distributed inverters. By compensating voltage discrepancies, it enhances voltage stability and improves overall power quality at the PCC.

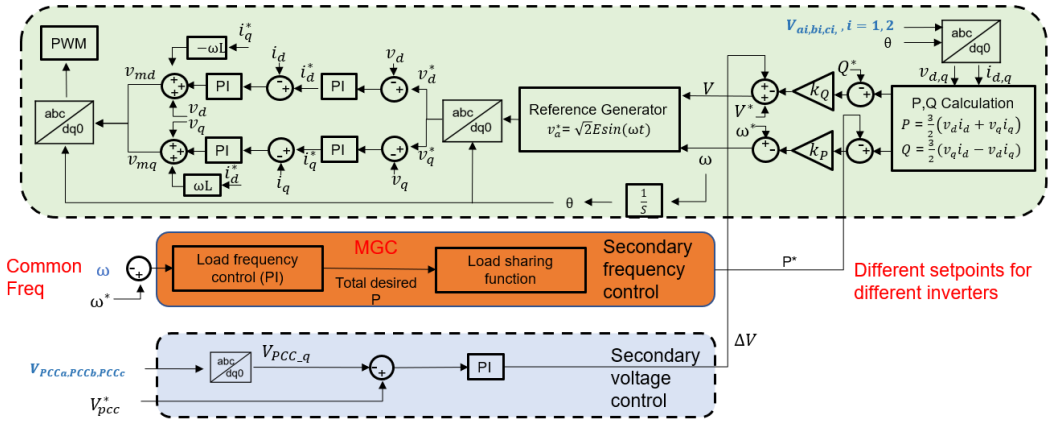


Fig. 2-1 The Universal decoupled V&f control scheme of GFM inverters.

**Subtask 2.2: UUCC's outer-loop controller design and software simulation**

In this subtask, a new outer-loop controller different from that in subtask 2.1 was designed, and corresponding simulations were conducted to evaluate the effectiveness of the proposed control algorithm.

The design process explicitly considered uncertainties in both grid dynamics and load characteristics. Specifically, the load is modeled as an uncertain resistive element, with an additional unmeasurable current component introduced to represent external disturbances.

As depicted in Fig. 2-2, the system configuration includes an inverter connected to a transmission line and a composite load model. The control design procedure is organized into three main components: (1) system modeling, (2) voltage control design, and (3) frequency control design.

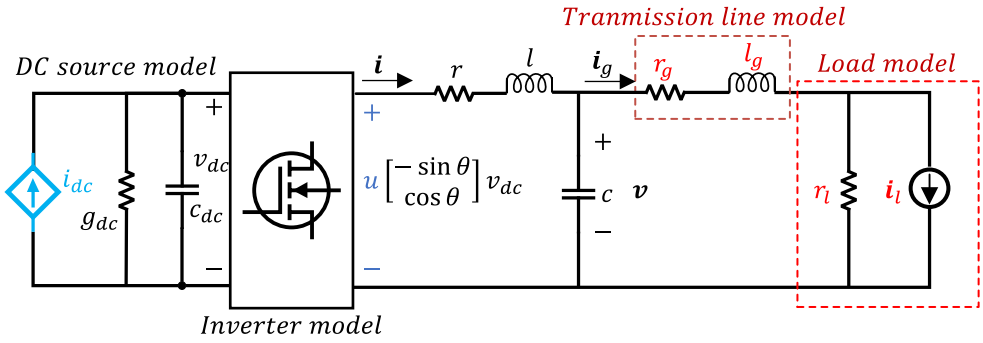


Fig. 2-2: The 3-phase DC/AC converter model with DC energy source, transmission line, and the load models in αβ frame

*1. Model Development*

The DC energy source dynamic is modelled by the following equation:

$$c_{dc}\dot{v}_{dc} = -g_{dc}v_{dc} + i_{dc} - \left(\begin{bmatrix} 0 \\ 1/2 \end{bmatrix}^{\top} \mathbf{i}\right) u \tag{2-1}$$

, where $v_{dc}, i_{dc}$ are the DC voltage (state) and current (control input in the DC part), $u$ is the control input in the AC part. By observation, the DC voltage dynamics mimics the frequency dynamics in synchronous machines using the following conversion

$$\omega = \eta v_{dc} \tag{2-2}$$

, where $\omega$ is the frequency in $^{rad}/_{sec}$, and $\eta = {}^{\omega_0}/_{v_{dc0}}$, and $\omega_0$, $v_{dc0}$ are the nominal values for the frequency, and DC voltage, respectively.
Then, in the AC side, the grid current dynamics can be represented by the equation below:

$$\dot{\mathbf{i}}_g = -\frac{(r_g + r_l)}{l_g}\mathbf{i}_g - v_{dc}\eta J\mathbf{i}_g + \frac{1}{l_g}\mathbf{v} + \frac{r_l}{l_g}\mathbf{i}_l, \tag{2-3}$$

Where $\boldsymbol{i}_g$ is the grid current, $\boldsymbol{i}_l$ is an unmeasurable current load disturbance, $r_l$ is an uncertain load resistance, $r_g$, and $l_g$ are uncertain grid resistance, and grid inductance. Also, $J = \begin{bmatrix} 0 & -1 \\ 1 & 0 \end{bmatrix}$.
The uncertainty load can be modeled as follows

$$\begin{aligned} \frac{r_g + r_l}{l_g} &= \left(\frac{r_{g0} + r_{l0}}{l_{g0}}\right)(1 + \delta_g), \\ \frac{1}{l_g} &= \frac{1}{l_{g0}}(1 + \rho_v), \end{aligned} \tag{2-4}$$

where $r_{g0}$, $l_{g0}$, and $r_{l0}$ are nominal grid resistance, inductance, and the load resistance, respectively. Moreover, $\delta_g$, and $\rho_v$ are uncertain parameters, which are bounded as $|\delta_g| \le \bar{\delta}$, $|\rho_v| \le \bar{\rho}$, for some konwon positive constants $\bar{\delta}$, and $\bar{\rho}$. Consequently, the above-mentioned uncertainty model can be rewritten as

$$\begin{aligned} \frac{r_g + r_l}{l_g} &= \frac{r_{g0} + r_{l0}}{l_{g0}}\left(\hat{\delta} + \Delta_g\right), \\ \frac{1}{l_g} &= \frac{1}{l_{g0}}(\hat{\rho} + \Delta_v), \\ \text{where } 0 < \Delta_g \le c_g,\ 0 < \Delta_v \le c_v,\ c_g > 0,\ c_v > 0,\ \hat{\delta} &\triangleq 1 - \bar{\delta},\ \hat{\rho} \triangleq 1 - \bar{\rho}. \end{aligned} \tag{2-5}$$

Besides, the voltage and current dynamics are modelled as:

$$\begin{aligned} \dot{\mathbf{v}} &= -v_{dc}\eta J\mathbf{v} - \frac{1}{c}\mathbf{i}_g + \frac{1}{c}\mathbf{i} \\ \dot{\mathbf{i}} &= -\frac{rI + v_{dc}\eta l J}{l}\mathbf{i} - \frac{1}{l}\mathbf{v} + v_{dc}\begin{bmatrix} 0 \\ 1/2 \end{bmatrix} u \end{aligned} \tag{2-6}$$

*2. Voltage control design*
The control objective in this section is to regulate the voltage tracking error. However, there are two control challenge in this layer. First, the inverter voltage dynamic is nonlinear and has couplings with other state variables. The other control challenge is that the IBR

sensor-less for voltage. Hence, we need to design a nonlinear multivariable controller along with a nonlinear multivariable observer. We design a voltage observer as follows

$$\dot{\hat{\mathbf{v}}} = -\eta v_{dc} J\hat{\mathbf{v}} - \frac{1}{c}\mathbf{i}_g + \frac{1}{c}\hat{\mathbf{i}} + \frac{1}{\varepsilon}\boldsymbol{\sigma}_i,$$

$$\dot{\hat{\mathbf{i}}} = -\frac{rI + \eta l v_{dc} J}{l}\hat{\mathbf{i}} - \frac{1}{l}\hat{\mathbf{v}} + v_{dc}\begin{bmatrix} 0 \\ 1/2 \end{bmatrix} u + \frac{1}{\varepsilon}\boldsymbol{\sigma}_i, \tag{2-7}$$

, where $\boldsymbol{\sigma}_i = \boldsymbol{i} - \hat{\boldsymbol{\imath}}$ is the current error estimation, $\hat{\boldsymbol{v}}$, and $\hat{\boldsymbol{\imath}}$ are the estimated inverter voltage and current, and $\varepsilon$ is the observer gain. Defining the voltage tracking error $\boldsymbol{e}_v = \hat{\boldsymbol{v}} - \boldsymbol{v}_0$. Consequently, the voltage control law is designed as follows

$$\tilde{\mathbf{i}} = c\eta J\tilde{v}_{dc}\mathbf{v}_0 + \tilde{\mathbf{i}}_g - k_v\mathbf{e}_v - \frac{c}{\varepsilon}\boldsymbol{\sigma}_i, \tag{2-8}$$

*3. Frequency control design*

The control objective in this section is to regulate the frequency tracking error. Similar to the voltage dynamics, the challenge here is the couplings between state variables. In addition, we need to deal with the exogenous signal $u$, which we will treat it as a measurable disturbance. In this part, we used the similarity dynamics between a synchronous machine and the DC dynamics of the IBR. Then, using this duality, by controlling the DC voltage, we can control the frequency. The mathematical analysis for the frequency control provides an asymptotical stability certificate with a sufficient condition giving the control gains design. Define the DC voltage tracking error $\tilde{v}_{dc} = v_{dc} - v_{dc0}$. Then, define the filtered tracking error

$$\psi = \tilde{v}_{dc} + \beta \underbrace{\int_0^t \tilde{v}_{dc}\tau}_{\tilde{v}_{dcI}}, \tag{2-9}$$

,where $\beta$ is the integrator gain. Consequently, the DC voltage control law is designed to have the following form

$$\tilde{i}_{dc} = \text{sat}\left(-k_{dc}\psi, x_1 + b, x_2 + b\right) - \tilde{\omega}_{dc}, \tag{2-10}$$

, where $k_{dc}$ is the DC voltage gain, $\tilde{\omega}_{dc} = \omega_{dc} - \omega_{dc0}$ with $\omega_{dc0} = -\left(\begin{bmatrix} 0 \\ 1/2 \end{bmatrix}^T \boldsymbol{i}_0\right)u_0, x_1 = -\bar{\imath}_{dc}, x_2 = \bar{\imath}_{dc}$, and $b = -i_{dc0} + \tilde{\omega}_{dc}$. Using the DC voltage control law provides a global asymptotical stability certificate with the following sufficient condition

$$\mu k_{dc} + g_{dc} \geq c_{dc}\beta + \frac{g_{dc}^2}{4c_{dc}\beta}, \tag{2-11}$$

*4. Simulation results*

Based on the design method shown above, Fig. 2-3, and Fig.2-4 show the simulation results of voltage error response of the IBR subjected to the disturbance, and a uniformly distributed grid parameters and load resistance variation.

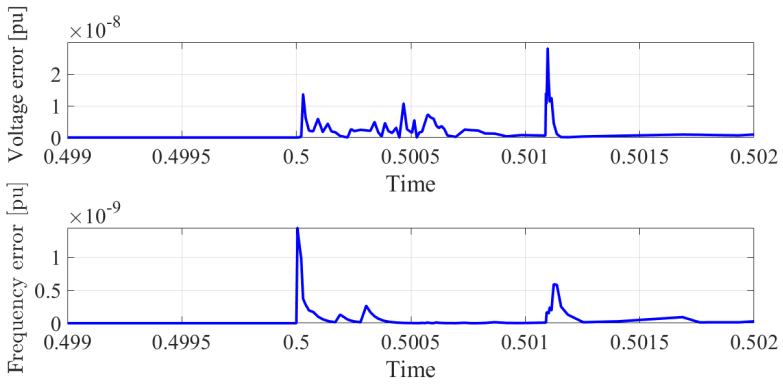


Fig. 2-3 Voltage and frequency error of the IBR subjected to a pulsated current load disturbance

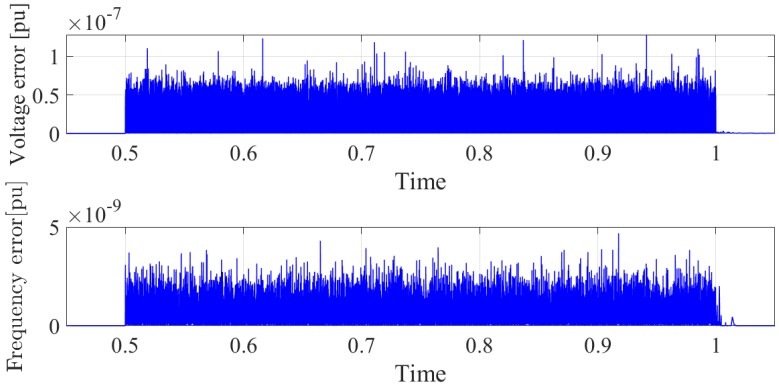


Fig. 2-4 Voltage and frequency error of the IBR subjected to a uniformly distributed grid resistance, inductance, and the load resistance variation

**Subtask 2.3: Outer-loop controller implementation on microgrid controller platform**

In this subtask, the outer-loop control of subtask 2.1 was implemented on the microgrid controller (MGC). Additionally, a bi-directional communication between MGC and inverter controller (PE-Expert 4) was established using the Modbus RTU protocol. The MGC utilizes the Modbus RTU Master to send the reading command, then the inner-loop controller receives the command and responds to the request, working as a Modbus RTU slave. In order to verify the communication, an online test was performed and the CAEx Plus logic platform for MGC. As shown in Fig. 2-5, where TLH.MG1.REF.IN denotes the

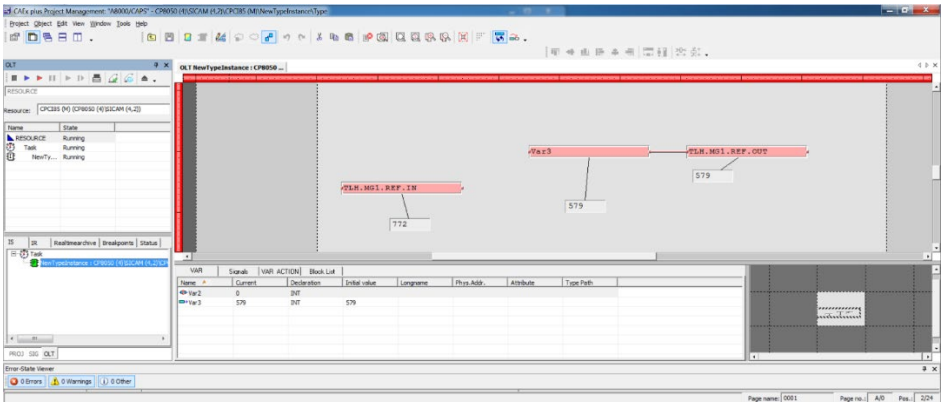


Fig. 2-5: CAEx Plus logic platform for MGC during the communication test.

received data from inverter side measurements and TLH.MG1.REF.OUT is the reference setting value sent to the inverter controller. In this test, 579 was the control reference sent out and 772 was the received inverter side measurement.

Furthermore, a logic schematic for MGC was developed to verify the communication function. As shown in Fig. 2-6, the active power P (16) and reactive power Q (7) control commands were integrated into TLH.MG1.P_ref.OUT (4230) which was sent out from MGC to the inverter inner-loop controller. While the TLH.MG1.P_ref.IN (258) denoted the received measurements from the inverter side.

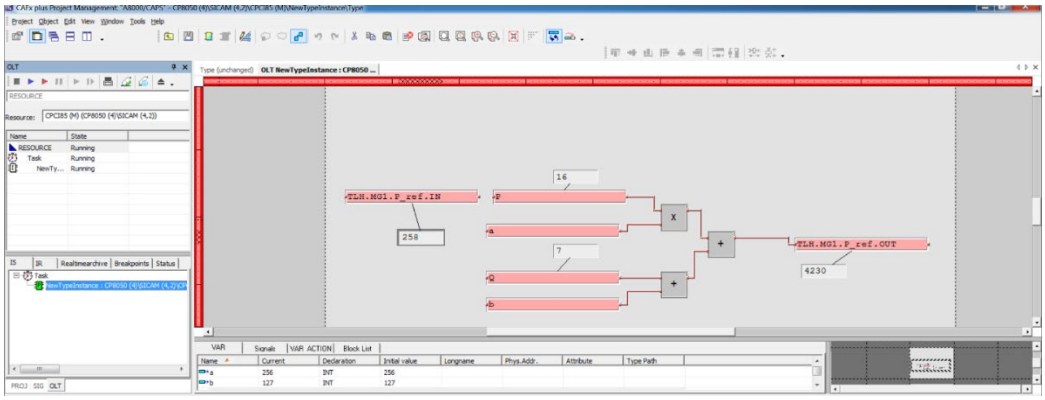


Fig. 2-6: A logic schematic built in CAEx Plus platform.

Following the successful validation of the Modbus RTU protocol, a bidirectional communication test (read/write) was carried out between the SIEMENS microgrid controller CP8050 and the DSP C6657 of the MyWay PE-Expert 4 platform. This test serves to establish the standard communication protocol between the R&D inverters (inner-loop) and the microgrid controller (MGC) (outer-loop). Fig. 2-7 shows the test case. At the beginning, the MGC CP8050 sends message to the DSP C6657 to read the particular register 0x00. The DSP C6657 returns the stored value 654 in register to the MGC CP8050. Then, MGC CP8050 executes a simple adding as 654 + 111 = 777 and sends this obtained results to DSP C6657 with storing it to the particular register 0x09. At last, DSP C6657 successfully receives this results and stores it.

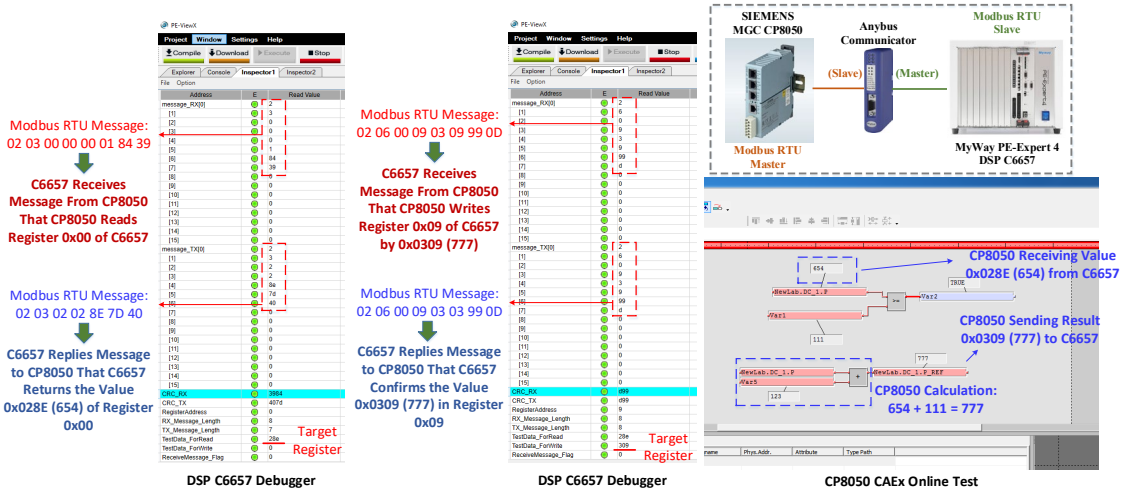


Fig.2-7 The Communication test of the framework between R&D inverters (inner-loop) and Microgrid Controller (MGC) (outer-loop)

Then, the aforementioned Modbus RTU communication protocol is applied to the bi-direction communication between MGC and OPAL-RT real-time simulator. The MGC is the Modbus RTU master terminal in the communication network and OPAL-RT is the slave terminal. The communication function of the MGC and OPAL-RT are tested separately before integrating them together. The associated test cases are shown as Figs. 2-8 and 2-9, respectively.

In the test case for MGC communication verification, the serial communication terminal (SCT) is leveraged as a Modbus RTU slave to validate the coming commands from MGC. As shown in Fig. 2-8, MGC initializes a reading command in step 1, where the SCT responses during step 2 based on received information at step 1. Once the responded information verified by the MGC, a writing command is sent out in step 3 subsequently. A communication cycle of MGC as Modbus RTU master is achieved when the same writing command is transmitted back to MGC from SCT at step 4.

In the test case for OPAL-RT real-time simulator communication verification, the SCT is leveraged as a Modbus RTU master to validate the reading command. As shown in Fig.2-9. SCT initializes a reading command in step 1, where the OPAL-RT responses during step 2 based on received information. Once the responded information verified by the SCT, a writing command is sent out in step 3 subsequently. The entire communication is achieved when the same writing command is transmitted back to SCT from OPAL-RT at step 4.

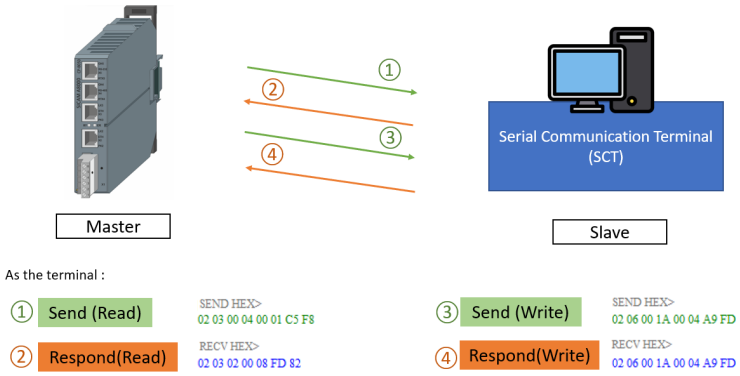


Fig.2-8 Communication between the Modbus RTU master (MGC) and Modbus RTU slave (SCT).

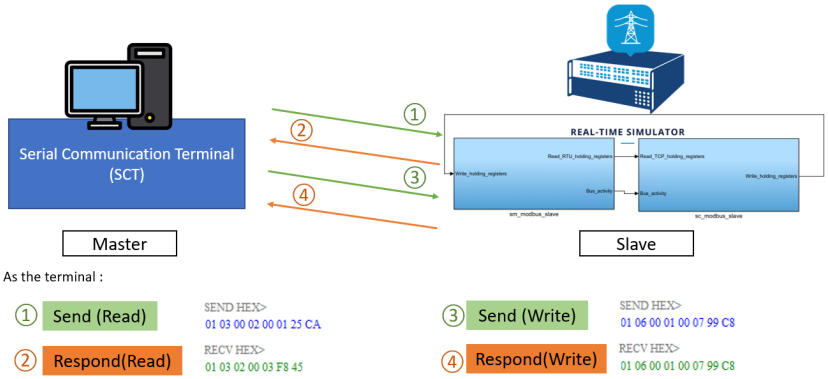


Fig.2-9 Communication between the Modbus RTU master (SCT) and Modbus RTU slave (OPAL-RT).

Moreover, Fig. 2-10 shows a simple read/write test between MGC and OPAL-RT. TLH.INV1.P.OUT is the reference setting value sent from the Modbus RTU master, MGC, and TLH.INV1.P.IN denotes the measurement data from Modbus RTU slave, OPAL-RT. In this test, the control reference was “4” and the measurement data was “7”.

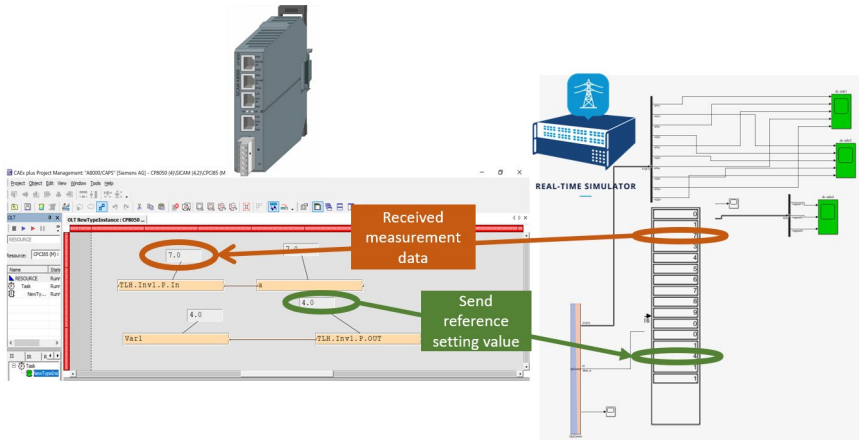


Fig.2-10 Modbus RTU communication between the Modbus RTU master (MGC) and Modbus RTU slave (OPAL-RT).

After all the testing, the outer loop can be finally implemented into the Siemens MGC CP8050. As shown in Fig. 2-1, the orange box and blue box refer to the outer loop controller in MGC.

**Subtask 2.4: Distribution system stability assessment**

In this subtask, the system stability assessment was carried out for outer-loop control developed in subtask 2.2. The system configuration is shown in Fig. 2-2. Since the uncertainty in the grid parameters, and the resistive load, and the current load disturbance are in the highest control level, the grid current controller is designed such that it robustly regulates the grid current. This is done by translating a robust control problem into an optimal control problem. The theoretical results provide gamma-dissipativity certificate along with a sufficient condition to design the controller. Define the grid current error by $\tilde{\imath}_g = i_g - i_{g0}$, where $\boldsymbol{i}_{g0}$ is the grid current at the operating point. Then, the uncertain open-loop dynamics is given by

$$\dot{\tilde{\mathbf{i}}}_g = -\frac{r_{g0}+r_{l0}}{l_{g0}}\left(\hat{\delta}+\Delta_g\right)\tilde{\mathbf{i}}_g - v_{dc0}\eta J\tilde{\mathbf{i}}_g + \frac{1}{l_{g0}}\tilde{\mathbf{v}}\left(\hat{\rho}+\Delta_v\right) + \frac{r_l}{l_g}\tilde{\mathbf{i}}_l, \tag{2-12}$$

where $\tilde{\boldsymbol{v}} = \boldsymbol{v} - \boldsymbol{v}_0$ , $\tilde{\boldsymbol{\imath}}_l = \boldsymbol{i}_l - \boldsymbol{i}_{l0}$, and $\boldsymbol{i}_{l0}, \boldsymbol{v}_0$ are the nominal current load and the nominal inverter voltage. Transferring the robust control problem above into an equivalent optimal control problem leads to the design of the optimal control law with the following form

$$\tilde{\boldsymbol{v}}^* = -\frac{\hat{\rho}}{l_{g0}} p\tilde{\imath}_g \tag{2-13}$$

, where $p$ is the solution of Algebraic Ricatti Equations (AREs) obtained by

$$p = \frac{-l_{g0}\left(r_{g0}+r_{l0}\right)\hat{\delta} + \sqrt{l_{g0}^2\left(r_{g0}+r_{l0}\right)^2\hat{\delta}^2 + 2l_{g0}^2\hat{\rho}^2 q}}{\hat{\rho}^2} \tag{2-14}$$

Using the dissipative system’s theory, and Hamilton-Jacobi-Bellman equation, finally the following sufficient condition is obtained:

$$q \geq \frac{c_g^2 \left(r_{g0} + r_{l0}\right)^2}{2\hat{\rho}^2} + \frac{1}{4\gamma^2} + 1, \tag{2-15}$$

In the above condition, given a $\gamma$, and the bound on uncertainties, the design parameter $q$ is determined that is used to design the optimal controller.

Figure. 2-11 shows the grid current error response when a current load disturbance occurs in the system. The disturbance is a signal with 100% current load step change from the nominal value the grid current controller is designed for. The current load disturbance occurs at t=0.5 sec and lasts for 1msec.

Figure. 2-12, shows the grid current error response of the IBR subjected to a uniformly distributed grid resistance, grid inductance, and load resistance variation. The parameters varied within the range of ±80% of their nominal values happening at t=0.5 sec and lasts for 0.5 sec.

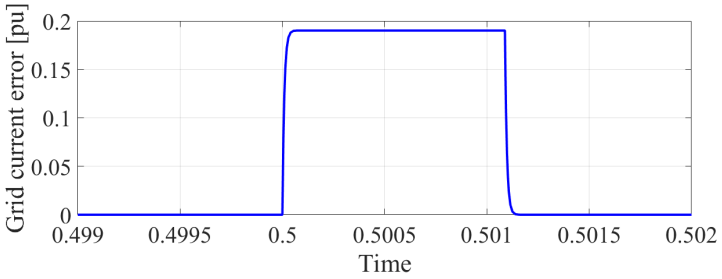


Fig. 2-11: Grid current error of the IBR subject to a pulsated current load disturbance

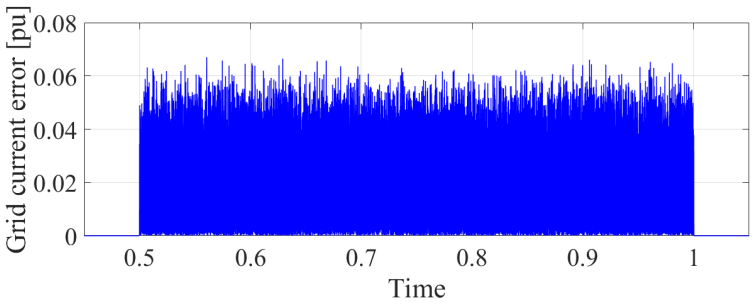


Fig. 2-12: Grid current error of the IBR subject to a uniformly distributed grid resistance, inductance, and the load resistance variation

The simulation results demonstrate that the current control tracking errors remain minimal under varying grid conditions, confirming the robustness and stability of the proposed control strategy.

**Subtask 2.5: Hardware acquisition for microgrid controller**

In this subtask, a hardware test bed is built aiming to verify the proposed UUCC's inner-loop control by FSU and UUCC's enhanced grid service, black start and grid-forming outer-loop control by Siemen's MGC. The developed test platform is shown in Fig. 2-13. It consists of a microgrid controller (MGC, SIEMENS CP8050), a Modbus RTU router, an inner-loop controller (PE-Expert4), and 2 R&D inverters (1 SiC-MOSFET inverter and 1 Si-IGBT inverter). The MGC sends the control commands and references (such as PQ references) to inverter inner-loop controller. The inverter inner-loop controller transfers the inverter ADC signals to MGC for outer-loop control purposes.

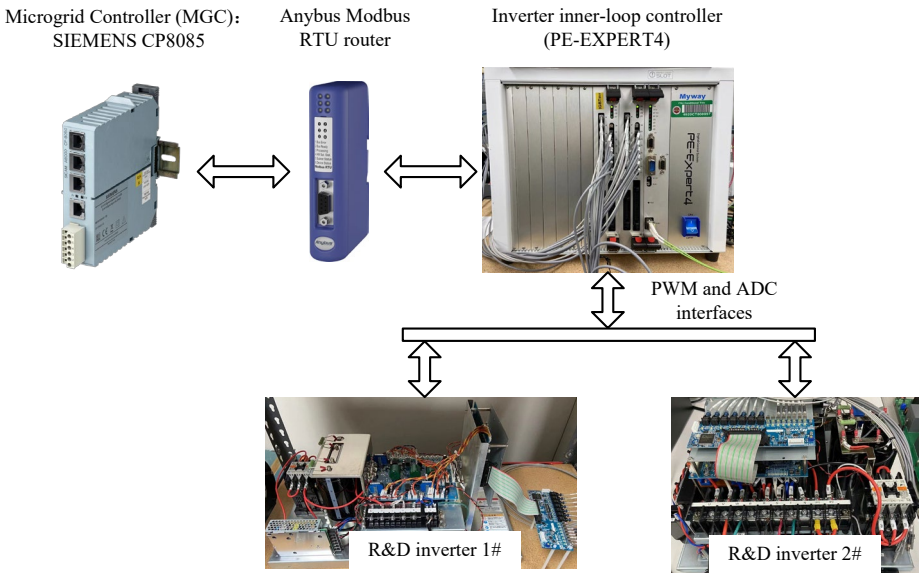


Fig. 2-13: Developed test platform to verify proposed UUCC's inner- loop control and grid-forming outer-loop control.

Modbus RTU was selected as the communication protocol since the inner-loop controller (PE-Expert4) is only compatible with it. The bi-directional communication of MGC as the Modbus RTU master and PE-Expert4 as the Modbus RTU slave is developed. More specifically, as shown in Fig. 2-14, MGC initializes a reading command in step 1, where the PE-Expert4 responses during step 2 based on received information at step 1. Once the responded information is verified by the MGC, a writing command is sent out in step 3 subsequently. A communication cycle of MGC as Modbus RTU master is achieved when the same writing command is transmitted back to MGC from PE-Expert4 at step 4. However, a significant communication delay between the Modbus RTU master and slave was observed during each cycle displayed in Fig.2-15. Fig. 2-15(a) refers to the inverter output active power and Fig. 2-15(b) indicates the received active power set-points on the inverter side. HIL results display unexpected oscillations which is cause by the communication delay. This delay will become worse when the number of Modbus RTU slaves increases.

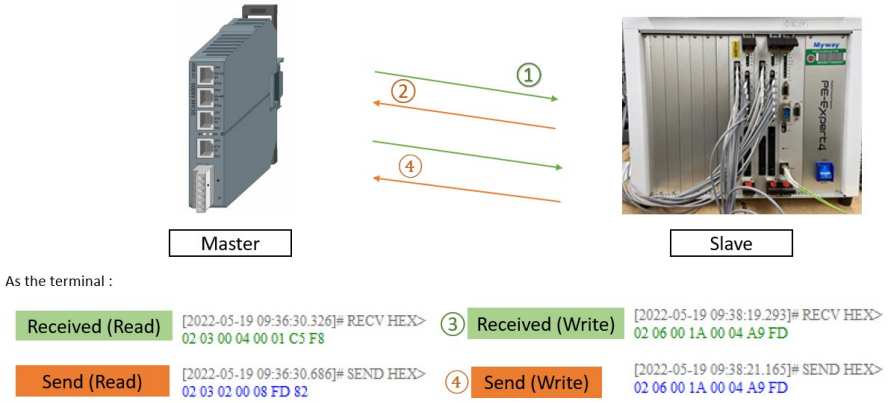


Fig. 2-14. Established bi-directional communication between MGC and PE-Expert4.

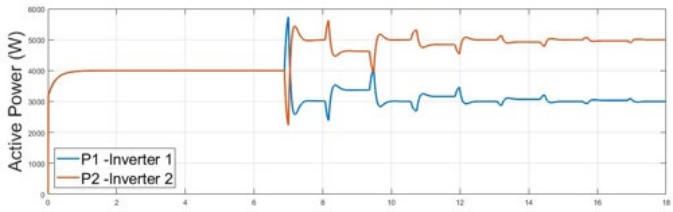


(a)

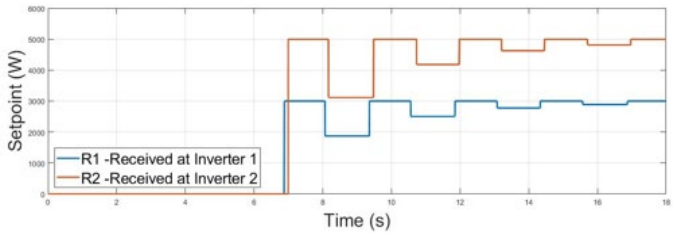


(b)

Fig. 2-15. HIL results for a microgrid consisting of 2 GFM inverters during islanded operation (a) active power output of inverter 1 and 2, (b) received active power set-points on each inverter.

## Task 3 Energy management controller design and development - Terminated at the end of BP1

| | ***Description*** |
|---|---|
| **T3** | **Task Name: Energy management controller design and development- Terminated at the end of BP1**<br>**Task Description:** We will modify existing regional 24 hr ahead PV power forecasting algorithms to be appropriate for predicting power at individual PV installations at specific geographic sites. Furthermore, a general methodology will be developed that will integrate the forecast result into energy management controller. Meanwhile we will identify typical operation scenarios including both a range of load profiles and market profiles for hybrid power plant, define cost terminology in regarding to economic($)/reliability needs as plant owner and design energy scheduling control algorithms. These operation scenarios will be applicable to different utility power purchasing agreements (PPAs). The controller will show > 5% cost improvement for at least one typical PPAs operating scenarios, compared to typical rule-based energy scheduled controllers. |
| **T3.1** | 24 hr ahead PV power forecast implementation, evaluation and assessment<br>**Completion in Q3-FY22:** Implemented **m**ethodology of 24 hr ahead PV forecast for specific geographic site of a PV installation, evaluated the PV forecast results, and assessed PV forecasts performance under classified local weather conditions and typical load profiles. |
| **T3.2** | Battery life-cycle and economic costs modeling and simulation.<br>**Completion in Q3-FY22:** Models and simulations of battery life-cycle and economic costs for energy storage that utilize different battery chemistries, DOD, operating temperatures or other discovered important influences. |
| **T3.3** | Energy scheduling control algorithms development and implementation.<br>**Completion in Q3-FY22:** Energy scheduling control algorithm to minimize the cost criteria and the PV forecast results of subtask 3.1 were integrated into the controller. |
| **M1.3.1** | Create 20-MW scale economic cost models that utilize different battery chemistries, DOD, operating temperatures.<br>**100% Completion:** The economic cost models for 20-MW power plant and simulation results considering various battery factors and solar farm factors. |

| | |
|---|---|
| **M1.3.2** | Showing > 5% cost reduction at least in one typical operation scenario compared to typical rule-based energy scheduled controllers.<br>**100% Completion:** > 5% cost reduation was achieved with the proposed control. |
| **Deliverables:** Energy scheduling control general algorithms. | |

**Subtask 3.1: 24 hr ahead PV power forecast implementation, evaluation and assessment**

This approach creates a short-term solar forecast by defining solar power index, SPI$(t)$, at time t. The SPI(t) represents the ratio between actual PV power, $P(t)$, and clear-sky power, $P_{CS}(t)$, as show in (1). The values are taken between 0 and 1. The clear-sky power $P_{CS}(t)$ and the expected clear-sky power $P_{CS}(t+\Delta t)$ at time change $\Delta t$ are calculated from System Advisor Model (SAM) with clear-sky GHI, DNI, DHI, and so on, (from NSRDB data viewer) as inputs, which indicates a calculated solar generation profile at certain time of the year and specified location by assuming an absence of clouds.

$$SPI(t) = min\,(P(t)/P_{CS}(t), 1) \quad (3\text{-}1)$$

Having defined the SPI, forecasted power $P_F(t+\Delta t)$ can be defined, which is power forecasted at time step $\Delta t$.

$$P_F(t+\Delta t) = P(t) + SPI(t) \times [P_{CS}(t+\Delta t) - P_{CS}(t)] \quad (3\text{-}2)$$

The plots in Fig. 3-1 (a) ~ (d) depict different forecast method and measurements for 24 hours on June 01, 2020. Fig. 3-1 (a) and (b) show the measured data compared to COT forecast and hour-ahead persistence forecast. Fig. 3-1 (c) and (d) show clear-sky solar power forecast and persistent forecast method with solar power clear-sky index for 24 hours.

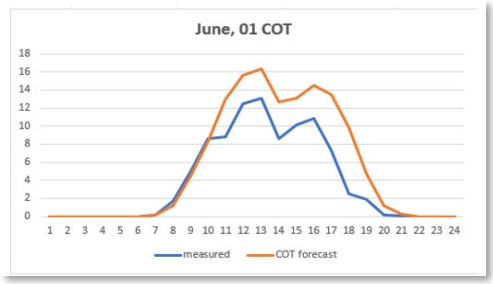


(a) Hourly Measured vs. COT forecast

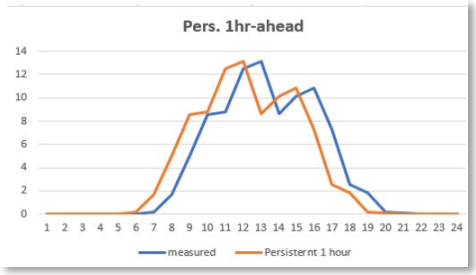


(b) Hourly Measured vs. persistent forecast

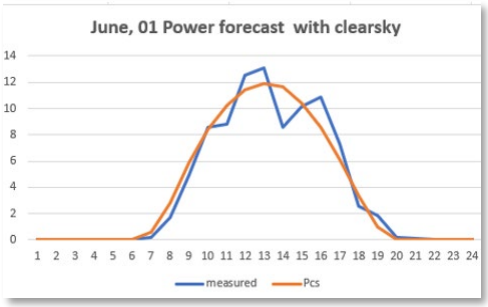


(c) Hourly Measured vs. clear-sky power

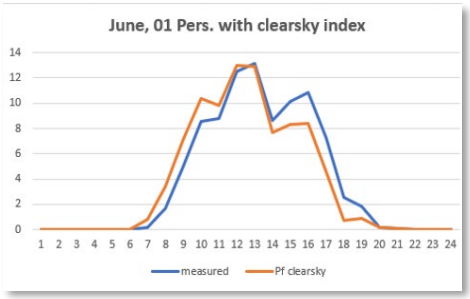


(d) Hourly Measured vs SPI prediction

Fig. 3-1: Forecast methods vs. measurements for 24 hours on June 01, 2020

In Fig. 3-2 (a) and (b), NMAE index and NRMSE index were used to evaluate these three forecast results for the entire year of 2020.

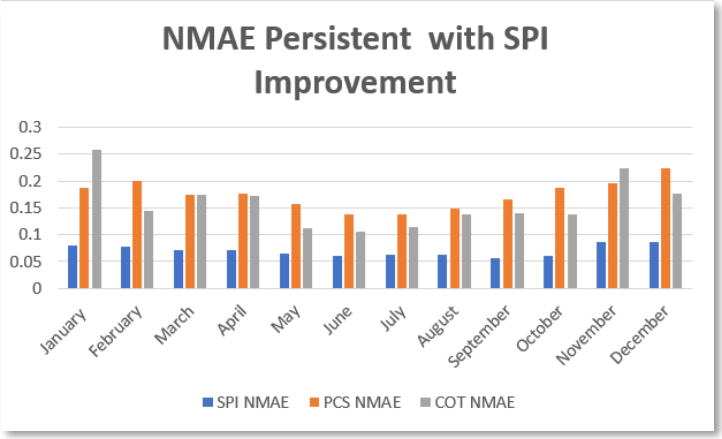


(a) NMAE index: COT, Clear-sky, and SPI prediction

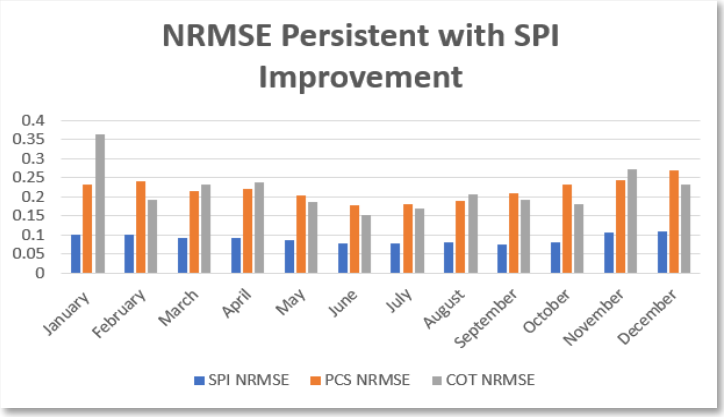


(b) NRMSE index: COT, Clear-sky, and SPI prediction

Fig. 3-2: Forecast result assessment

The result shows that among all 12 months of year 2020, solar power index-based forecast reduces hourly forecast error by 54% in NMAE, or 58% in NRMSE. The yearly averaged NMAE for this method is 7%, while the yearly averaged NMAE as shown in previous result is more than 15%. Similarly, the yearly averaged NRMSE of the SPI-based forecast is 9%, while the yearly averaged NRMSE of COT forecast is 22%.
SPI-based hourly forecast error is comparatively lesser than those other forecast approaches. This would be beneficial economically in terms of cost requirement, such as accurate battery sizing, reserves, carbon emission tax charges, and electricity market participation.

**Subtask 3.2: Battery life-cycle and economic costs modeling and simulation**
In conjunction with design input from City of Tallahassee Electric & Gas Utility (COT), the FSU & NU team has created MATLAB programs to help size the battery for the hybrid PV power plant that better utilizes the grid forming capabilities of the new inverters. As a proof of concept, an example of battery sizing process is done for a 20 MW solar farm reference model which is located at the property of the Tallahassee International Airport (TLH). The output power data of the solar farm 1 with 10s sampling rate for two years of 2020 and 2021 is used in the battery performance and cost optimization modeling (MATLAB). COT

has placed high value on grid-firming features for the hybrid inverters so that power fluctuations between the solar forecasted and the actual solar PV power have minimal impact on grid stability, especially short time period power fluctuations like 10 minutes or less that may cause frequency fluctuations in the grid.
The typical 20MW solar farm output power data has been showed in Fig. 3-3. This data has been used for the further processing to give sizing energy storage recommendations with the objective to match forecasted values of PV power to actual PV power, using the additional energy storage to smooth out the variations. The universal controller for the inverter would regulate the total energy management.

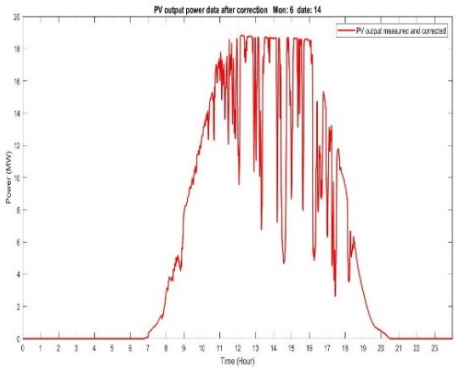


Fig. 3-3: Solar farm data COT 20MW PV plant

We define the PV error power which needs to be compensated by the battery (in this example it has been calculated for every 5 minutes) as:

$$Error\ Power\ (P_e) = P_{avg\_5min} - P_{hourly_{forecast}avg} \quad (3\text{-}3)$$

As of now, it is assumed that $P_{hourly_{forecast}avg}$ is 100% accurate, since this research is just developing the methodology and simulation program. The MATLAB program designed evaluates the improvements in $P_e$ with battery vs. without battery for the different size batteries. This simulation tool will allow COT and other utilities to properly size the grid forming inverters when solar forecasting and the unique grid forming features are implemented into the hybrid PV power plant.
As an example, a 10 MW, 5 MWh battery is simulated to provide energy storage to the 20 MW COT existing PV array. Without the energy storage, the $P_e$ is plotted in Fig. 3-4.

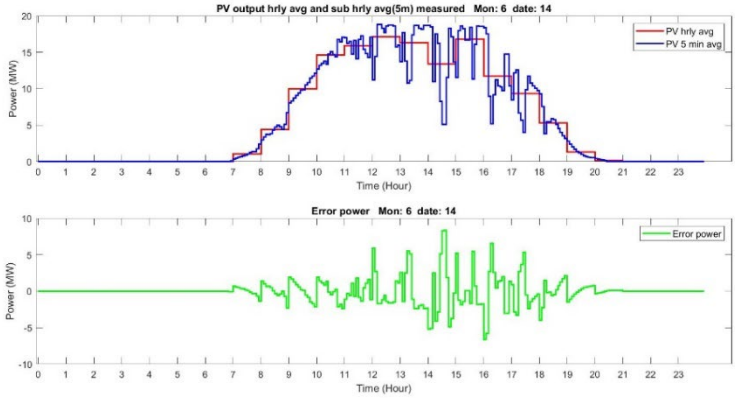


Fig. 3-4: Solar farm output power hourly avg, 5-minute avg., and error power (without energy storage)

Assume that the battery can be charged from the grid or discharged to the grid during the non-solar irradiance time to achieve its 50% SOC starting charge at early morning hours. Then when the 10 MW, 5 MWh battery is added to the PV power plant, Fig. 3-5 demonstrates that the $P_e$ becomes zero for almost all data points. This is due to the fact that the energy is released to the grid when the PV forecast is too low compared to the actual PV power. Similarly, the extra solar energy above the forecast is absorbed into the battery. The one small time interval in which the PV power substantially exceeds the forecasted power (15:30) is due to the fact that the battery is fully charged and cannot accept the additional PV power. To deal with this, solar PV curtailment may be implemented, but it is not yet programmed into the existing MATLAB simulation program.

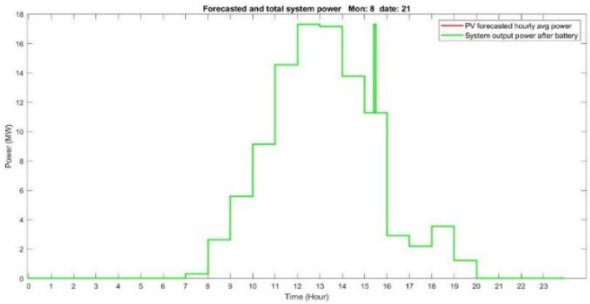


Fig. 3-5: Solar farm's hourly forecasted power and total power when 10MW, 5MWh battery is added to the PV array.

The simulation program is now being used to help size the COT future PV installations and to demonstrate the cost benefits of adding the energy storage in conjunction with the new inverters.

**Subtask 3.3: Energy scheduling control algorithms development and implementation**

A dynamic programming (DP)–based load scheduling algorithm was applied using actual load forecast data from the City of Tallahassee (COT). This scheduling strategy was executed over the course of one year, demonstrating its effectiveness in optimizing generator usage. The results indicate that the proposed DP-based algorithm significantly enhances the contribution from high-efficiency combined cycle (CC) generators while reducing reliance on internal combustion (IC) generators. This shift leads to a measurable reduction in the hourly operating cost of the COT power grid. The structure of the DP-based load scheduling algorithm is illustrated in Fig. 3-6. The hourly operating cost under conventional COT load scheduling is presented in Fig. 3-7 for comparison. Further, Fig. 3-8 shows the results of applying the DP-based scheduling to the same grid, this time incorporating a utility-scale battery. The integration of battery storage further reduces the grid's hourly operating costs, highlighting the potential benefits of combining DP scheduling with energy storage solutions.

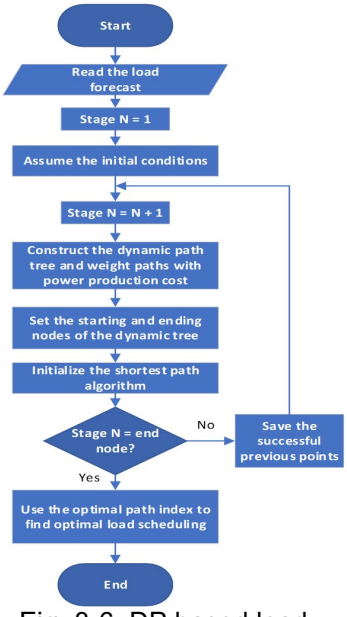


Fig. 3-6: DP based load scheduling algorithm

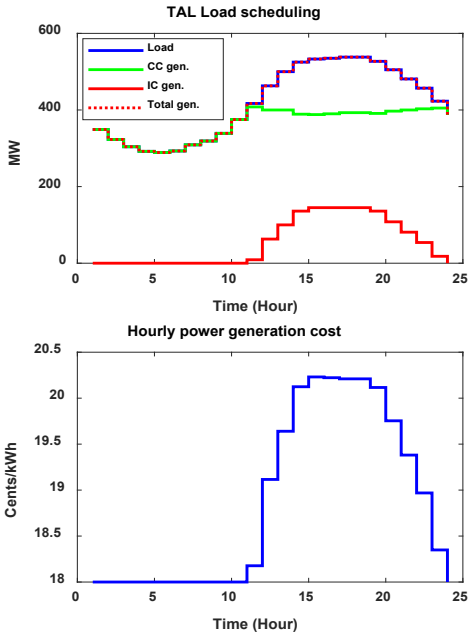


Fig. 3-7: TAL load scheduling and generation cost/kWh

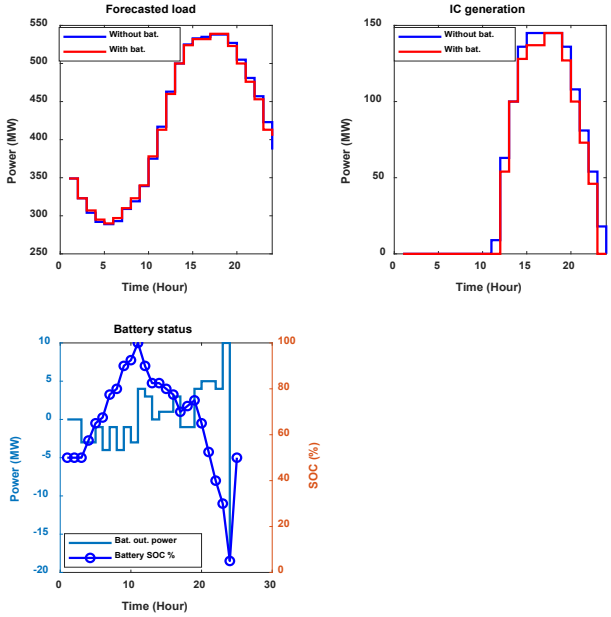


Fig. 3-8: DP based load scheduling

## Task 4 Control and use-case development on 1-MW at-scale test platform - Terminated at the end of BP1

| | ***Description*** |
|---|---|
| **T4** | **Task Name: Control and use-case development on 1-MW at-scale test platform-Terminated at the end of BP1**<br>**Task Description:** We will entail identification of use cases and development of controller architecture on 1-MW at-scale test platform in both grid-following and grid-forming modes. |
| **T4.1** | Plant configuration modeling and controller architecture development<br>**Completion in Q3-FY22:** The configuration of the hybrid power plant to support the grid forming and following resources was identified and modelled. |
| **T4.2** | Use-case development for evaluation and validation.<br>**Completion in Q3-FY22:** The use-case was identified to validate various services and controls developed for both grid-forming and grid-following modes of operation. |
| **M1.4.1** | Controller architecture identified and full control integration pathway defined.<br>**100% Completion:** Finalized full control architecture along with steps for how all the system control as well as inner and outer loop controls will be integrated. |

**Subtask 4.1: Plant configuration modeling and controller architecture development**
This section of the report summarizes the overall comparative control architecture for two parallel connected PV and battery inverters in a microgrid. The overall control architecture is based on virtual inertia with an outer droop loop to ensure operation under grid-following modes of operation. The simplified control block diagram is presented in Fig. 4-1, the other controller takes the same form only the virtual inertia is replaced with a standard proportional integral (PI) control like the reactive power loop.

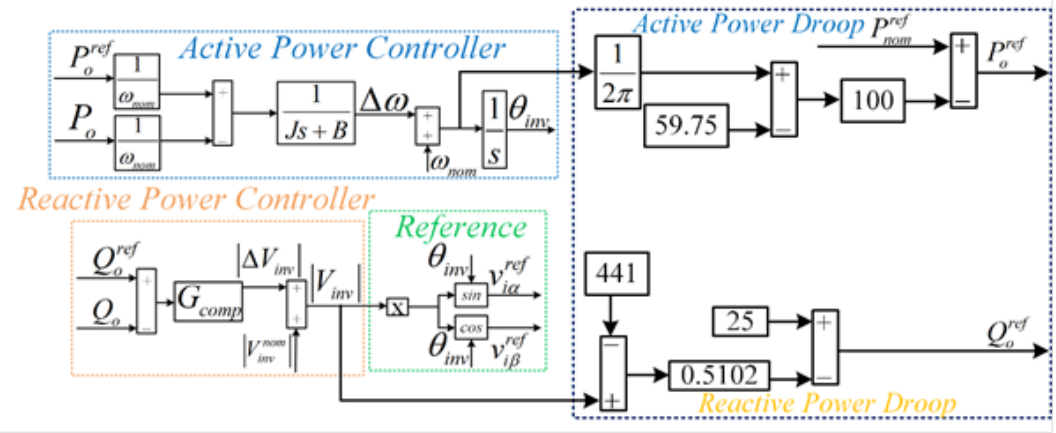


Fig. 4-1: Simplified block diagram schematic for the overall control architecture

The overall droop curves followed has been quantitatively presented in Fig. 4-2 and Fig. 4-3.

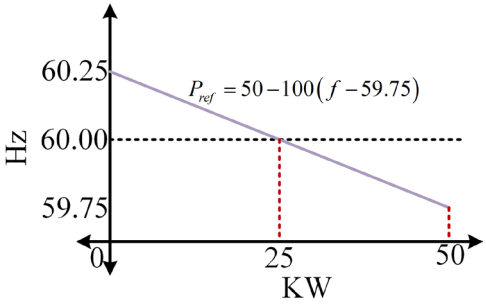


Fig. 4-2: Active power droop

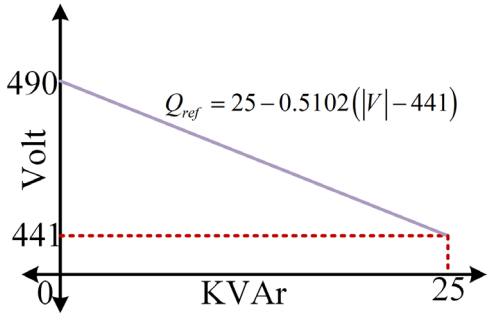


Fig. 4-3: Reactive power droop

**Subtask 4.2: Use-case development for evaluation and validation**

Based on subtask 4.1, the overall system was simulated, and various case study results are presented showing the performance of the overall system. For the whole study two parallel connected PV + battery inverter system have been used as presented in the simplified block diagram of Fig. 4-4 where one of the converters is operating as a PV the other one as a supporting battery converter.

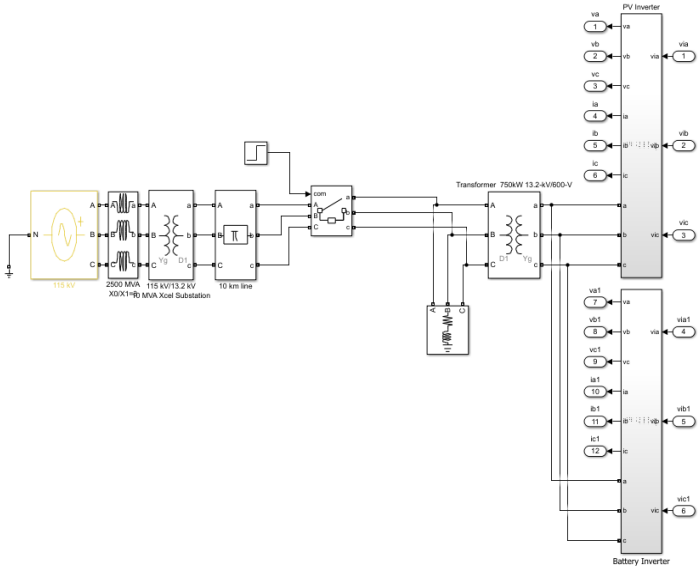


Fig. 4-4: Simplified block diagram of the parallel connected PV + battery system

The result showing the steady state performance with the two types of control architecture (one presented in Fig. 4-1 and the other with using PI for the active power loop like the reactive power) for grid following mode is presented respectively in Fig. 4-5 through Fig. 4-8.

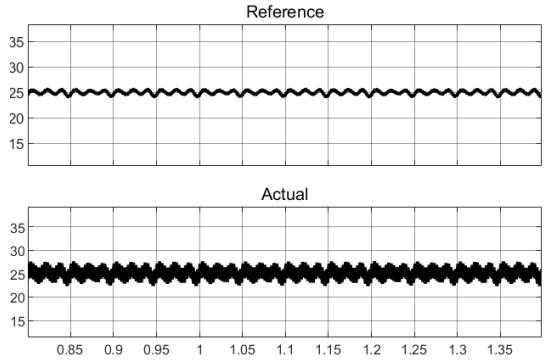


Fig. 4-5: PV converter steady state power with virtual inertia-based control architecture

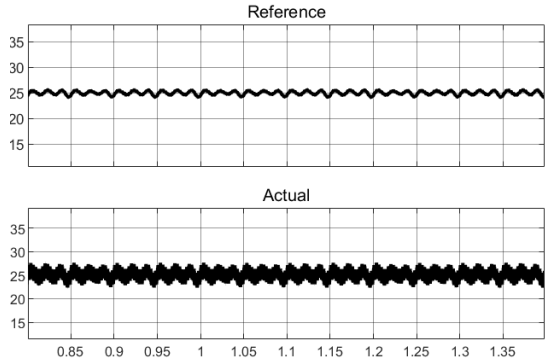


Fig. 4-6: Battery converter steady state power with virtual inertia-based control architecture

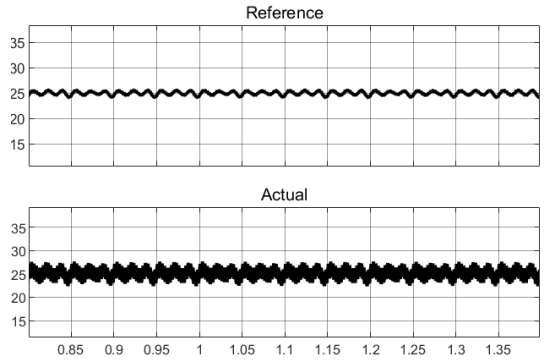


Fig. 4-7: PV converter steady state power with PI control-based architecture

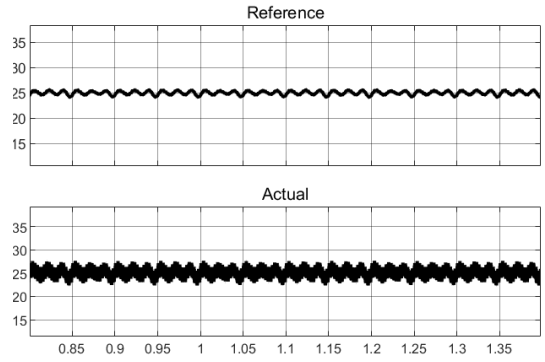


Fig. 4-8: Battery converter steady state power with PI control-based architecture

As observed from the results in Fig. 4-5 through Fig. 4-8 that the steady state performance remains similar for all the cases. Next the result for these converters for a transient in the active power are respectively presented in Fig. 4-9 through Fig. 4-12.

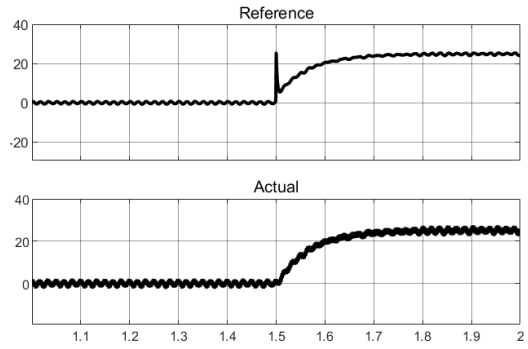


Fig. 4-9: PV converter step change in active power with virtual inertia-based control architecture

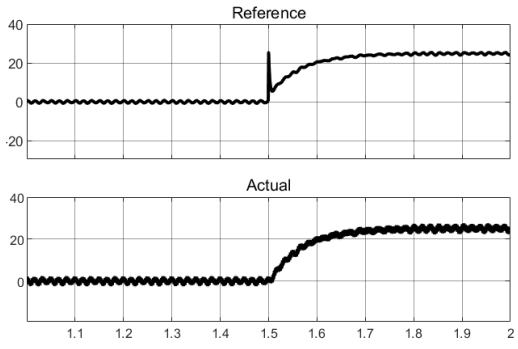


Fig. 4-10: Battery converter step change in active power with virtual inertia-based control architecture

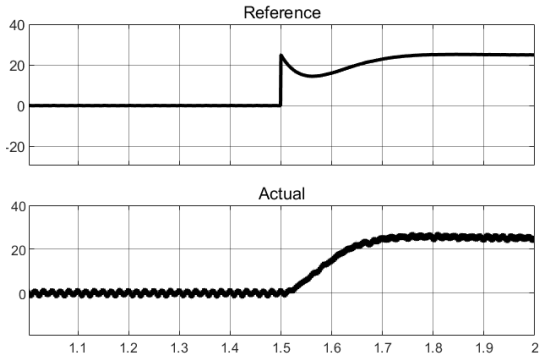


Fig. 4-11: PV converter steady state power with PI control-based architecture

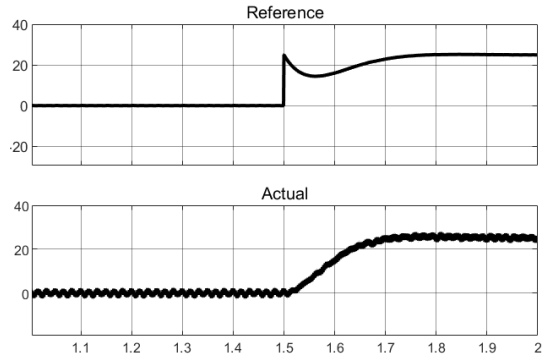


Fig. 4-12: Battery converter steady state power with PI control-based architecture

From the results presented in Fig. 4-9 through Fig. 4-12 it is observed that when there is virtual inertia-based control, the performance can be optimized based on the choice of the inertia and damping constants. However, with traditional PI controller, it becomes difficult to optimize the performance. The result for the grid voltage and current for the above case studies are respectively presented in Fig. 4-13 through Fig. 4-16.

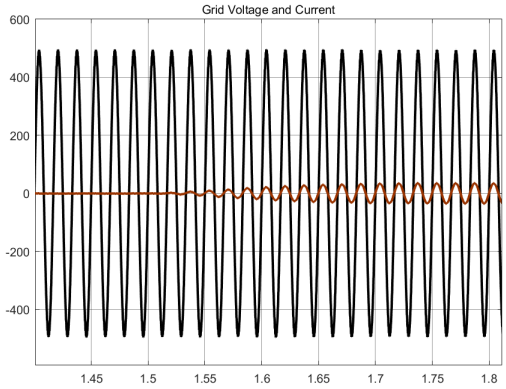


Fig. 4-13: Grid voltage and current for the PV converter with virtual inertia-based control architecture

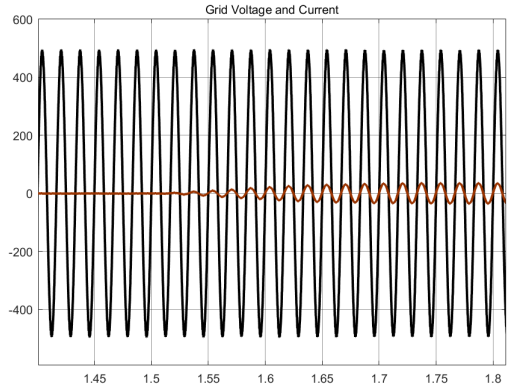


Fig. 4-14: Grid voltage and current for the battery converter with virtual inertia-based control architecture

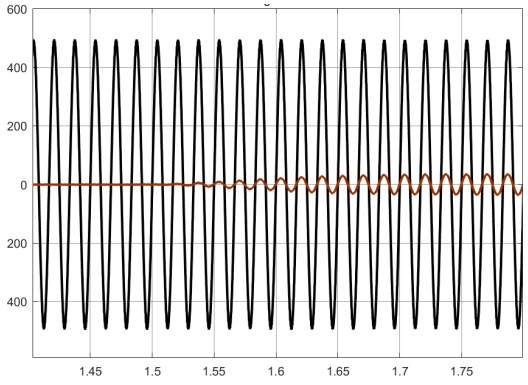

Fig. 4-15: Grid voltage and current for the PV converter with PI controller-based architecture

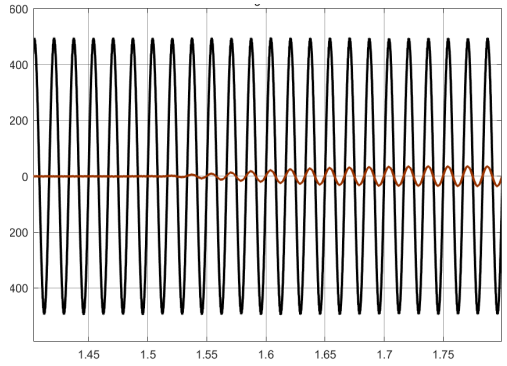

Fig. 4-16: Grid voltage and current for the battery converter with PI controller-based architecture

The results show similar performance for the grid voltage and current. As mentioned before, all the above results are presented for the grid following mode of operation. The next set of results are presented for grid forming mode where these converters are supplying some critical standalone loads. The result showing the transition of grid-following mode to grid-forming mode are presented next.

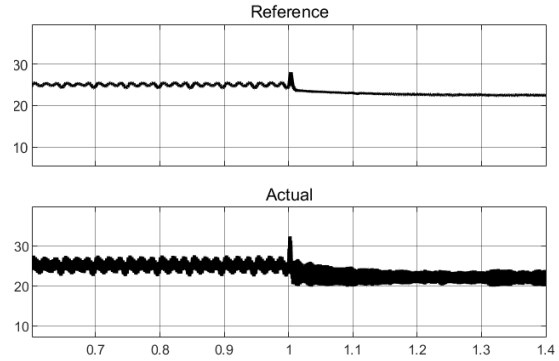


Fig. 4-17: Active power during transition from grid following to forming for the PV converter with VI based control

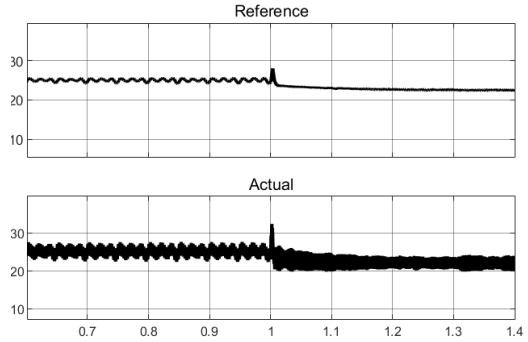


Fig. 4-18: Active power during transition from grid following to forming for the battery converter with VI based control

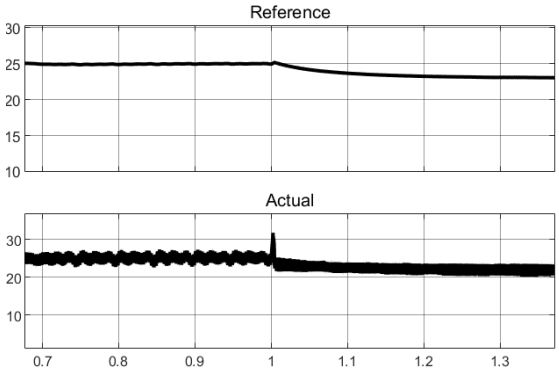


Fig. 4-19: Active power during transition from grid following to forming for the PV converter with PI based control

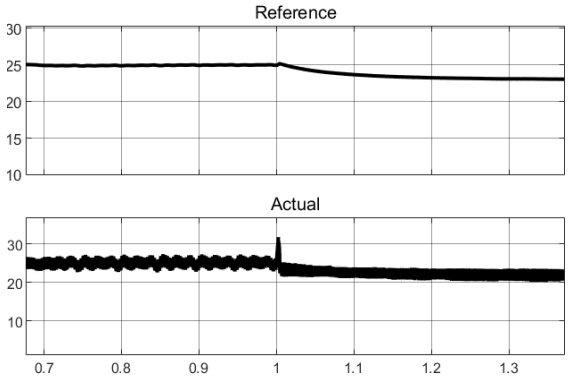


Fig. 4-20: Active power during transition from grid following to forming for the battery converter with PI based control

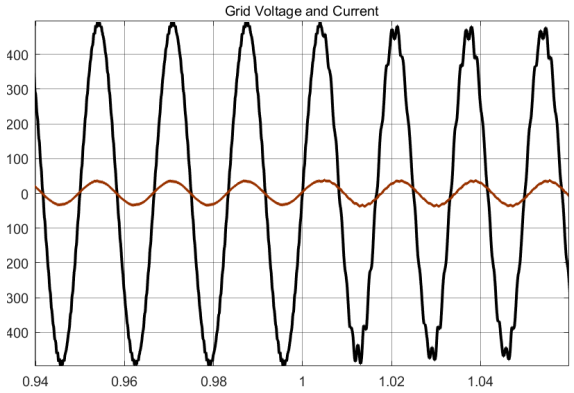


Fig. 4-21: Grid voltage and current for transition from grid following to forming with VI based control architecture for the PV converter

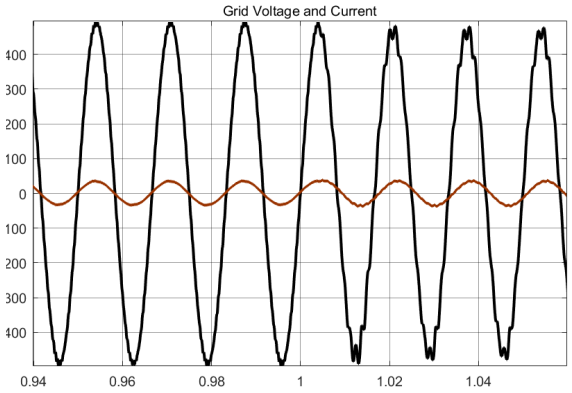


Fig. 4-22: Grid voltage and current for transition from grid following to forming with VI based control architecture for the battery converter

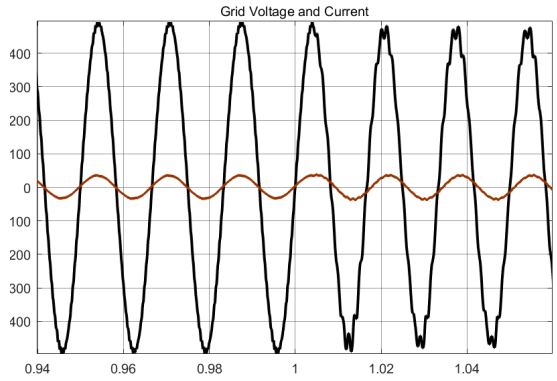


Fig. 4-23: Grid voltage and current for transition from grid following to forming with PI based control architecture for the PV converter

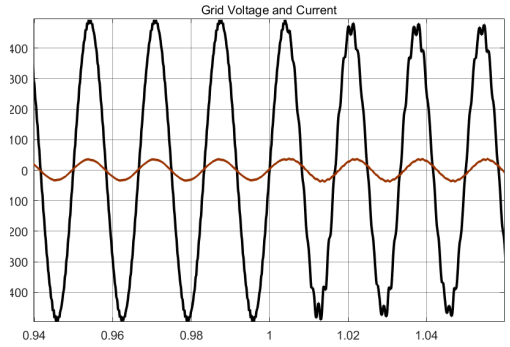


Fig. 4-24: Grid voltage and current for transition from grid following to forming with PI based control architecture for the battery converter

From these results it is observed that the system can seamlessly transition from grid following to grid forming mode of operation. The last set of results present the voltage and currents for the grid following to forming mode of operation.

The result for the transient load change in grid forming mode are presented in the next set of results

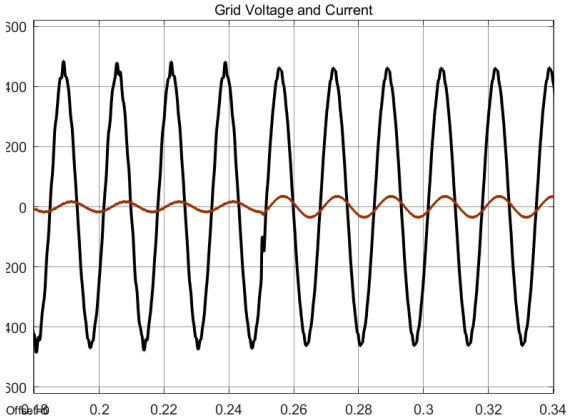


Fig. 4-25: Step change in load with VI based control architecture for PV converter

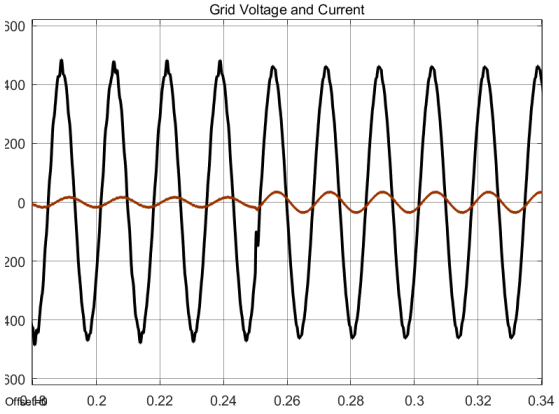


Fig. 4-26: Step change in load with VI based control architecture for battery converter

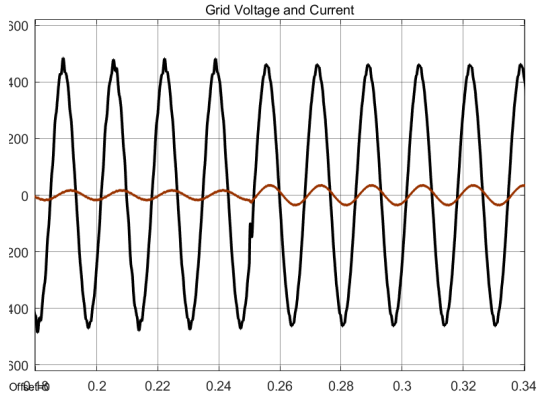


Fig. 4-27: Step change in load with PI based control architecture for PV converter

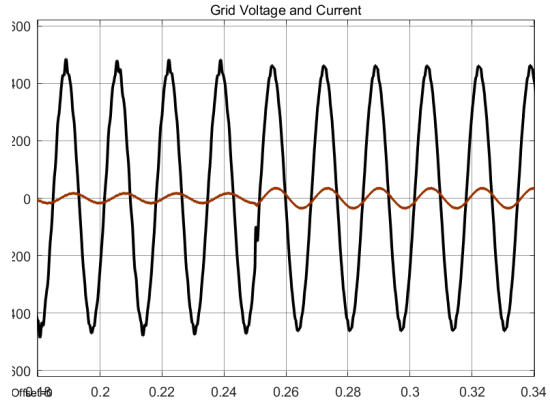


Fig. 4-28: Step change in load with PI based control architecture for battery converter

The results present the comparison between the reported architecture for a part of big microgrid system with different resources. Several other case studies as well as corner cases are explored to understand the operation and controllability for the overall system.

### Go/No-Go and Deliverables

| | *Description* |
|---|---|
| **GNG-1A** | Inner-loop controller design. |
| **GNG-1B** | Outer-loop controller design |
| **Deliverables:**<br>UUCC Yearly Report – BP1<br>Inner-loop controller simulation model, software code and hardware design schematics<br>Energy scheduling control general algorithms | |

### Task 5 UUCC's inner-loop control implementation and lab validation.

| | *Description* |
|---|---|
| **T5** | **Task Name: UUCC's inner-loop control implementation and lab validation.**<br>**Task Description:** In this task, the switching-cycle-based inner-loop control method will be implemented and validated in lab environment. |
| **T5.1** | Inverter control software development<br>**Completion in Q3-FY23:** Developed VR based inner-loop control software for GFL inverters under unbalanced grid conditions. |
| **T5.2** | UUCC's inner-loop control implementation and lab validation<br>**Completion in Q4-FY23:** Implemented GFL control algorithms with VR based inner-loop code and validated GFL operation experimentally in the lab. |
| **M 2.5.1** | Grid-tied inverter hardware and inner-loop controller software implementation.<br>**100% Completion:** Built testbed and implemented control software to test GFL operation. |
| **M 2.5.2** | UUCC's inner-loop controller lab validation under 3%-30% distribution system impedance, 100% load changes.<br>**100% Completion:** Conducted GFL experiments under different grid impedance and 100% load change. |

### Subtask 5.1: Inverter control software development

In this subtask, the inner-loop control algorithm was developed considering unbalanced grid conditions. Additionally, a transient-less transformer energization at GFL mode was proposed to suppress the inrush current for GFL inverters.

5.1.1 Inner-loop control algorithm under unbalanced grid conditions

Based on the voltage unbalance definition offered by the National Equipment Manufacturer's Association (NEMA), a simplified computational approach is presented. This methodology is designed to align with other recognized standards, including those set by IEEE, ensuring a coherent framework for assessing voltage imbalances. The IEEE Standard consolidates recommendations from ANSI, IEC, and EN, advocating that the voltage imbalance in a three-phase system should not exceed 3%. This study considers scenarios with a 3% voltage imbalance to represent extreme conditions.

Let the voltage imbalance be denoted as δ%. According to the NEMA definition, this imbalance is calculated by the ratio of the maximum deviation of each phase voltage peak from the average magnitude to the average value itself. The analysis then proceeds to examine the deviation between the estimated phase angle and the actual value. The

actual phase angle can vary from 0 to 2π, which models a startup event that could happen at any point during grid voltage operation. The study spans each phase angle from 0 to 2π.

Fig. 5-1 illustrates the error in estimating phase angles across various voltage imbalances, ranging from 0.6% to 3%, considering different initial phase angles. The findings highlight a notable discrepancy in the sine of the estimated and actual phase angles, peaking around 0.015 at either 90° or 270°. This deviation translates to a maximal phase angle difference of approximately 9°, which remains within the acceptable range for synchronization processes, as per the standards set by IEEE, specifically mentioning the synchronization criteria without exceeding the 10° threshold. Moreover, comparisons with prior research reveal our observed phase difference is less than the previously reported 11° maximum, underscoring the relative insignificance of a 0.01 difference in sine values for practical applications where typically only the sine or cosine values are of concern.

The analysis further indicates that the impact of voltage imbalance, denoted as δ, on phase angle estimation is minimal, as illustrated by the overlapping data lines in Fig. 7-1. It suggests that scenarios exceeding the studied voltage imbalances might not be relevant for this discussion, as system protections could preempt inverter activation, thus remaining outside the purview of this investigation. Additionally, the study supports the premise that inrush currents, which are significantly influenced by a 180° phase difference, are likely to be minimal in this context. Our findings show a maximum phase difference well below 10°, hinting at potentially lower inrush current scenarios, aligning with the initial hypothesis presented earlier in the text.

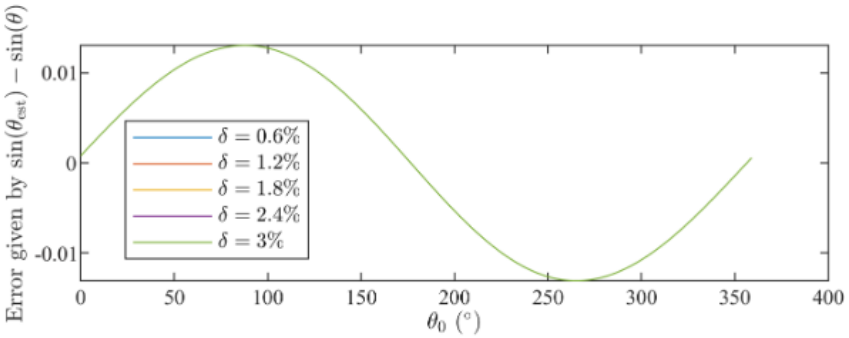


Fig.5-1. Error Analysis of Phase Angle Estimation Across Voltage Imbalances: A depiction of the error in phase angle estimation (sin θ_est vs. sin θ) for voltage imbalances ranging from 0.6% to 3%, highlighting the maximum discrepancy observed at specific phase angles (90° and 270°).

### 5.1.2 Transient-less Transformer Energization for GFL inverters

A transient-less transformer energization method is developed for GFL inverters to control the excitation flux based on pre-fluxing and virtual resistance. Fig. 5-2 shows a three-phase transformer energized by an inverter, where the pulse-width modulation (PWM) signals are generated by the current control loop. For the inverter with a supply voltage of amplitude $U_m$ and a phase angle $\alpha$, the electromagnetic transient equation for the starting process is:

$$U_m \sin(\omega t + \alpha) = N\frac{d\emptyset}{dt} + iR \tag{5-1}$$

where $\emptyset$ is the transformer core flux, $R$ is the resistance of the primary side of the transformer, and $N$ is the turns of the primary side windings of the transformer.

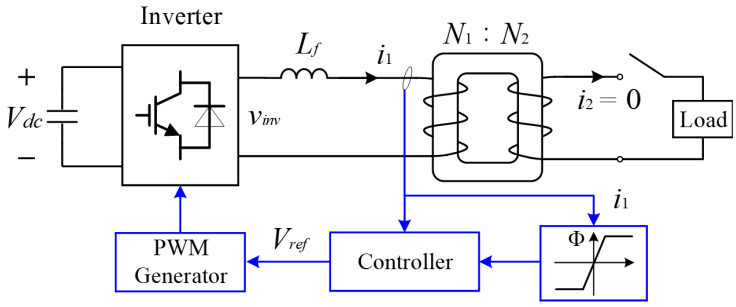


Fig. 5-2. Transformer pre-fluxing and virtual resistance control for transformer energization.

Since the initial transformer flux is not easy to obtain according to previous analysis, a transformer pre-fluxing is proposed to change the transformer flux by maintaining the switching state of the inverter bridge to allow DC voltage to be applied to the primary side of the transformer. As shown in Fig. 5-2, the transformer flux is magnetized to a positive or negative saturation value (according to the initial transformer flux state) to provide a defined initial flux. The output reference of the inverter is represented by

$$\begin{cases} \boldsymbol{V_{ref}} = \boldsymbol{V_t(t)}, & if\ \emptyset\ is\ saturated \\ \boldsymbol{V_{ref}} = \boldsymbol{V_c}, & if\ \emptyset\ is\ unsaturated \end{cases} \quad (5\text{-}2)$$

where $V_c$ is a constant larger than 1 and will not cross the carrier.

Fig. 5-3 shows the simulation waveforms, where the blue lines are the transformer energization transient when the inverter starts without flux control and the brown lines are the inverter starts with flux control. Fig. 5-3(a) shows the flux control method based on previous detection of the inverter output voltage. Fig. 5-3(b) shows the flux control method based on pre-fluxing and virtual resistance. The initial remanent transformer flux is 0.8. In this scenario, the transformer flux is pre-fluxing to the positive saturation state to provide a defined initial flux. The simulation results show that the inrush current during the transformer energization process can be effectively mitigated when the transformer flux has been controlled to start with the matched voltage phase angle.

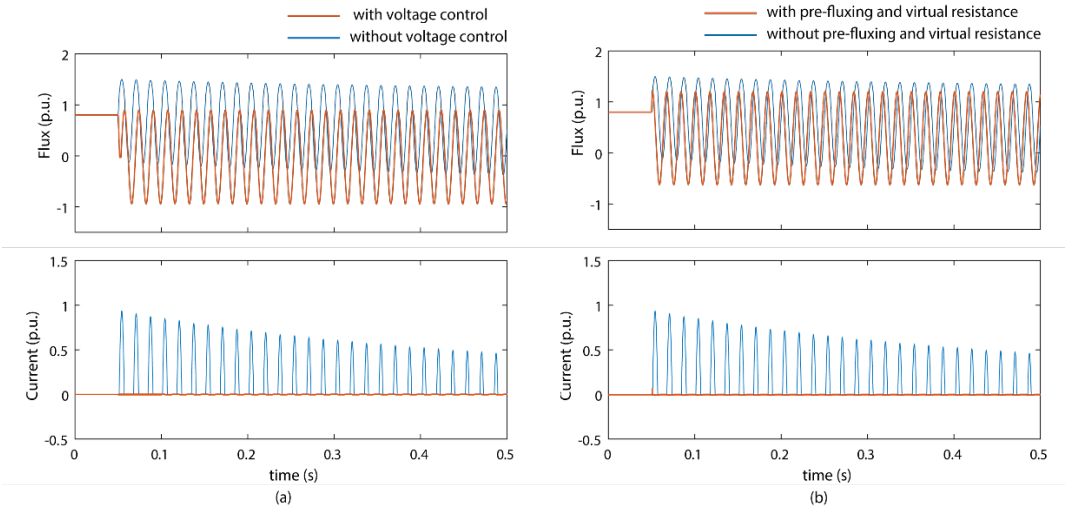


Fig.5-3. Simulation results (flux of transformer and current) of the grid-connected inverters with single-phase transformer energization. (a) Comparison results of voltage control (b) Comparison results of pre-fluxing and virtual resistance control

**Subtask 5.2: UUCC's inner-loop control implementation and lab validation**

In this subtask, the inner-loop control strategy was implemented and experimentally verified under GFL mode. Additionally, the transformer energization method for GFL inverters was also validated through testing.

5.2.1 GFL operation validation under unbalanced grid conditions.

To verify the effectiveness of GFL performance based on VR inner-loop control, the experimental testbed was built, as shown in Fig. 5-4.

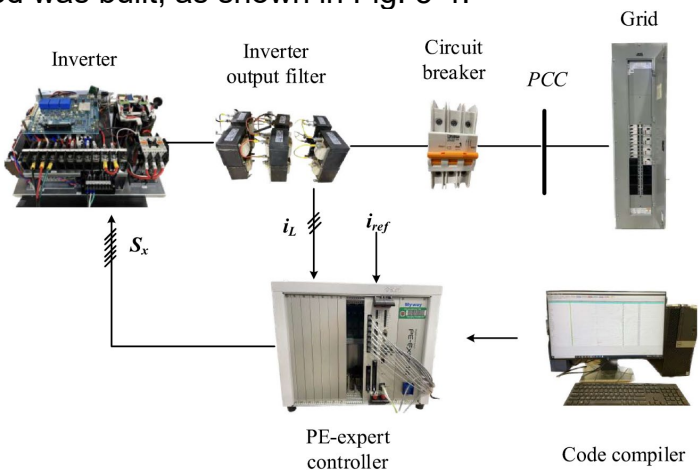


Fig.5-4. Experimental setup for GFL operation.

Fig. 5-5 presents the GFL experimental results for connecting the inverter to the grid, with a switching time of only 200 μs per state. The method achieves successful connection in just two switching cycles, requiring a total of 400 μs. The top subfigures display the phase currents $i_a$ and $i_b$, represented by the blue and red curves, respectively, while the gating signals of the phase a upper switch and the phase b upper switch are illustrated by the green and orange curves, respectively. The bottom subfigures show the three-phase grid voltages $v_{ga}$, $v_{gb}$, and $v_{gc}$, represented by the blue, red, and green curves, respectively. The purpose of monitoring these voltages is to demonstrate the successful four-quadrant startup of the proposed method. However, they are not utilized in the control process. Notably, the proposed startup method's key feature is the utilization of only current for the startup, as demonstrated in this study. In Fig. 5-6, the switching duration is depicted at 100 μs. The current peak during the startup for this duration is noticeably lower than that observed for the 200-μs scenario. Furthermore, in both the cases, the currents remain well below the rated value.

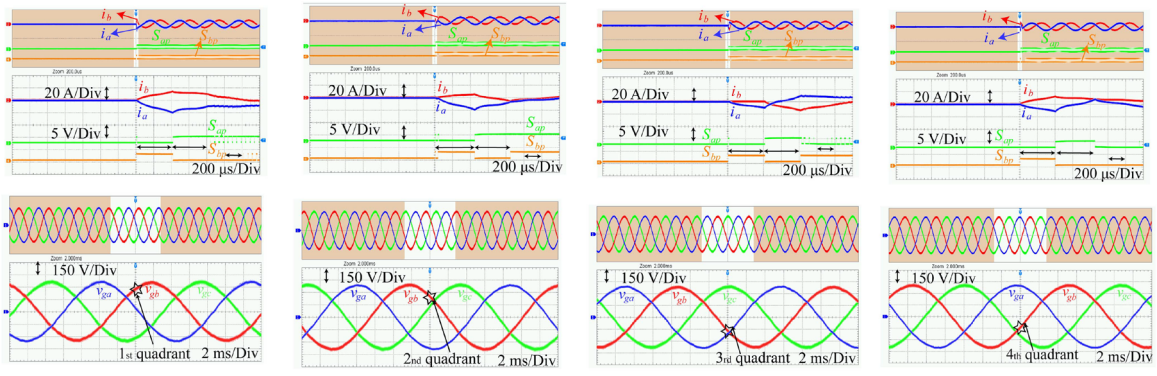


Fig.5-5. (a)–(d) Experimental results of GFL mode under the switching duration at 200 μs.

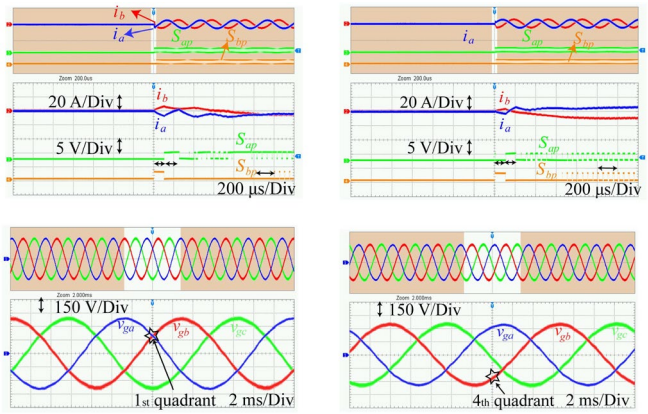


(a) (b)

Fig.5-6. Experimental results of GFL mode under the switching duration at 100 µs for synchronization (a) at a positive grid voltage cycle and (b) at a negative grid voltage cycle.

During the GFL inverter connected to the grid process, the phase a current ($i_a$) initially decreases, while the phase b current ($i_b$) increases due to the first switching state being 011. However, to reduce the peak current magnitude, a complimentary switching state (100) is employed in the subsequent switching cycle. This results in an increase in the phase a current and a decrease in the phase b current in the second switching cycle. After the two switching cycles, the grid voltage is calculated and obtained, causing the control loop to transition to the current control to the rated current. The entire process achieves synchronization within 200 µs, without any inrush current occurring.

All the experiments were performed by connecting the inverter directly to a practical power grid, rather than an ideal ac source or grid simulator. This indicates that the grid voltage inherently has some harmonics. Fig. 5-7 showcases the harmonic components of the grid at different frequencies, with a THD of 5.6%. This affirms the applicability of our proposed method even in the presence of grid harmonics. In addition, the practical grid voltage is not perfectly balanced, displaying a 4% imbalance, as depicted in Fig. 5-8. Despite this, the GFL inverter connected to the grid process remains free of inrush current and achieves synchronization within just two switching cycles.

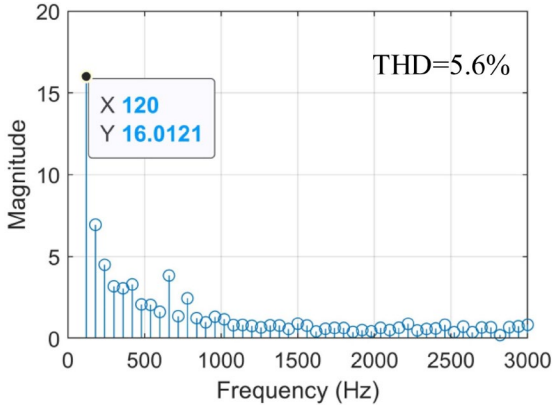


Fig.5-7. Harmonic magnitude of grid voltage in relation to frequency, ranging from the second harmonic (120 Hz) up to the 50th harmonic (3000 Hz).

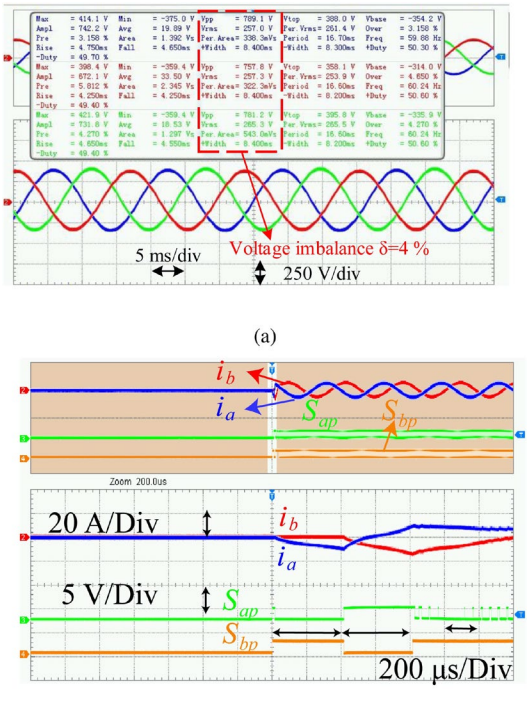


Fig.5-8. (a) and (b) Experimental results of GFL inverter connected to the grid under 4%grid voltage imbalance.

### *5.2.2 Instant transformer energization based on virtual resistance control in GFL mode*

FSU constructed a testbed to test transformer energization in GFL mode that specifically assess the characteristics of the inrush current. The test circuit is shown in Fig. 5-9(a). The SiC inverter is connected to a three-phase transformer through the L filterer. The rated voltage at the primary side of the transformer is 208 V. Fig. 5-9(b) shows test waveforms of transient inrush current and inverter output voltage during transformer energization. It can be seen that from the instant of the output voltage $V_{inv}$ of the inverter, large inrush currents occur in the transformer. Particularly, the inrush currents in the opposite direction of phase A and phase B are as high as 20 A. After a few tens of milliseconds, the transformer current decays to zero.

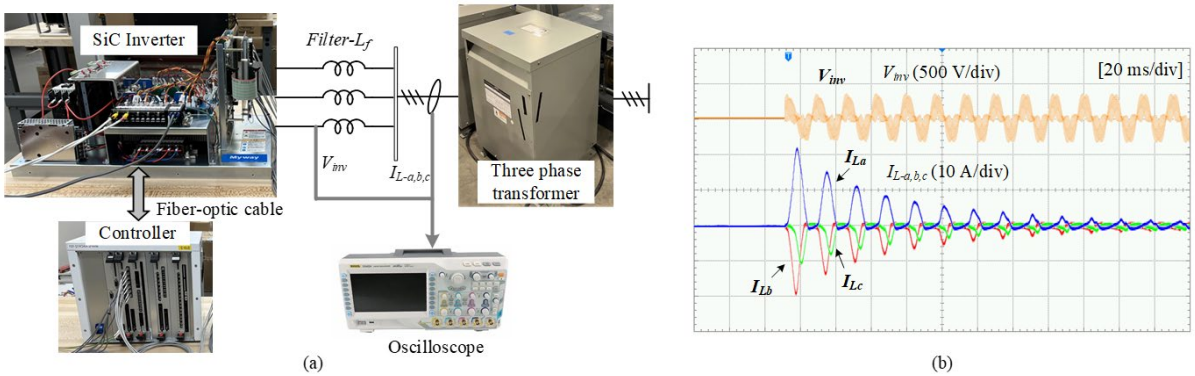


Figure 5-9: (a) Experimental test circuit under GFL mode. (b) Test waveforms of transients for transformer energization under GFL mode.

We proposed a novel approach to energize a transformer using IBR with GFL operation by switching cycle-based direct current control. Zero-inrush current can be achieved by virtual resistance control. The inverter startup voltage phase angle is determined based on the active damping to make sure that no dc component will be induced when energizing the transformer. The proposed control method will allow the timeliest adjustment of the inverter's behavior to mitigate the inrush current for a transient-free transformer energization. Fig. 5-10 shows the energization of a transformer using an inverter to verify the effectiveness of the proposed strategy. The simulation result of energizing the transformer without virtual resistance control is shown in Fig. 5-10. Its transients coincide with the test waveforms in Fig. 5-9(b). It can be seen that a very high bias component is generated in the transformer flux curve and the transformer inrush current rises up to 2 pu. When virtual resistance control is applied, as shown in Fig. 5-11, the transformer inrush current can be effectively reduced to 0.06 pu due to the approximate matching of the starting angle of the inverter with the transformer flux, then the inrush current of the transformer can be rapidly attenuated to zero within several switching cycles.

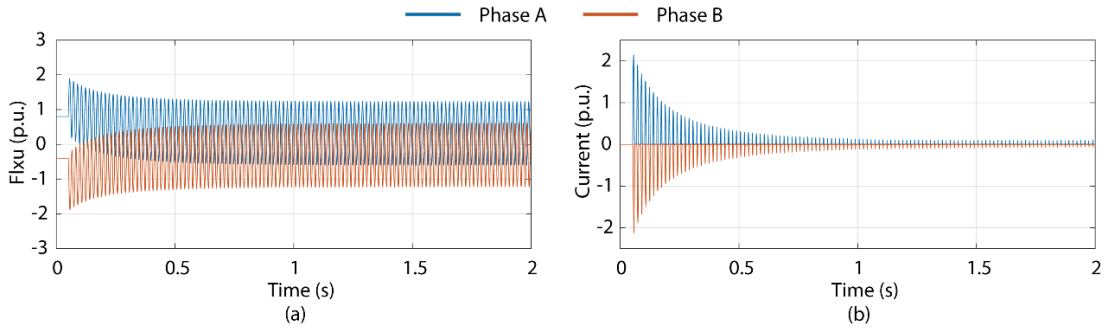


Fig. 5-10: Waveforms of transformer phase A and phase B without virtual resistance control. (a) Transformer core flux. (b) Transformer current.

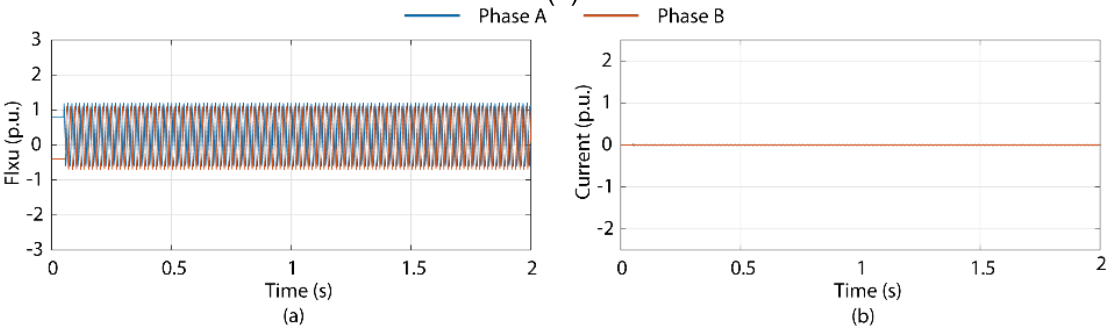


Fig. 5-11: Waveforms of transformer phase A and phase B with virtual resistance control. (a) Transformer core flux. (b) Transformer current.

## Task 6 Develop black start functions for hybrid plant

| | *Description* |
|---|---|
| **T6** | **Task Name: Develop black start functions for hybrid plant**<br>**Task Description:** This task includes the development of black start functions for PV plus battery hybrid plant. We will develop two black start operation logics, 1. to restore the service to islanded system, and 2. to synchronize and reconnected to bulk power system (BPS), respectively. The black start functions will be implemented in a microgrid controller. |

| | |
|---|---|
| | (Note: This Task is described for information only. The work effort for conventional black start in Task 6 and its applicable subtasks will be incorporated into development of the ultrafast black start described in Task 7, below). |
| **T6.1, 6.2** | Black start of a hybrid power plant for local restoration.<br>Synchronization and reconnection of hybrid power plant to utility-power system<br>**Completion in Q3-FY24:** Developed black start operation logic for a hybrid power plant including re-synchronization with grid, inrush current control and overload protection. |
| **T6.3** | Implement black start functions in microgrid controller.<br>**Completion in Q3-FY24:** Implemented black start logic in Siemens microgrid controller. |

**Subtask 6.1: Black start of a hybrid power plant for local restoration**
**Subtask 6.2: Synchronization and reconnection of hybrid power plant to utility-power system**

The black starting of inverter-based resources (IBRs) consist of several aspects. This includes: (1) re-synchronization with grid (2) controlling inrush current (3) overload protection. In subtask 6.1 and 6.2, Siemens team developed solutions for these aspects of black starting based on their past project experience.

1. Grid re-synchronization

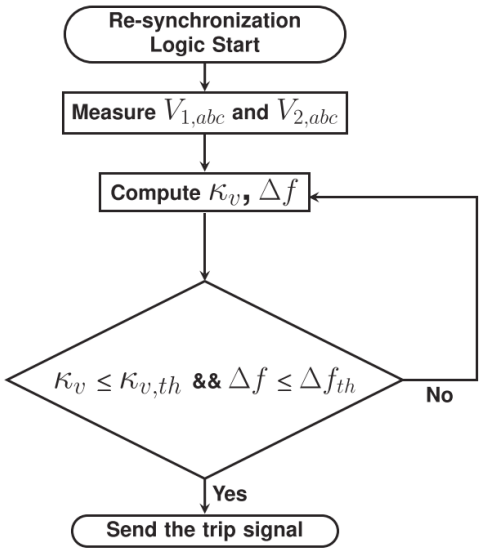


Fig. 6-1 Re-synchronization logic

During black starting of IBRs, it is important to ensure synchronization of frequency and voltage with the grid before closing the breaker to ensure successful grid restoration after blackout. We suggest re-synchronization logic as shown in Fig. 6-1. In the figure, $V_{1,abc}$ and $V_{2,abc}$ are 3-phase measurements at the grid side and the inverter side, respectively. These measurements are used to compute voltage difference factor, $k_v$, and frequency difference, $\Delta f$. The breaker should remain open as far as values of $k_v$ and $\Delta f$ are more than their threshold values, $k_{v,th}$ and $\Delta f_{th}$, respectively.

The threshold value, $k_{v,th}$ is obtained based on transient current, $I_{tr}$ as follows: $k_{v,th} = I_{tr}|Z_i|$. Where $Z_i$ is the impedance between two voltage sources which would be dominated by filter impedances in the absence of the line impedance, typically ranging in 0.1 to 0.3pu, while $I_{tr}$ can be determined by inverter's maximum current, typical design value is 1.1 to 1.2 pu. On the other hand, $\Delta f_{th}$ is obtained using following relation: $f_{th} = \frac{k_{v,th}}{2\pi T_r}$, where $T_r$ is switch response time.

2. Inrush current control in PV + Battery system (Siemens' background IP)

Compared to conventional generators, power electronic devices are much more fast-acting, and has the potential to black start a system in seconds compared to hours using conventional generators. However, due to the physical constraints of semiconductor switches, the inverters can only provide current within its limit. To black start a system (either transmission, distribution, or behind the meter), transformer and induction machine can incur starting inrush current with high magnitude over short period of time which over drives capacity of the inverter. Whether a grid forming inverter can be used to black start depends on the current rating as well as accurate information of the system, e.g. how much start current will incur.

In practice, the black start of a grid forming inverter is carried out manually where experienced operator decides a fixed voltage reference ramp rate based on his/her past experience with particular inverter system. The reference rate is chosen more conservatively to avoid current over drives. This is known as soft start. As a result, black start can take more time than actually requires under optimal condition. Thus, as shown in Fig. 6-2., we suggest adaptive changes in voltage ramp rate based on real-time information as contrast to fixed ramp rate.

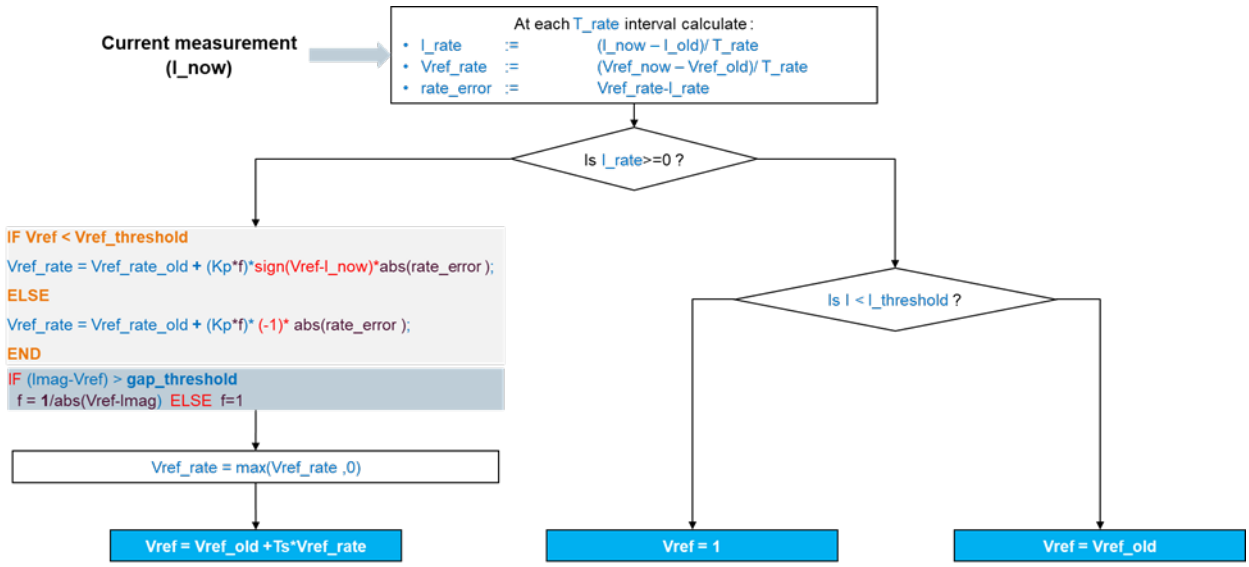


Fig. 6-2. Proposed black start algorithm for pu (per unit) system.

In our past research project, above algorithm is used for hybrid PV and battery systems. Both PV and battery inverters are operated in grid forming mode. The inverter connected to battery is operated as with adaptive Vref as in Fig. 6-2 while PV inverter is controlled at fixed bus Vdc voltage. The grid is represented by induction motor. The algorithm is verified in simulation using induction motors of different characteristics. It was observed that proposed algorithm is able to provide Vref such that the inrush current peak remain within 1pu for all considered cases. Note that for all cases same tuning parameters are used. Thus, it can be concluded that the proposed algorithm has a potential to scale across different system without manual intervention.

3. Overload detection and disablement process

In order to smooth black start, it is important to monitor overload while enabling load connection and If overload condition is detected then load disable process must be initiated to avoid any instability/blackout. Thus, we suggest overload detection logic as shown in Fig. 6-3. The figure describes flowchart of the proposed detection logic. Idea behind the logic is that in case of overload, bus voltage drops significantly. Thus, whenever bus voltage drops below the boundary of the peak phase voltage, $v_{lim}$, it triggers overload detection. However, it is important to differentiate between voltage drop due to the transient and due to the actual overload condition. Thus, as soon as voltage drops more than $v_{lim}$ it starts accumulator process and triggers load disablement process if and only if accumulator value reaches to $N_{tho}$. Note that $N_{tho}$ is function of the nominal fundamental frequency, the desired number of cycles to wait after large load detected, and data communication delay.

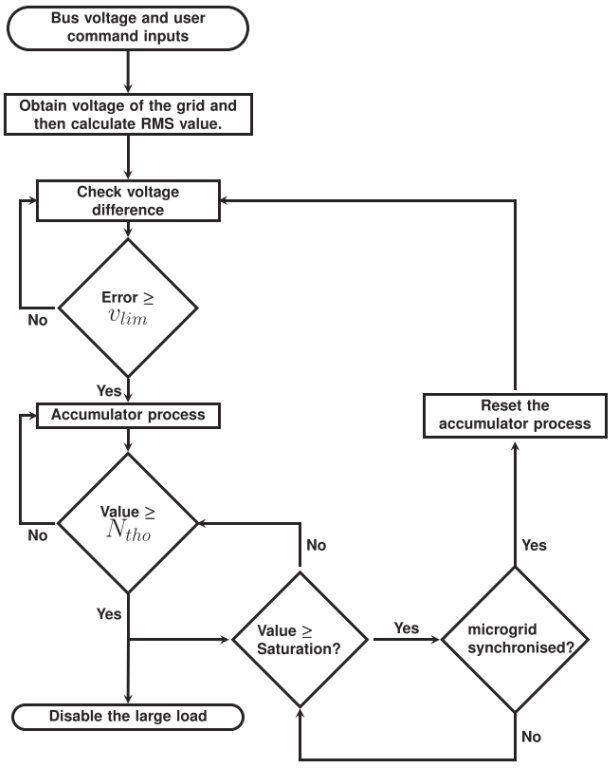


Fig. 6-3. Overload detection logic

**Subtask 6.3: Implement black start functions in microgrid controller**

Siemens built a microgrid at its Princeton NJ office that has black start functionality. This system is a microgrid integrated with building management system, not only provides power to the Siemens office building, but also serves as a living laboratory for researching and demonstrating new technologies. The Living Lab consists of an 836 kWp photovoltaic (PV) system, a 1MWh/500kW energy storage system, a microgrid controller and six power inverters (four PV inverters and two battery inverters), an Automatic Transfer Switch, six Siemens electric vehicle (EV) chargers and a Siemens cloud-based solution,

integrated into a grid-tied microgrid capable of optimizing both supply and demand through transactive energy controls. The single line diagram of the microgrid is shown in Fig. 6-4.

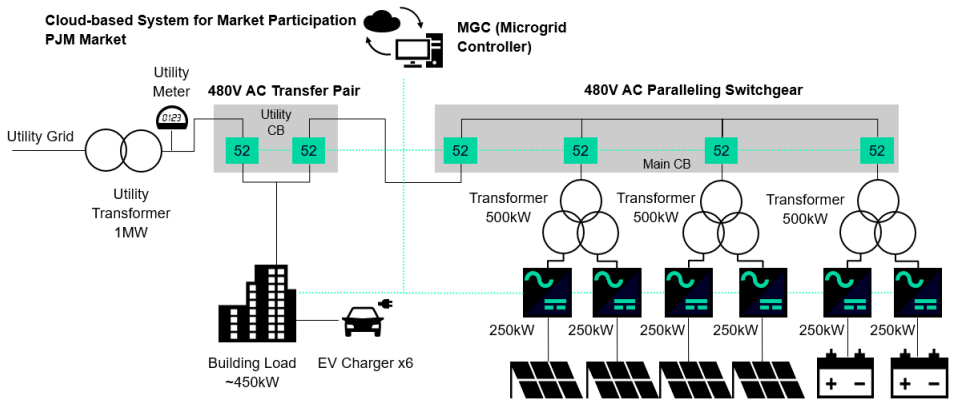


Fig. 6-4: Single Line Diagram of Siemens Princeton Microgrid

There are six grid-connected inverters which can operate in either grid-following or grid-forming mode. During normal operation when utility grid is available, the microgrid is operating in grid-following mode. When an unpredicted event like power outage happens, the inverters will switch to grid-forming mode, and the microgrid will operate in islanded-mode without the main utility grid. An automatic transfer switch is enabling the safe disconnection and reconnection of the microgrid back to the utility grid and smooth transition between grid-forming and grid-following modes. Whenever there is a power outage, the protection relay will automatically detect the loss of grid and send a command to the Microgrid Controller. The Microgrid Controller will then coordinate the inverters to operate in grid-forming mode and support power to the building. The transition is seamless and building tenants will not notice any power disruption.

In case of a more severe power outage, system will need to execute the sequence of operation for black start. Since normal building load is between 350kW – 500kW, we first start the two battery inverters in grid-forming modes and send set point of 250kW to both inverters. We will close the circuit breaker for the main building, while keeping the utility breaker open. The building management system will then power up the loads in the building based on their preset priority. The number of loads which can be connected would depend on the State-of-Charge (SoC) of the battery. If battery SoC is higher, more loads can be connected. Once the system stabilizes, the four PV inverters will be connected in grid-following modes. When the system stabilizes, all loads can be connected safely. The system will then operation in islanding mode, while waiting for grid power to be restored.

Microgrid Control, a SICAM application product offered by Siemens Smart Infrastructure, has functionality related to blackout detection and black start.

A blackout in the public grid can be detected automatically; to ensure the microgrid's stability, it must disconnect from the public grid. This disconnection can be performed automatically, manually or per schedule.

In worst case, when supply of the public grid is lost, a black start sequence is required to power up the microgrid again. This preconfigured sequence can be initiated by command or by automated blackout detection. Microgrid Control automatically detects blackout events and step-by-step starts the generation devices and/or connects the loads depending on success of the previous step. By this procedure, a maximum degree of security and reliability of energy supply is ensured.

When the public grid becomes available again, Microgrid Control can reconnect automatically if a synchronization unit is available.


Fig. 6-5. Microgrid Control automated measures for Blackout and fault detection

In case an automatic black-start is not possible or is not desired, Microgrid Control can support a manual black-start process by providing information about actual spinning reserve and predicted load.

In this project, the black start and synchronization functionality is centrally coordinated by a Siemens CP-8050 device, which is part of the SICAM A8000 automation platform. It runs the SICAM application Microgrid Control (MGC) and up to three custom-written SIAPP container-based applications. MGC monitors data from each inverter and sends commands to turn them on during the black start procedure. MGC also monitors the status of a relay and commands it open or closed to connect the two inverters together during the synchronization step.

Deploying a SIAPP to the SICAM Application Runtime (SIAR) environment is described in the SICAM 8-Engineering manual. The following is a high-level summary of the SIAPP deployment steps using SICAM Device Manager:

Step 1: Assuming a project with a CP-8050 device has already been created in order to run MGC, the first step in SIAPP deployment is to add a SIAPP Runtime to the CP-8050.
Step 2: If TCP / IP communications with external applications are needed, configure the port(s) over which the SIAPP will communicate.
Step 3: To communicate with MGC or other SIAPPs, create signals and map them to the relevant SIAPP.
Step 4: Import the packaged SIAPP file to SICAM Device Manager.
Step 5: Assign the imported SIAPP to a runtime slot.
Step 6: Upload the SIAPP to the CP-8050 and begin execution.

## Task 7 Ultrafast black start of PV + battery hybrid power plant

| | *Description* |
|---|---|
| **T7** | **Task Name: Ultrafast black start of PV + battery hybrid power plant**<br>**Task Description:** To develop an ultrafast black start algorithm that can fully utilize the fast response and instant synchronization feature of the proposed switching-cycle-based inner-loop control. The targeted black start times as specified in Table. 1. The developed ultrafast black start will be implemented and validated in a hybrid PV + battery power plant environment. |
| **T7.1** | Development of ultrafast black start algorithm based on the switching-cycle-based inner-loop control<br>**Completion in Q4-FY24:** Developed innovative ultrafast black start algorithms based on the deadbeat method and mitigated inrush current when energizing the transformer during the black start process. |
| **T7.2** | Experimental implementation and validation of ultrafast black start based on switching cycle-based inner-control<br>**Completion in Q1-FY25:** Implemented the deadbeat-based GFM control on a single SiC inverter and tested ultrafast black start in the islanding mode. |
| **T7.3** | Simulation validation of a realistic 100-kW PV-battery hybrid plant for the ultrafast black start.<br>**Completion in Q1-FY25:** Developed a simulation model of a 100 kW HPP plant and simulated the ultrafast black start using the proposed VOC-based GFM method and VR-based GFL control. |
| **M 2.7.1** | Simulation validation of a hybrid plant picking up local loads within the capacity of the plant, and establishing acceptable voltage (within 0.917 - 1.05 p,u,) and frequency (within 59.5 – 60.1 Hz) set points.<br>**100% Completion:** Simulation models were developed. The simulation results verified that the two proposed ultrafast black start algorithms established the voltage and frequency setpoints with minimum steady state errors. |
| **M 2.7.2** | Simulation validation of a hybrid plant synchronized and reconnected to a realistic distribution/sub-transmission system.<br>**100% Completion:** The simulation results verified that the two proposed ultrafast black start algorithms synchronized and reconnected to the grid significantly faster than targeted goals. |
| **M 2.7.3** | Implement UUCC's outer-loop black-start control algorithm on microgrid controller for hybrid plant.<br>**100% Completion:** A black start algorithm was implemented on microgrid controller for hybrid plant. |
| **M 2.7.4** | Black start hardware and software implementation.<br>**100% Completion:** A testbed was built in the lab to evaluate black start of a single SiC inverter. Ultrafast black start of deadbeat-based GFM control in islanding mode was tested experimentally using the developed testbed. |

### Subtask 7.1: Development of switching-cycle based ultrafast black start algorithm

FSU teams developed a deadbeat-based ultrafast black start algorithm that can achieve switching-cycle control. Additionally, a transformer energization technique has also been designed to suppress the inrush current during black start process.

1. Deadbeat based GFM control with ultrafast black start and instantaneous synchronization capability

Fig 7-1 shows the proposed deadbeat-based GFM control. This control strategy is mainly composed of the V/f regulation and deadbeat current controller.

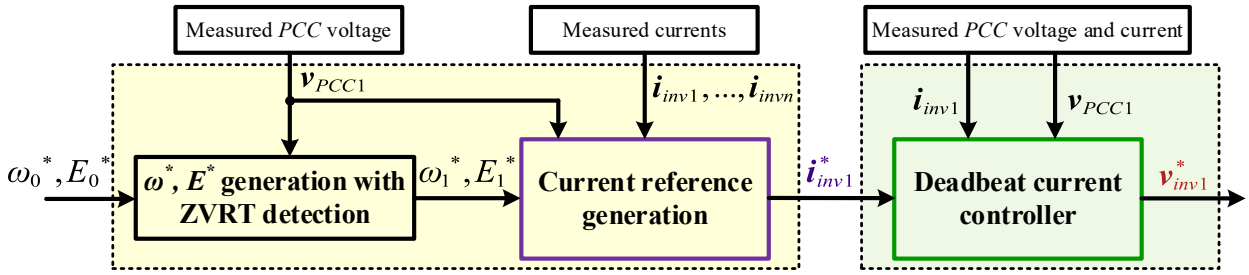


Fig 7-1 Proposed deadbeat-based GFM control

The proposed GFM control method achieves ultrafast black start within switching cycles and ensures instantaneous seamless transitions between the islanded and grid-tied mode. Upon receiving voltage magnitude and frequency references, any inverter using this method can quickly black start and energize the load, forming a stable load voltage. Multiple inverters can then synchronize their output voltages instantly, allowing fast parallel operation without complicated coordination. When synchronizing with the utility grid, the transition from islanded to grid-tied operation is seamless, with no disturbance to voltage or frequency. Importantly, if a fault such as a grid voltage drop occurs during grid-tied operation, the control method's integrated current-limiting strategy enables the GFM inverters to ride through the event without tripping, effectively providing low-voltage ride-through (LVRT) capability without the need for extra hardware or complex control switching. The control maintains both stability and a fast dynamic response, ensuring reliable operation even under challenging conditions.

The control strategy naturally accommodates both islanded and grid-tied modes under a unified framework, removing the need for separate operating modes. Importantly, it does not rely on a phase-locked loop (PLL) for synchronization with the grid, which simplifies the control architecture, enhances dynamic performance, and improves reliability. The method also demonstrates fast dynamic response during transients, allowing the inverters to react rapidly to grid events. Its compatibility with strong grid conditions ensures that the control remains stable even when the grid is stiff.

2. Transformer energization during black start with low inrush current

FSU team developed the transformer energization method with low inrush current during black start process. Unlike transformer energization in GFL mode where the maximum inrush current occurs at the beginning of its start process, leading to potential saturation by pre-fluxing process due to the increased remnant flux, which can be solved using the inverter’s output signal starting with a 180-degree phase shift to cancel the effect of saturation, the transformer flux in the GFM mode, as shown in Fig.7-2, will increase in response to the ramping voltage during the black start process. The pre-fluxing process, in GFM mode, therefore aims to reduce the residual flux rather than increase it as in GFL mode.

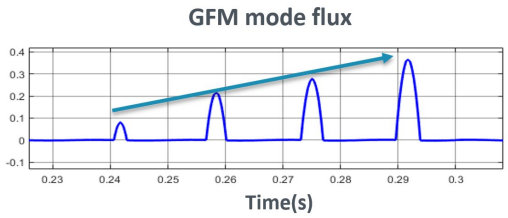


Fig 7-2 Transformer flux increases during black start process

The proposed pre-fluxing method is integrated with our deadbeat-based GFM control which is shown in Fig 7-3. During the black start, the GFM control will achieve the instant transformer energization within several switching cycles. Then, the breaker will be closed to connect the inverter to the load.

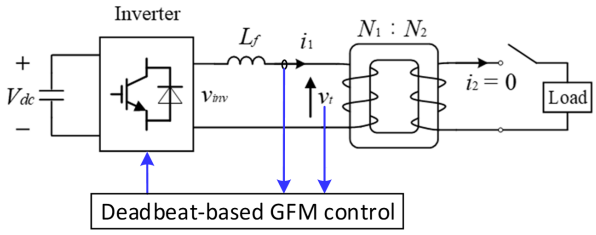


Fig 7-3 Transformer flux increases during black start process

We developed a simulation model to verify the integrated black start and transformer energerization with mitigated inrush current. The simulation results are illustrated in Fig 7-4, which validated that the proposed deadbeat-based GFM control method inherently suppresses the inrush current and the pre-fluxing method can further reduce the inrush current in the transformer during black start process.

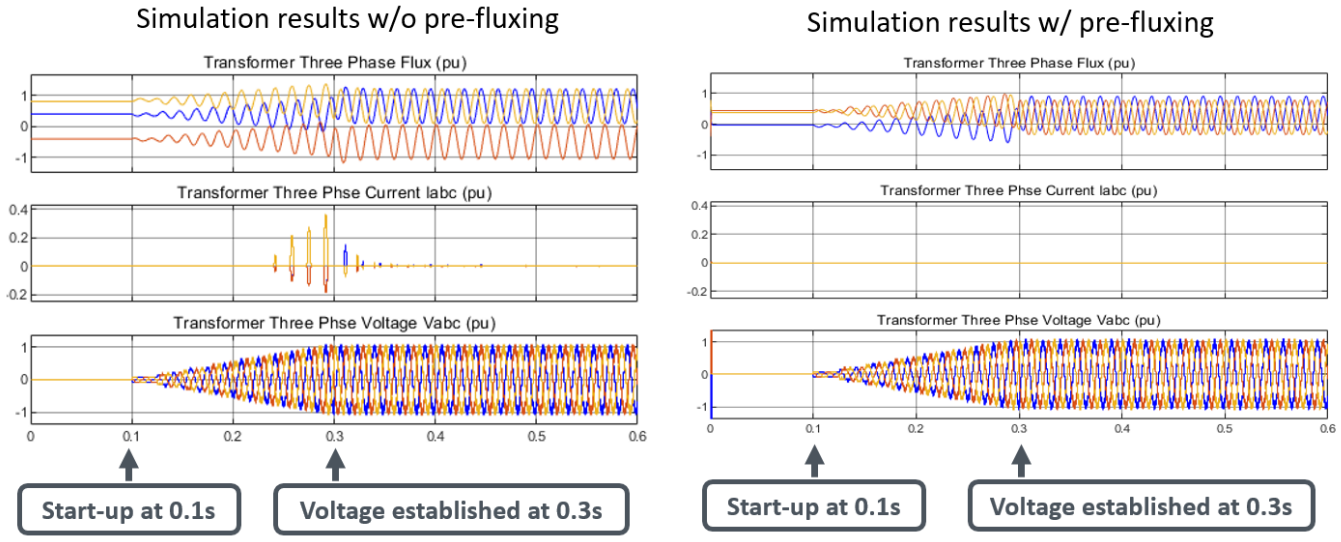


Fig 7-4 simulation results w/o pre-fluxing and simulation results w/ pre-fluxing

**Subtask 7.2: Experimental implementation and validation of switching-cycle-based ultrafast black start**

The deadbeat-based GFM control was implemented on a SiC inverter to access the ultrafast black start performance. The experimental setup was shown in Fig. 7-5. The DC-link voltage is set as 240 V, and the inverter is rated at 5 kW, operating at a high switching frequency of 50 kHz. A filter inductance of 600 μH is chosen to mitigate high-frequency harmonics and ensure smooth current waveforms. To evaluate the ultrafast black start capability of the deabeat approach, the inverter started up with a pre-connected 1.8 kW resistive load. The inverter was controlled by PE-Expert 4 real-time controller.

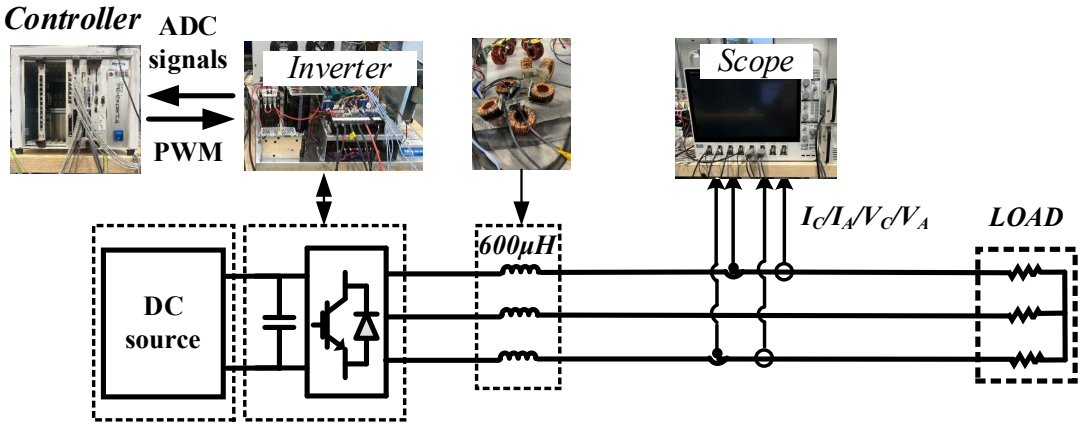


Fig. 7-5 Single deadbeat-based GFM inverter experimental setup.

The experimental results are illustrated in Fig. 7-6. Once the black start begins, the output voltage ramps up to its predefined reference value, while the current simultaneously follows the load demand. As the voltage approaches its target, the system transitions into a steady-state condition where both voltage and current stabilize. The experimental waveforms illustrate that the output voltage reaches its steady-state reference level within approximately 5ms, which is significantly faster than the project benchmark of 0.5 seconds for black start operations. This rapid response demonstrates the fast dynamic performance of the switching-cycle-based control method.

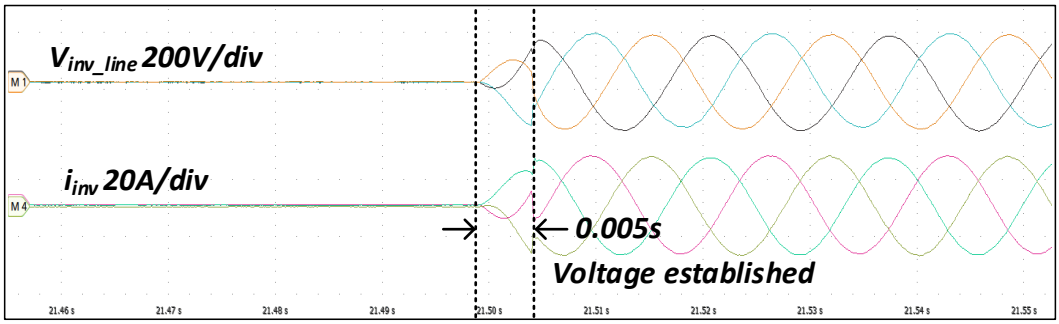


Fig. 7-6 Single deadbeat-based GFM inverter black start experimental results.

The observed experimental results conclusively verify the proposed control scheme's capability to achieve ultrafast and stable black start performance with load. The precise and rapid voltage establishment, combined with controlled current delivery, affirms the

method's suitability for critical power restoration applications where swift recovery is essential.

**Subtask 7.3: Simulation validation of a realistic 100-kW PV-battery hybrid plant for the ultrafast black start.**

In this subtask, the NU team conducted PSIM simulations of a 100 kW PV-battery hybrid power plant to demonstrate ultrafast black start performance using the proposed VOC strategy that will be elaborated in Task 8. The simulation system configuration is illustrated in Fig. 7-7, where one IBR is simulating the battery inverter implemented VOC-based GFM control and handling local load black start and grid-reconnection, while the other IBR is modelling the PV inverter implemented VR-based GFL control and injecting power into the grid. The battery-GFM inverter is 40kW rated and PV-GFL inverter is rated at 60kW, making the total rated power of hybrid plant 100kW. The local load is a passive load and rated at 20kW. Therefore, during the islanded mode, the battery inverter is expected to black start and supply the 20kW local load, and during the grid-tied mode, it injects additional 20kW into the grid. After the battery-GFM inverter operates in grid-tied mode, the PV inverter starts connecting to the grid in grid-following mode and injects its full 60 kW to the grid.

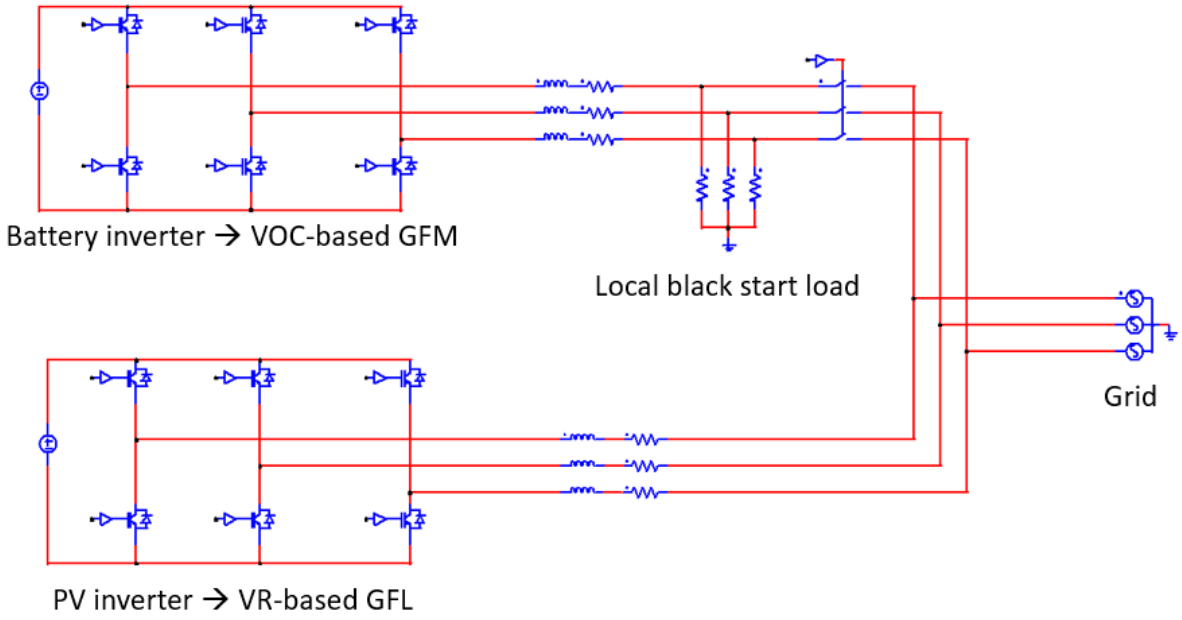


Fig. 7-7: PSIM simulation for 100kW PV-battery hybrid plant black start using VOC-based GFM control and VR-based GFL control.

The key simulation results are demonstrated in Fig. 7-8 and Fig. 7-9. The battery GFM inverter is activated at t = 0 s to supply the local critical load for black start. After successfully energizing the local load and build up PCC voltage, it reconnects to the main grid at t = 0.6 s. Subsequently, the PV GFL inverter initiates its VR_based GFL operation connecting to the grid and begins injecting power into the grid at t = 0.8 s. The entire black start process of the hybrid power plant is completed within 1 second.

In Fig. 7-8, by using the proposed VOC GFM method for battery inverter, we can see ultra-fast black start to support the local critical load within 80ms, which satisfies the requirements and validated the effectiveness of the proposed VOC method. During the grid-reconnection transient, the inverter makes transition from islanded mode to grid-tied mode, the voltage waveform is smooth, and no disturbances are observed. The overall black start finished within 1s, which meet the expected outcomes.

Fig. 7-9 demonstrates the voltage amplitude and power distribution between battery and PV inverters with the grid during the black start process. The battery inverter operating under VOC-based GFM control, effectively establishes the voltage and supplies the local load in islanded mode, and delivers additional power to the grid once grid connection is established, utilizing its full rated capacity. The PV inverter with VR-based GFL control, also achieves ultra-fast startup and injects its full rated power into the grid. The system as a whole demonstrates stable and robust operation, with proper power sharing and no control interference between the parallel inverters. These results validated the effectiveness of the proposed control enables the ultrafast start for PV-battery hybrid plant.

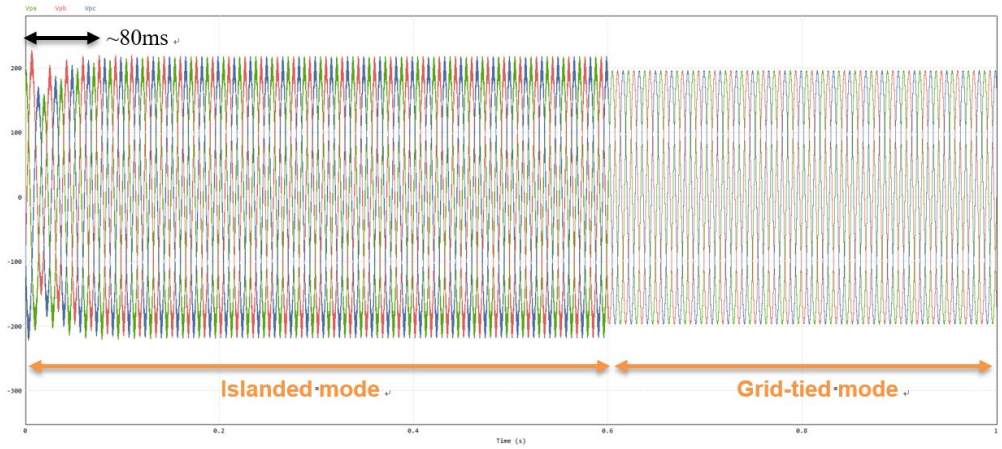


Fig. 7-8: PCC voltage of the local black start critical load during the black start process.

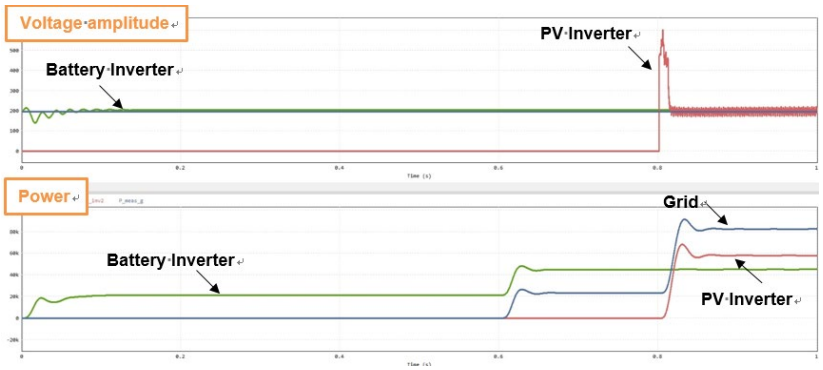


(a) Overall process

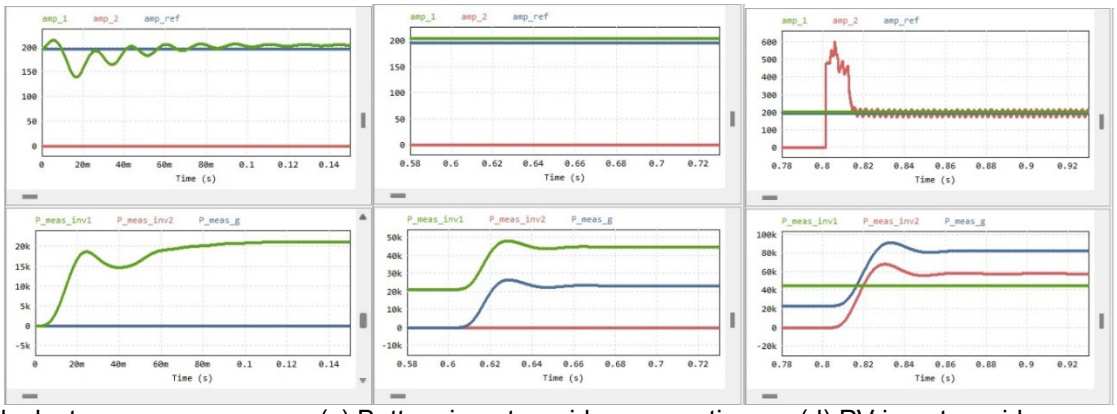

(b) Black star (c) Battery inverter grid-reconnection (d) PV inverter grid-connection

Fig. 7-9: Voltage amplitude of inverters and power distribution of the two inverters and grid during the black start process.

## Task 8 Evaluation of developed controls and ultrafast black start

| | ***Description*** |
|---|---|
| **T8** | **Task Name: Evaluation of developed controls and ultrafast black start**<br>**Task Description:** We will develop the hybrid plant model and integrate the developed inner and outer loop controls and the ultrafast black start with the plant model. Different developed controls and black start algorithms will be evaluated to compare their advantages, explore potential limitations, and identify the most suitable applications for each approach. |
| **M 2.8.1** | PV plus battery model is developed and modified to integrate inner and outer control layers. Developed controls are evaluated on at-scale plant model on a digital platform.<br>**100% Completion:** The deadbeat based UUCC approach and VR+VOC based UUCC approach were evaluated and compared. |
| **Deliverables:** Evaulation results of proposed GFL methods and GFM methods. | |

In BP1, FSU team proposed VR-based inner loop control and designed a GFL method integrating VR-based inner loop. In BP2, FSU team developed a deadbeat-based UUCC for a hybrid PV-battery plant with multiple inverter units. The control algoritm for the *i-th* inverter is illustrated in Fig. 8-1.

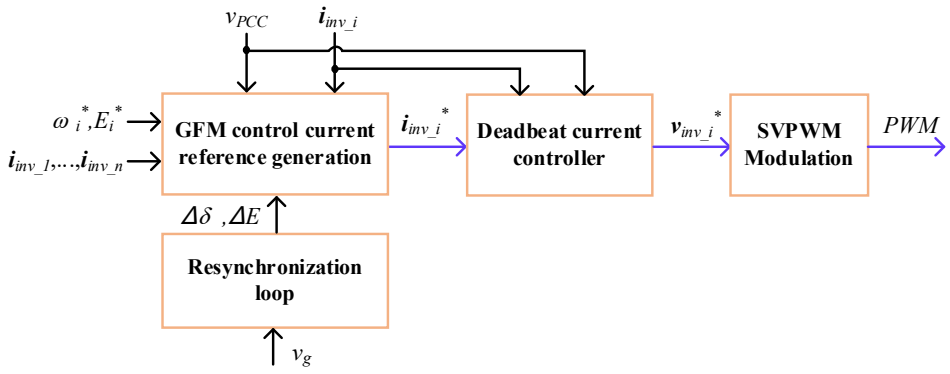


(a)

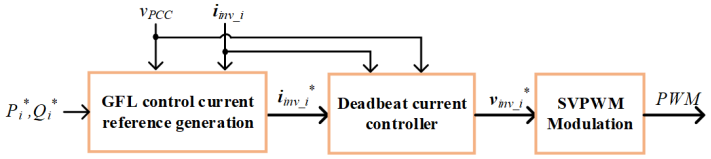


(b)

Fig. 8-1 Proposed deadbeat-based UUCC for hybrid PV+Battery Plant: (a) GFM control for battery .inverter; (b) GFL control for PV inverter

Fig. 8 (a) shows the deadbeat-based GFM control diagram, $\omega_i^*$ and $E_i^*$ represent the frequency reference and voltage reference of *i*-th inverter, respectively. The variable $i_{inv\_i}$ denotes the phase current of *i*-th inverter, while $v_{PCC}$ and $v_g$ correspond to the PCC phase voltage and grid phase voltage, respectively. The proposed GFM control is mainly composed of four key components: resynchronization loop, GFM current reference generator, deadbeat current controller, and SVPWM modulation. The resynchronization loop is responsible for determining the phase angle difference $\Delta\delta$ and voltage amplitude difference $\Delta E$ between the grid voltage and PCC voltage. Then, the generated $\Delta\delta$ and $\Delta E$ will be delivered to the GFM current reference generator, which is used to generate the next cycle current reference. After the current reference is obtained, the deadbeat current controller will calculate the next cycle voltage reference. Finally, the SVPWM modulation block will convert the computed voltage reference into corresponding PWM signals for inverter switching. It is important to note that the GFM control in (a) is an universal method including ultrafast black start, islanding mode and grid-tied mode where the ultrafast black start and islanding mode lab validation has been reported in Task 7.2. As for the GFL control diagram in Fig.8 (b), the $P_i^*$ and $Q_i^*$ represent the active and reactive power references of *i*th inverter, respectively. All other variables remain consistent with those defined in the GFM control diagram. Similar to the deadbeat-based GFM method, the proposed GFL method exhibits universal control for start up, normal state and LVRT transients without requiring mode switching – unlike the VR-based GFL method, which relies on different control mode for startup and grid-tied option to optimize performance. Another advantage of proposed deadbeat approach is its ability to achieve switching-cycle-based control, therefore it can mitigate inrush current within one switching cycle during large-signal transients such as 100% load change and LVRT events. The large-signal stability of proposed deabeat method for multiple inverter units has been analyzed and proved using the Lyapunov method. The proposed deadbeat method are especially beneficial for inverters using WBG devices with high switching frequency.

The universal control of deadbeat-based GFM and GFL were verified through simulation results in Fig. 8-2 and Fig.8-3, respectively using same parameters of two SiC inverters in our test bed. The switching frequency is 50 kHz. The filter inductance of the two inverters are selected as 600μH and 800μH, respectively. And the line to line RMS voltage is 120V/60Hz. Load #1 is 8Ω (1.25kW) resistive load, while load #2 is 4Ω(2.5kW) resistive load, which is consistent with our test setup for final lab validation in Task 10.

Fig. 8-2 shows the two-inverter configuration for GFM operation.In the beginning, both CB1 and CB4 are open. The two GFM inverters start up independently, and establish their own load voltage at 0.2s. Once the voltage is established, the two inverters synchronize at 0.5s, and CB1 is closed to connect them together at 0.6s. After the

inverters are interconnected, the power redistribution function is tested. Initially, the power ratio between the two inverters is 1:2, but at 0.7s, it is adjusted to 1:1, demonstrating dynamic power-sharing capability. Subsequently, the Subsequently, the power ratio is reverted to 1:2 at 0.8s, confirming the system's ability to flexibly redistribute power. At 1.1s, a resynchronization command is issued to synchronize both inverters with the grid. Shortly thereafter, at 1.2s, CB4 is closed, successfully establishing the grid connection.

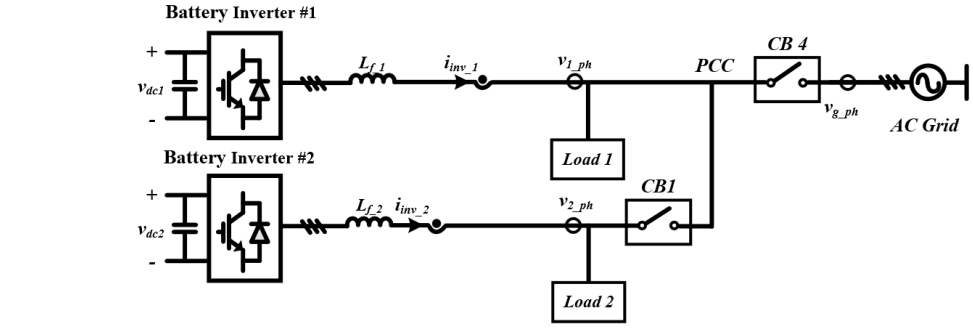


(a)

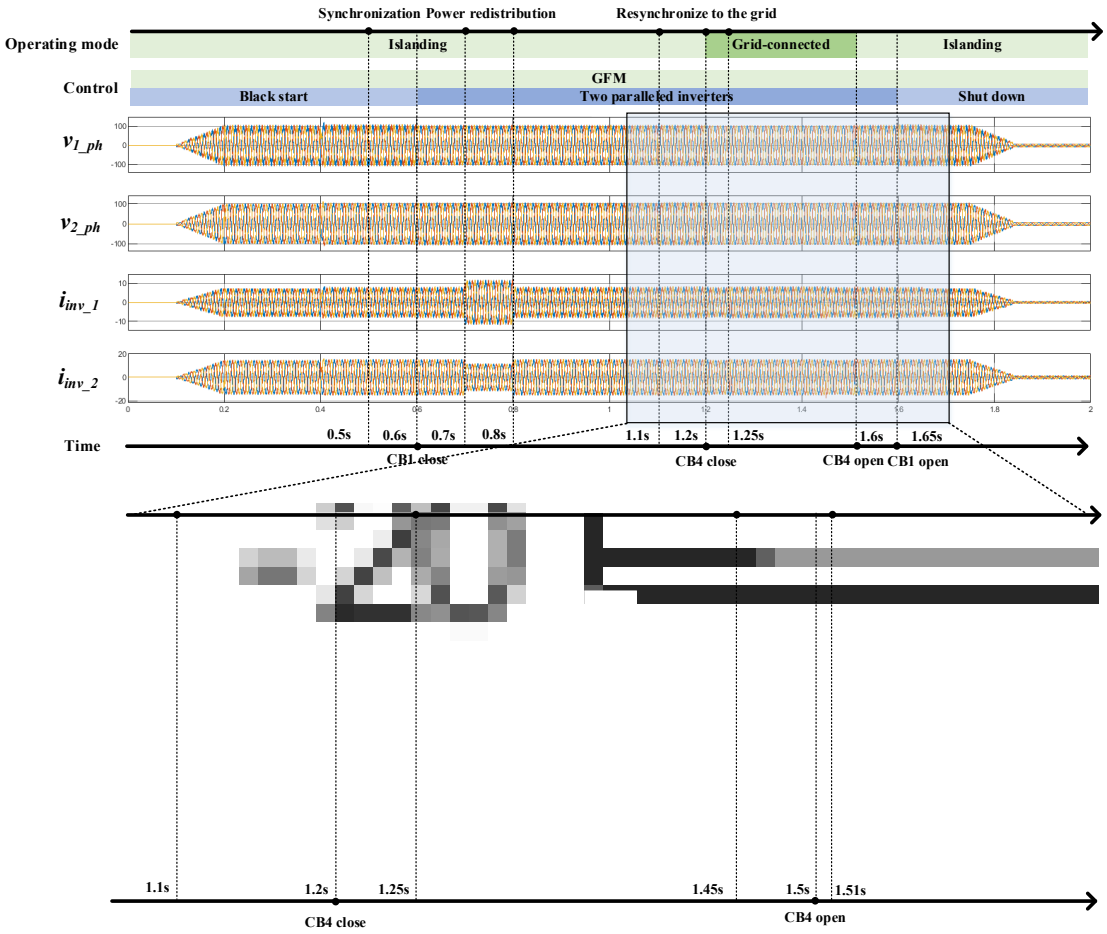


(b)

Figure 8-2 Simulation configuration and simulation results (a) two GFM inverters configuration; (b) simulation results.

After the connection, the resynchronization loop is bypassed at 1.25s. The transition to grid synchronization is completed smoothly, with the synchronization transient finishing within a single switching cycle (20μs). Notably, there is nearly no current and voltage overshoot during the transient. Following the successful synchronization, a disconnection command is issued, and at 1.3s, CB4 is opened to isolate the inverters from the grid before they are powered down. These simulation results demonstrate the effectiveness of the proposed control strategy, showcasing its ability to achieve ultrafast and stable grid synchronization while minimizing transient inrush currents and ensuring seamless power transitions. This validation highlights the robustness of proposed deadbeat based GFM control approach.

Fig. 8 -3 (a) shows the test setup consisting of two GFL inverters, each rated at 5 kW, operating at a switching frequency of 50 kHz. The inverters are connected to the grid through single L filters, with 600 μH inductance for Inverter 1 and 800 μH for Inverter 2. The grid voltage is chosen to be 120 V/60 Hz. Both inverters are controlled to track active and reactive power references of 3 kW and 0 Var, respectively.
In this simulation, the inverters startup independently. At 0.02 s, CB2 is closed to connect Inverter 1 to the grid. The simulation reveals that the inverter establishes grid connection smoothly, with negligible inrush current during the transient. Subsequently, at 0.04 s, CB1 is closed, connecting Inverter 2 to the grid. Similar to Inverter 1, the connection is completed without any observable inrush or transient disturbance. Both inverters commence power injection at 0.07 s, steping up their outputs to meet the assigned 3 kW active power target.

At 0.1 s, the LVRT event is triggered as the grid voltage drops to 0.5 pu. Despite the voltage depression, both inverters remain connected with the grid and continue operating stably, delivering power with no interruption or fault-triggered shutdown. The proposed GFL control successfully regulate the current to prevent overcurrent faults, reflecting the robustness of the deadbeat-based method. The grid voltage recovers to its nominal level at 0.2 s, and both inverters seamlessly resume full-power operation without requiring a reset or manual intervention. Notably, no inrush current is observed during the recovery process, confirming the smooth dynamic response and control stability of the system. These results confirm the GFL control strategy's resilience and its ability to maintain smooth grid interaction, even under voltage disturbances such as LVRT.

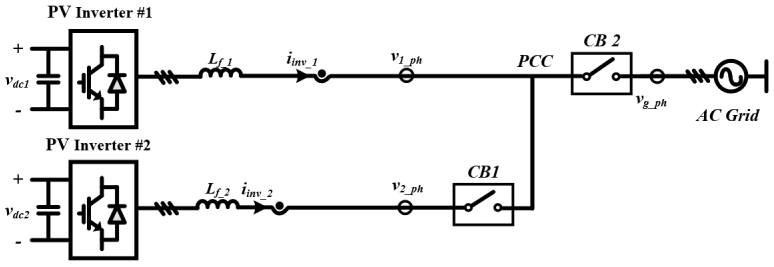


(a)

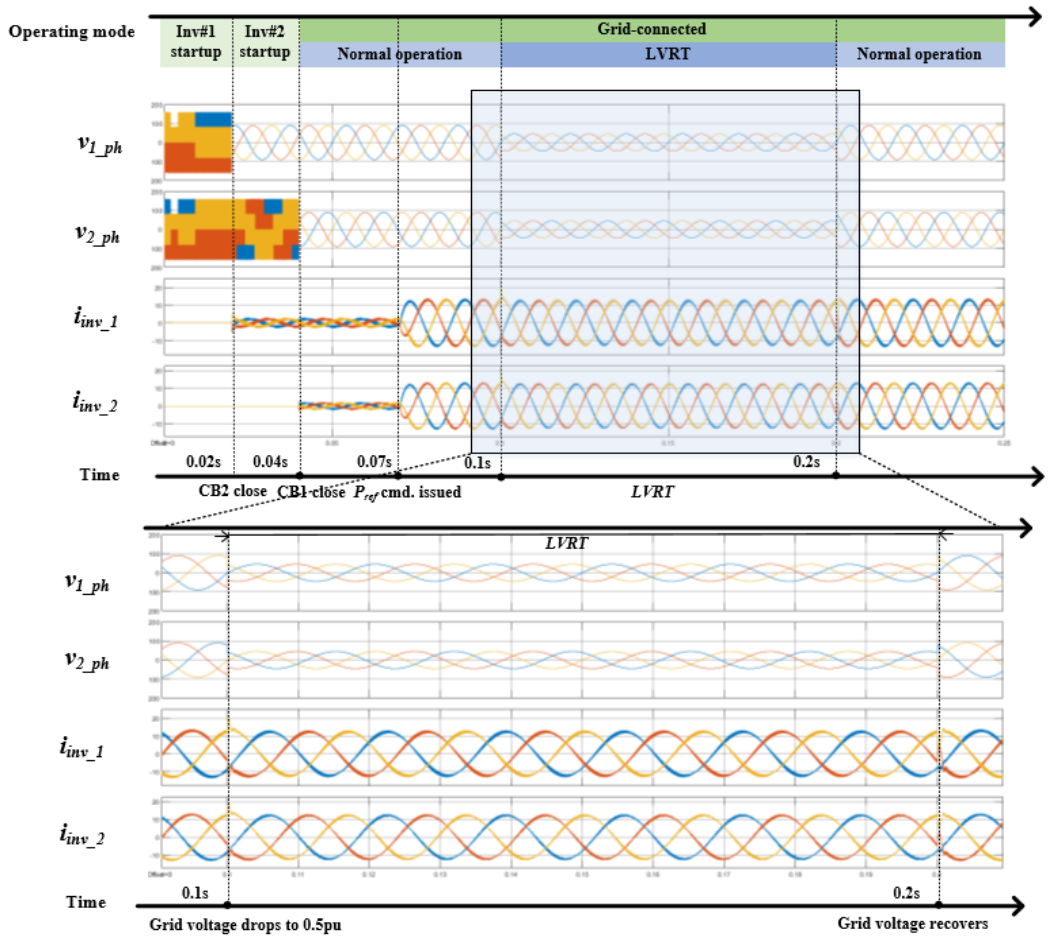


(b)

Fig 8-3 Simulation configuration and simulation results (a) two GFL inverters configuration; (b) simulation results.

In addition to deadbeat approach developed by FSU team, Northeastern University (NU) team developed a VOR-based GFM method in BP2 enabling an ultrafast black start. We analyzed a subsystem of the complete black start system, consisting of parallel Virtual-Oscillator-Controlled (VOC) inverter-based-resources (IBRs) connected to a common bus, supplying a local passive RL load, as illustrated in Fig. 8-4. In practical black start scenarios to this subsystem, parallel inverters may be activated and connected to the grid sequentially through point-of-common-coupling (PCC). It's noteworthy that the inverters might be remotely placed, which introduces significant line impedances, even when on the same distribution line. Additionally, black starting a generator will likely require multiple geographically dispersed PV + Battery hybrid installations to collectively achieve the necessary power. Without proper control redesign, this could result in high shoot-through current and slow transient synchronization. Future work should focus on developing specific approaches to ensure the promised black start times can be met in such scenarios.

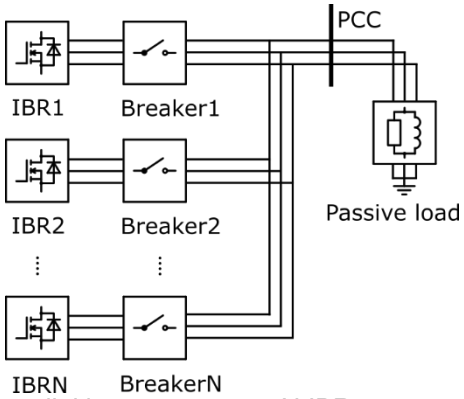


Fig 8-4: The block diagram of parallel inverter system: N IBRs are parallelly connected to support the passive load.

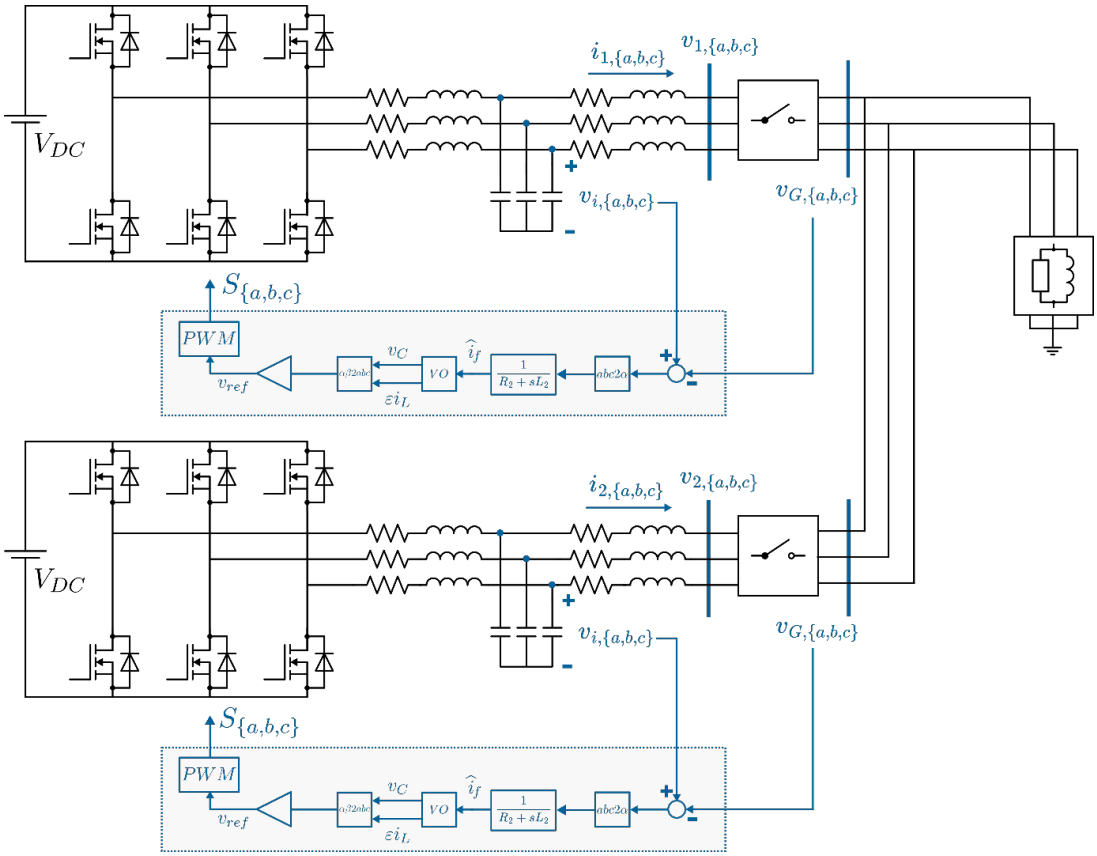


Fig. 8-5: The proposed 2-parallel-inverter system block diagram of the three-phase VOC inverter using predictive feedback for the VOC.

During black start process of the subsystem, the conventional approach to VOC presents potential issues, including inrush current, PCC voltage drop, and prolonged synchronization time. To address these challenges, an advanced control method is proposed using an estimator, as demonstrated in Fig. 8-5. This control scheme uses the predicted current for the input of the virtual oscillator (VO), enabling the inverter to synchronize with the PCC even when the breaker is open, and maintaining equivalent operation to conventional VOC during steady-state conditions. This significantly reduces inrush current and PCC voltage drop, while also accelerating the synchronization speed.

To validate the proposed control scheme, a test scenario involving two IBRs was conducted in Simulink simulation. The black start sequence of the test subsystem is as follows, and the results are shown in Fig. 8-6.

1. **Stage 0:** At 0s, turn on IBR1 and close Breaker 1. IBR2 remains inactivated and Breaker 2 is open.
2. **Stage 1:** At 0.233s, turn on IBR2, and keep Breaker 2 open. IBR1 and Breaker 1 are unchanged.
3. **Stage 2:** At 0.5s, close Breaker 2. Both IBR1 and IBR2 are connected to the load through PCC.

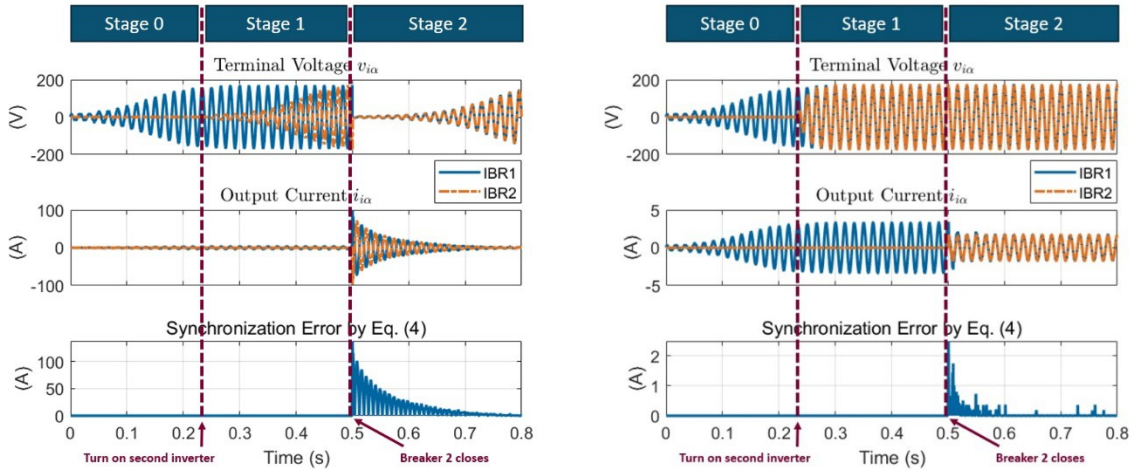


Fig. 8-6: The simulation results for the subsystem black start using (a) traditional VOC method and (b) proposed VOC method. The $\alpha$ components of the three-phase quantities are used to plot the waveform. The synchronization error is calculated by taking the absolute value of the instantaneous current difference between the two inverters and multiplying it by a constant.

During Stage 1, Fig. 8-6(a) shows an arbitrary mismatch before the breaker closes using the conventional VOC method. In contrast, Fig. 8-6(b) demonstrates that the proposed method enables IBR2 to quickly build up the terminal voltage and synchronizes with IBR1 terminal voltage (which also serves as the PCC voltage during Stage 1), while Breaker 2 remains open and the current output of IBR2 is zero. Therefore, upon transitioning to Stage 2, the proposed approach ensures fast smooth current synchronization and minimizes voltage drop at the PCC, while maintaining consistency with conventional VOC during steady-state operation.

The proposed VOC-based GFM method also equips the universal control across black start, islanding and grid-tied mode. The unified virtual oscillator control (VOC)-based inverter control strategy is shown in Fig. 8-7, capable of steady operation in both islanded and grid-connected modes, and fast and seamless transition between them, which satisfies the ultrafast black start time requirements.

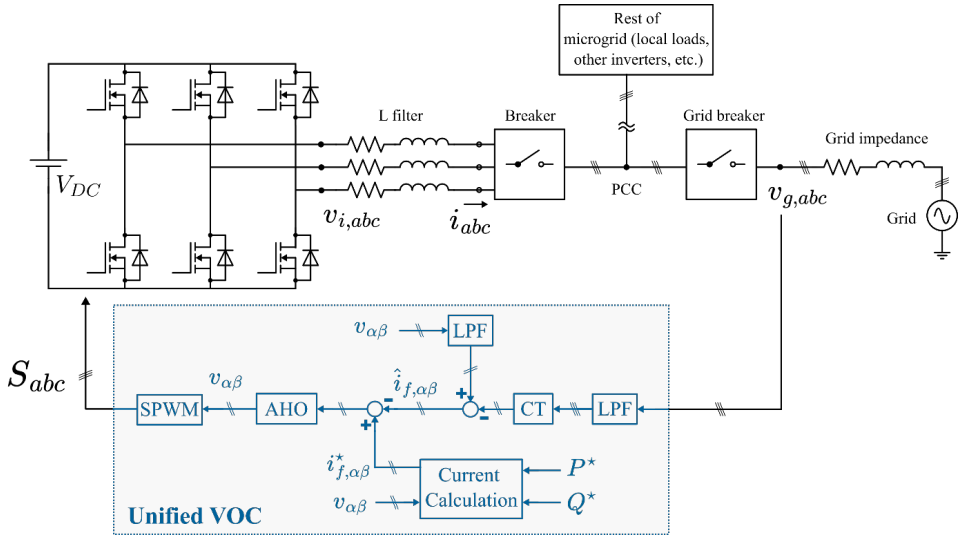


Fig. 8-7: The block diagram of proposed unified VOC.

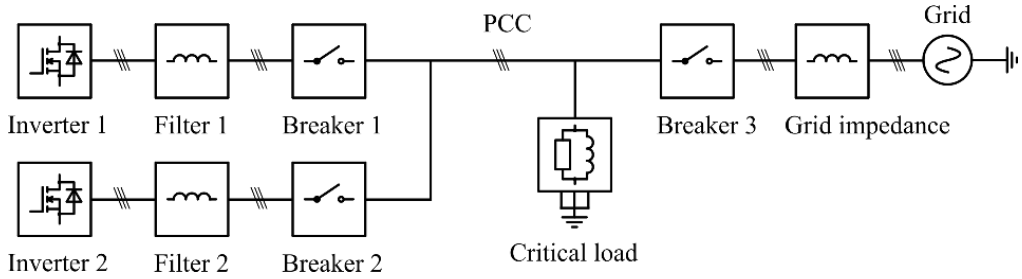


Fig. 8-8: The block diagram of the baseline black start test system.

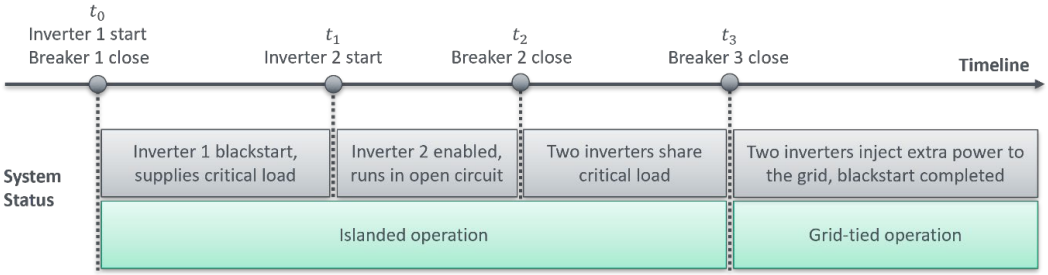


Fig. 8-9: The baseline timeline of the black start sequence.

The testing system for the ultrafast black start using the unified VOC is illustrated in Fig. 8-8, and the black start timeline is demonstrated in Fig. 8-9. At t = $t_0$, Breaker 1 closes and Inverter 1 performs its black start to energize the local linear passive loads. Then at t=$t_1$, Inverter 2 is enabled, and the inverter is pre-synchronized so that its voltages are in-phase with Inverter 1, even before the Inverter 2 provides currents to the load. Then at t=$t_3$, Breaker 2 closes. Inverter 2 shares critical loads with Inverter 1, but there is still no grid connection. Finally at t=$t_3$, the Breaker 3 is closed, and the two inverters inject any extra power not sent to the critical loads to the grid, through its grid impedance. When both inverters eventually reconnect to the main grid and inject power into the grid. This procedure will be followed, also, when experimentally evaluating the black start capability of the prototype inverters, no matter which control algorithm is used in an inverter being evaluated.

The key functionalities of the unified VOC during the ultrafast black start process can be summarized in three aspects:

1. Fast black start local critical loads by one inverter

As soon as the inverter is activated, the fast dynamic response of the VOC ensures a rapid black start. Furthermore, with the proposed unified VOC, the inverter synchronizes with the grid voltage even during islanded operation.

2. Fast parallel inverter synchronization and power sharing

The second inverter also synchronizes with the grid, similar to the first inverter, ensuring that when the breaker is closed to connect the inverter to the Point of Common Coupling (PCC), the transients remain smooth and fast. Additionally, the proposed VOC maintains load sharing and droop properties similar to the traditional VOC, which guarantees correct load distribution during parallel inverter islanded operation.

3. Fast grid reconnection and power redistribution

Since both inverters are synchronized with the grid, no inrush current occurs during grid reconnection, allowing for an instant and smooth grid reconnection. Additionally, the proposed VOC retains the traditional characteristics of grid-tied VOC operation, ensuring correct power delivery from the grid-tied inverter.

The PSIM simulation results are shown in Fig. 8-10. The waveforms demonstrate the successful implementation of the VOC in C code. Additionally, the proposed algorithm achieves an ultrafast black start within 1 second, with smooth transients, stable steady-state operation, and correct power distribution.

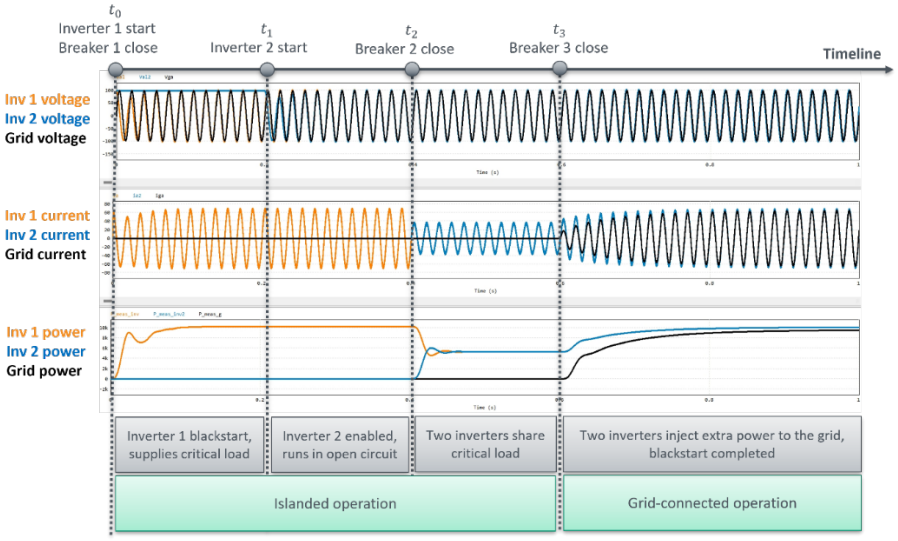


Fig. 8-10: The PSIM simulation results of black start system. For voltages and currents, only phase A is presented for overview.

Notice that between $t_0 < t < t_2$, the Inverter 2 does not produce current since it is in open circuit. Yet at $t=t_1$, the pre-synchronization phase of Inverter 2 can be seen. Its voltage quickly synchronizes to the same phase as Inverter 1. Then when Breaker 2 closes and Inverter 2 produces power to the critical load, there is no noticeable shoot through current and the two inverters can share equal power within a few line cycles. Similarly, when Breaker 3 closes, there is no shoot through currents in the inverter and the inverters quickly share power together. Notice that the entire process of all the different stages

finishes in less than 1 second. These simulation results demonstrate a successful preliminary test of the unified VOC for ultrafast black start. The next step will be to implement (program) the algorithms on real microcontrollers for inverters and test realistic black start experimental systems.

Additionally, the baseline system is expanded by including an induction motor load to evaluate the black start performance using the unified VOC control for inverters. The induction motor is one of the more difficult loads to black start, since its high inductance can cause shoot through currents through the switches in the inverter if the controller is not properly operated. The updated simulated system with the induction motor is illustrated in Fig. 8-11, where the induction motor is connected to the PCC through Breaker 3. The system is tested in the SIMULINK environment, and the simulation results are shown in Fig. 8-12. The results demonstrate that with the proposed VOC control, the induction motor starts smoothly, causing minimal disturbance on both the PCC voltage and inverter current.

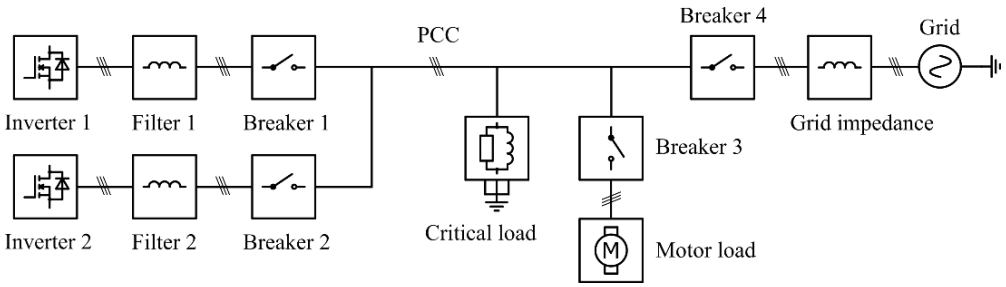


Fig. 8-11: The block diagram of the black start test system with motor load.

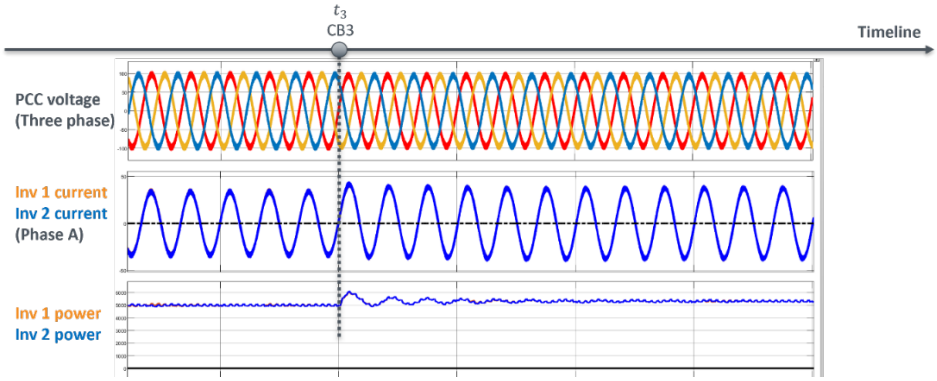


Fig. 8-12: The SIMULINK simulation results of motor load black start. For currents, only phase A is presented for overview.

The results demonstrate that with the proposed VOC control, the induction motor starts smoothly, causing minimal disturbance on both the PCC voltage and inverter current. We only show the simulation in Fig. 8-10 around t = $t_3$, since that is when the induction motor is connected to the inverters. Notice that the inverter currents remain well bounded, without the shoot through currents, due to the saturation current limiters implemented in the VOC controllers. As one might expect, though, the connection of the motor does lead to a 20% increase in peak currents, but this is easily within the safe operating regions of the inverters switches and components. It takes about 8 of the 60 Hz line cycles (< 150 ms) for the transients to settle down to its steady state values, as indicated by the power plots of the two inverters.

The main features of the developed VR-based GFL method, VOC-based GFM method, deadbeat-based GFL and GFM method are summarized and compared in Table 8-1. The UUCC method developed by Siemens is a traditional droop-based GFM approach without ultrafast black start capability. Therefore, it served as a baseline for the laboratory evaluation of the developed control methods in Task 10.

Table 8-1 Evaluation of developed controls and ultrafast black start

| GFL Control | | Virtual Resistance method | Deadbeat method |
|---|---|---|---|
| **Synchronization** | | No PLL; current-based; synchronized within1 line cycle | No PLL; current-based; synchronized within 2 switching cycles |
| **Stability** | | Stable under weak grid due to virtual resistance in inner-loop | Stable under weak grid via adaptive output impedance |
| **Steady-state** | | Low steady-state error | Low steady-state error |
| **Startup** | | Separate startup control enables inrush-free synchronization | Unified control; inrush-free synchronization |
| **Fault Ride-Through** | | Not Applicable | Built-in LVRT with switching-cycle transients; inrush-free |
| **Multi-Unit Operation** | | Not evaluated | Veified;stable with switching-cycle transient settling |
| **Transfomer Energization** | | Low inrush cuttent during energization | |
| **GFM Control** | | **VOC method** | **Deadbeat method** |
| **Black Start** | | Voltage and frequency established during black start | Ultrafast voltage/frequency establishment during black start |
| **Islanding Operation** | | Low stead-state error; Autonoumous power sharing | Low steady-state error; Instantenous power sharing |
| **Grid-tied Operation** | **Grid Synchrtonization** | Grid pre-synchronized during black start | Instantenous synchronization within switching cycles |
| | **Stability** | Stable under stiff grid | Stable under stiff grid |
| **Fault Ride-Through** | | Fast transients; low inrush current | Faster trantriants within switching cycles; inrush-free |
| **Multi-Unit Operation** | | Verified | Verified |
| **Transfomer Eenergization** | | NA | Low inrush current via pre-fluxing method |

Notes:
- GFL = Grid-Following; GFM = Grid-Forming
- LVRT = Low Voltage Ride-Through
- VOC = Virtual Oscillator Control

## Task 9 Control integration for lab validation

| | Description |
|---|---|
| **T9** | **Task Name: Control integration for lab validation**<br>**Task Description:** We will integrate black start, outer loop and inner loop control in the lab for experimental validation. Communication protocol between each two layers will be specified to send and receive commands. We will share in the group with block diagrams, design specifications, flow chart, and communication protocols. |
| **M 2.9.1** | Lab validation of integrated outer-loop and inner-loop controller.<br>**100% Completion:** The deadbeat-based GFM control, VOC control, and droop-based control are integrated and ready for experiments. |
| **Deliverables:** All the GFM control algorithms are integrated for lab verification. | |

In this task, the FSU team successfully integrated their developed deadbeat-based Grid-Forming (GFM) control algorithm with both ultrafast black start, islanding and grid-connected functionalities. The experimental setup is illustrated in Fig. 9-1. The DC-link voltage is set to 240 V, and the inverter is rated at 5 kW. A filter inductance of 600 μH is selected, and the resistive load is configured as 8 Ω (1.8 kW). The line-to-line RMS voltage is set to 120 V at 60 Hz. Control is executed using the PE-Expert 4 real-time controller.

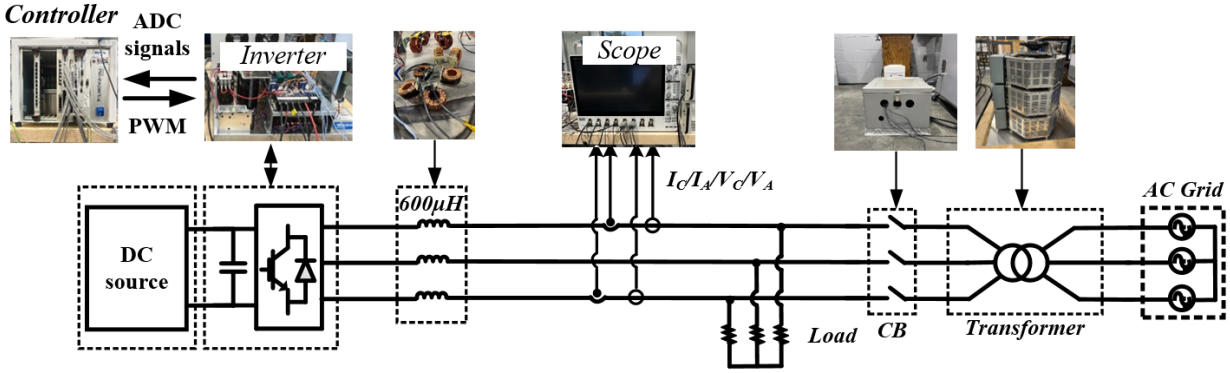


Fig.9-1 Experimental testbed of a single inverter using deadbeat-based GFM control.

In this experiment, the inverter performs a black start under loaded conditions. After voltage establishment, a grid-synchronization command is issued, and the circuit breaker is subsequently closed to connect the inverter to the grid. The experimental results, presented below, show that the load voltage is established within 5 ms, which is consistent with prior simulation results. The synchronization process is completed almost instantaneously, with negligible voltage and current overshoot. Additionally, the grid connection occurs smoothly, demonstrating the robustness and effectiveness of the proposed control scheme in practical implementation.

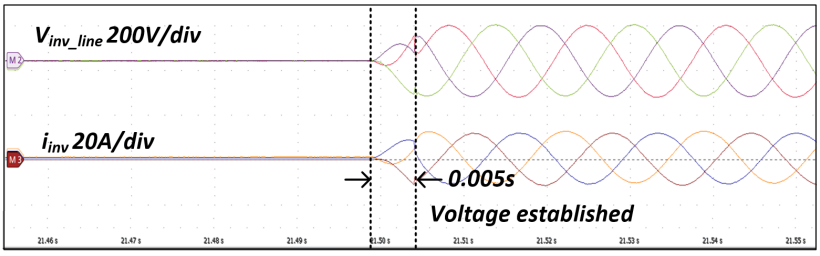


(a)

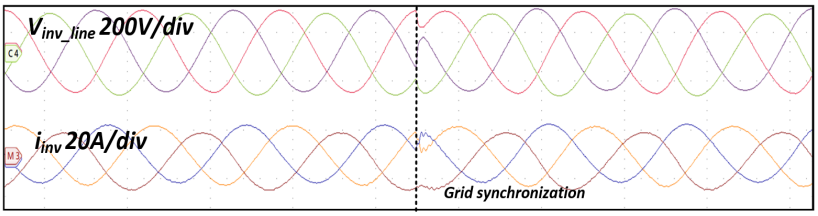


(b)

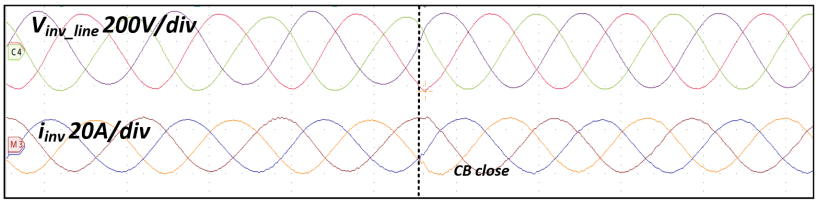


(c)

Fig. 9-2 experimental results: (a) black start; (b) grid synchronization; (c) grid connected.

In this task, Siemens team integrated their developed droop-based GFM control scheme, shown in Fig.9-3 with their black start function.

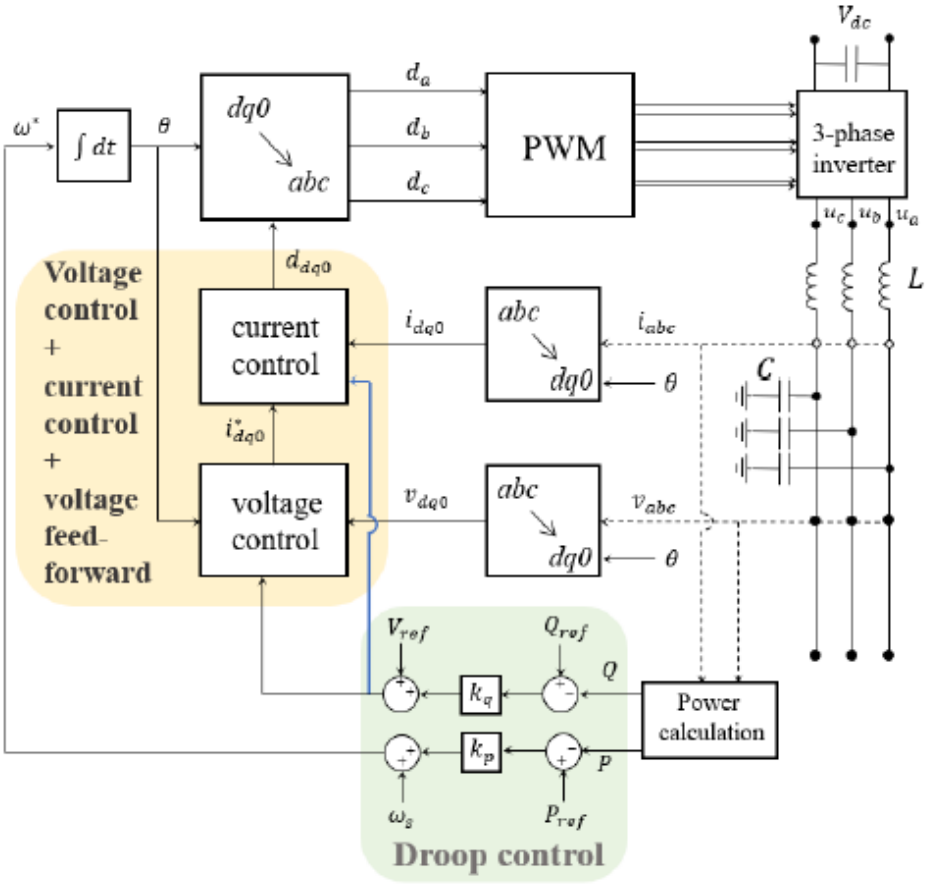


Fig. 9-3 Inverter control incorporating droop for active and reactive power sharing and a cascaded voltage and current controller.

The control flow chart to integrate the black start and GFM is illustrated in Fig. 6-2 and Fig. 9-4.

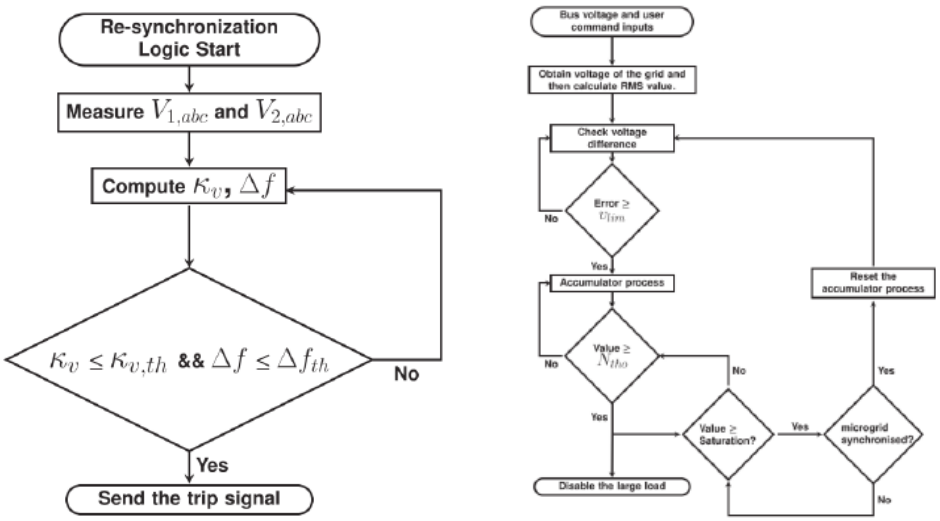


(a) (b)

Fig. 9-4 Control flow chart. (a) synchronization logic; (b) overload detection logic.

The communication architecture for two inverters emulating a hybrid PV+battery plant was developed by Siemens which is shown in Fig. 9-5. To trigger the two inverters on for black start, there are two Beagle Bone Black (BBB) devices which communicate this signal to each inverter via the SPI protocol. The synchronization phase is coordinated by a third BBB, which communicates 1) via the Modbus protocol over TCP / IP with a SIAPP running on a CP-8050 device, and 2) via GPIO with a relay connecting the two inverters. This BBB first indicates its intent to close the open relay to the SIAPP, which then responds with an instruction to execute the “close relay” action. The BBB then commands the relay to close in order to reconnect the two inverters and resynchronize.

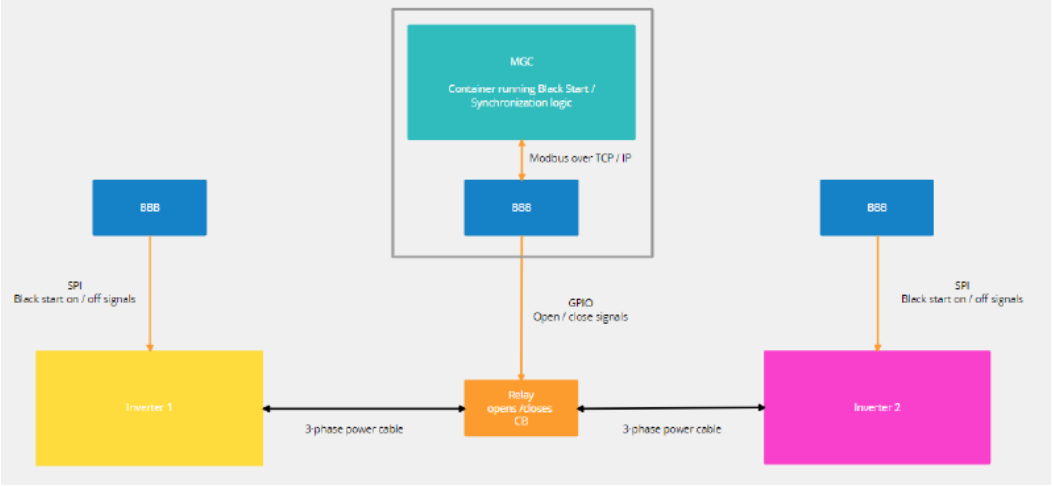


Fig. 9-5 Communication architecture for two inverters emulating a hybrid PV+battery plant with integrated black start and GFM function.

The communication configurationbe tween various layers were designed and listed in Table 9-1.

Table 9-1 Communication configuration between different control layers

| Devices | | Communication Details |
|---|---|---|
| MGC-BBB | Purpose | MGC Receives ready status (Boolean) from BBB. MGC generates and transfers on/off (Boolean) command to the BBB |
| | Direction | Bidirectional |
| | Bit rate | Depends on network interface, we have 100Mbps connection, which is theoretical maximum |
| | Byte size | <= 125 registers (i.e., 250 bytes of data) |
| | Type of communications | Modbus TCP/IP |
| BBB -- Relay | Purpose | Relay control (close/open) |
| | Direction | Unidirectional (BBB to Relay) |
| | Bit rate | Typically, 100 to several thousand toggles per second using python Adafruit_BBIO library |
| | Byte size | 1 |
| | Type of communications | GPIO pin. Devices are connected using jumper cables |
| BBB – Inverters (TAPAS) | Purpose | BBB sends black start (on/off) command and P_ref to inverter and receives inverters measurement data (P, f, V) |
| | Direction | Bidirectional |
| | Bit rate | 100 MHz (**Note:** fastest rate Siemens was able to get is 4ms in their past projects) |
| | Byte size | 8 bytes |
| | Type of communications | SPI pins. Devices are connected using jumper cables. |

## Task 10 Lab HPP validation and evaluations.

| | ***Description*** |
|---|---|
| **T10** | **Task Name: Lab HPP validation and evaluations**<br>**Task Description:** In this task, individual system controllers developed by FSU/NU and Siemens will perform scalable performance testing the developed controls of near real time resilience. |
| **T10.1** | Implement and validate the Siemens system controller in lab using Siemens Microgrid Controller (MGC).<br>**Completion in Q6-FY24**: Siemens team successfully implemented their control method and finished the lab validation using Siemens Microgrid Controller (MGC). |
| **T10.2** | Lab validation of system controller developed by FSU/NU<br>**Completion in Q8-FY25**: Both FSU and NU team verified their developed control methods through experiments. |
| **M 2.10.1** | Individual system controllers developed are integrated with the controllable grid interface.<br>**100% Completion:** Both integrated control methods developed by FSU and NU are validated in the lab. |
| **Deliverables:** The lab validation is finished for all control methods. | |

**Subtask 10.1: Implement and validate the Siemens system controller in lab using Siemens Microgrid Controller (MGC)**

In this subtask, Siemens developed a downscaled microgrid testbed, shown in Fig. 10-1, to demonstrate their integrated control including black start and GFM control.

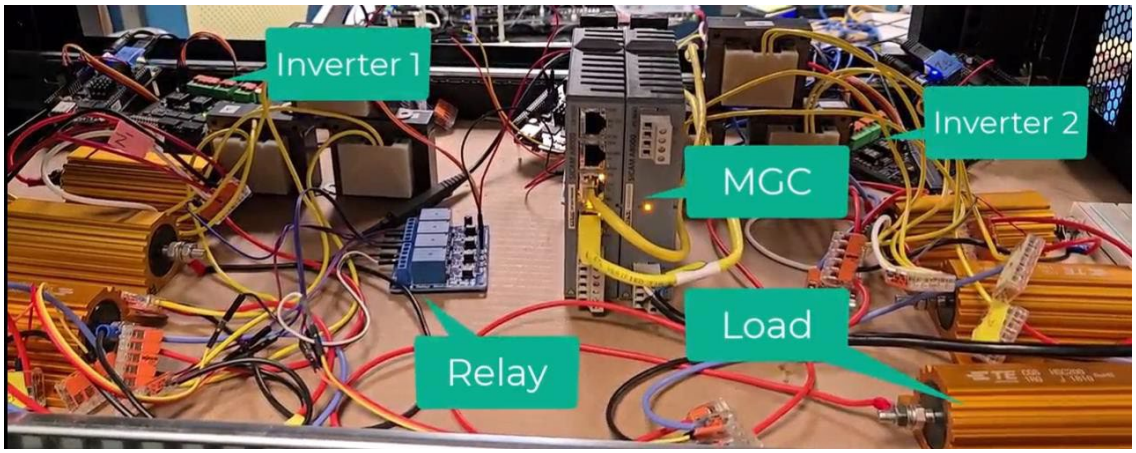


Fig. 10-1 Microgrid testbed developed by Siemens at Siemens lab to demonstrate integrated black start and droop-based GFM control.

The testbed comprises two inverters to emulate a hybrid PV+ battery plant, a four-channel relay, an MGC, and loads for each inverter. The inverters are implemented using TAPAS boards, each connected to a corresponding Beagle Bone Black (BBB) board. The TAPAS boards, developed by Siemens, is a software defined inverter. TAPAS features 3-phase GaN inverter power stage with onboard LC filter and TI digital processor. In this test bed, droop-based grid forming inverter (GFM) control with voltage loop is implemented, as detailed in Fig.9-10. The BBB boards are responsible for communicating on/off commands via SPI pins to start or stop the associated inverters. The output of the inverters is connected to a three-phase resistive load through corresponding three-phase transformers. Each inverter's three-phase bus is connected to the four-channel relay (utilizing only three channels, one for each phase). This setup allows the inverters to operate independently with their own loads or to create a single bus, sharing power and running at a common frequency, depending on the relay's open or closed status. The logic that controls closing of relay is detailed in Fig. 9-11 (b). Additionally, a dedicated Beagle Bone Black is used to communicate the MGC's open/closed commands to the relay via GPIO pins, while communication between the MGC and BBB is established using the TCP/IP Modbus protocol. This testbed is used to demonstrate black start and synchronization between the two inverters. In order to observe live data, an oscilloscope is also connected with one phase from each bus.

The test results are shown in Fig. 10-2 and Fig. 10-3. Initially, when none of the inverters are ON, there is no AC voltage waveform in either bus, corresponding to zero active power, frequency, and Vd component at $t < 0$ seconds in Fig. 10-2. At t=0, Inverter-1 receives an ON (or start) command from its corresponding BBB board. Consequently, the active power of inverter-1 increasing from 0 to 40 W at t = 0 seconds. This represents the black start of Inverter-1 of the testbed.

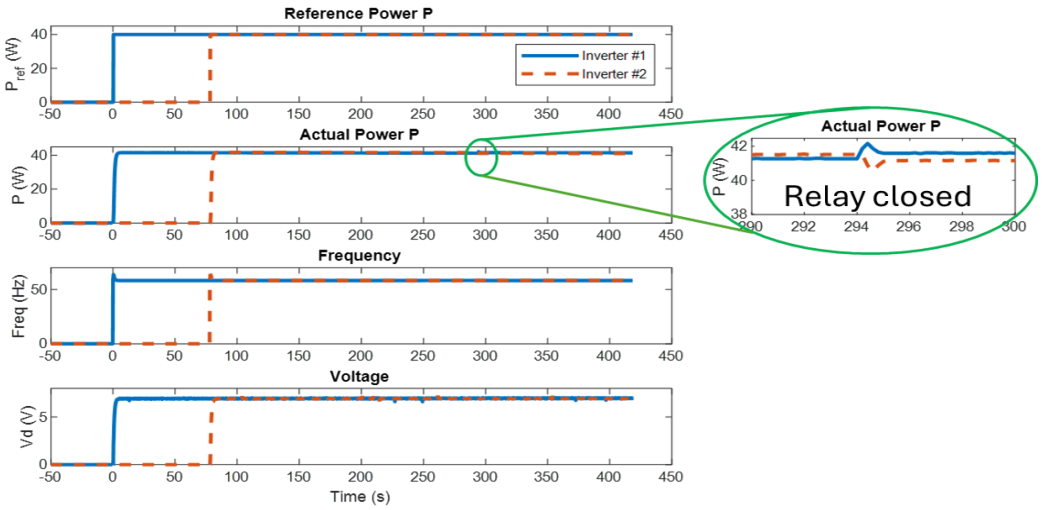


Fig. 10-2. Calculated active power, Frequency and d-component of AC voltage for both inverters

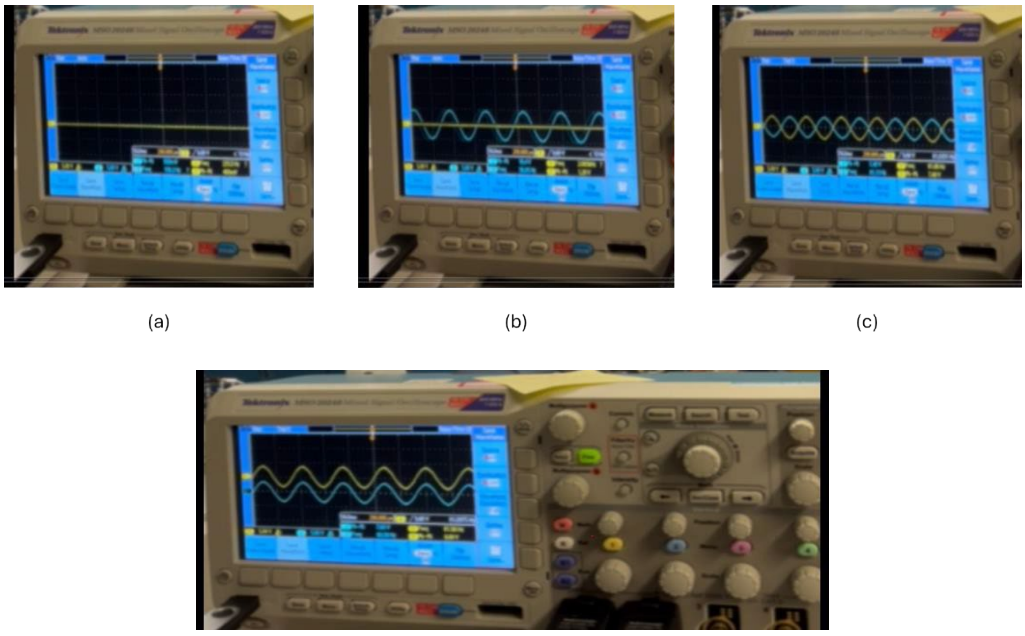

(a) (b) (c)

(d)

Fig. 10-3. Oscilloscope screen demonstrating black start in (a) – (c) and synchronized waveforms from 2 inverters due to closed relay status entering GFM mode in (d).

After some time, around t=80 seconds, Inverter-2 receives a black start command from its corresponding BBB board, as evidenced by the active power of Inverter-2 increasing from 0 to 40 W (see the orange line in Fig. 10-2). Note that the relay connecting the two buses is currently open, and both inverters are running independently with their corresponding loads, which displays different phase angles (asynchronous) between the two waveforms from each bus. At t = 294, the MGC receives ready status information from the BBB board associated with the relay. At this point, the MGC passes this information to the docker container running on the MGC. Based on the synchronization logic, the MGC then issues a command to close the relay around t=295 seconds, which is communicated to the associated BBB board via Modbus, and the BBB transfers this command to the relay via GPIO. As a result, the relay closes, creating a common bus for

both inverters. This is evident from Fig. 10-3 (d), which demonstrates both waveforms having the same phase angles (i.e., synchronous operation). Additionally, the impact of closing the relay is visible in the actual power, with a minor transient around 295 seconds, as highlighted in the zoomed-in plot in Fig. 10-2. Notably, the active power of both inverters remains nearly identical after the relay closes, due to their identical loads. However, if the inverters operate under different loads, closing the relay results in power sharing between the two, stabilizing at an intermediate value. For instance, if inverter-1 operates at 40W and inverter-2 at 60W before the relay closes, both would operate at 50W afterward.

**Subtask** 10.2: **Lab validation of system controller developed by FSU and NU.**

10.2.1 Lab validation of deadbeat-based approach by FSU Team

In this subtask, FSU team has developed a testbed in the lab, shown in Figure 10-4, to experimentally validate our proposed deadbeat-based based grid-forming (GFM) control strategy for HPP that integrates the ultrafast black start function with GFM control in islanded and grid-tied mode.

In this lab testbed, two DC sources are connected to two inverters, respectively, to form a scaled-down hybrid-power-plant (HPP) system. Each inverter is rated at 5 kW and operates at 50 kHz switching frequency. To demonstrate the proposed control's effectiveness in mitigating circulating currents among paralleled grid-tied inverters, two different harmonic filters are intentionally used: a 600μH filter inductance for inverter 1 and an 800μH inductance for inverter 2. Inverter 1 supplies power to 1.8 kW load, while inverter 2 supplies a 3.2 kW load. The PE-Expert 4 serves as the controller for the two inverters to synchronize the carrier waveforms of both inverters, preventing high-frequency circulating currents.

The test timeline and the corresponding experimental results of this HPP system is shown in Figure 10-5.

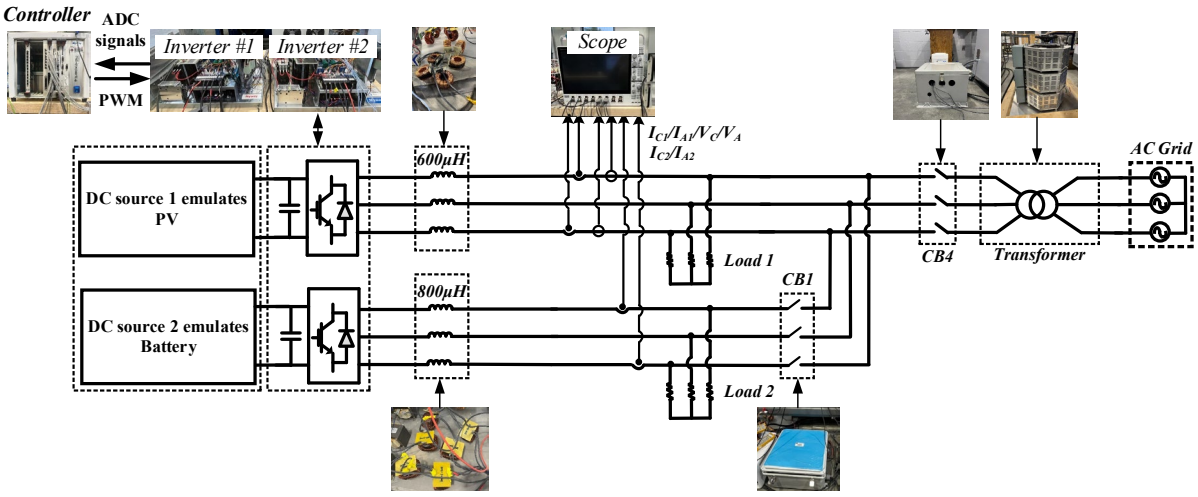


Fig. 10-4: The developed lab testbed for HPP applying proposed deadbeat based GFM control.

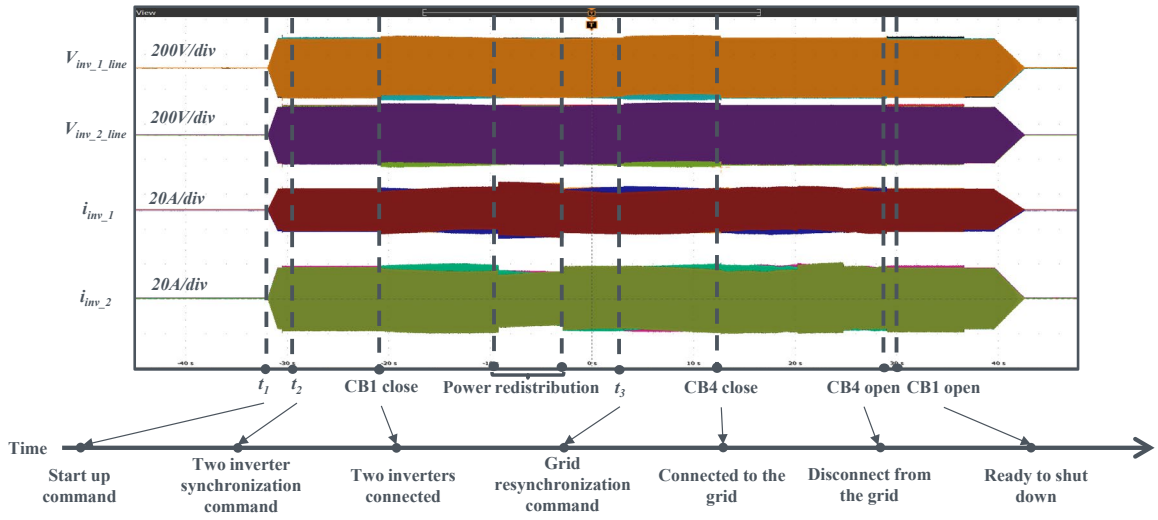


Fig. 10-5: The test timeline and the corresponding experimental results.

At time $t_1$, both inverters start up independently with different loads and establish their respective load voltages. At time $t_2$, a synchronization command is issued, and the two inverters synchronize instantaneously. After successful synchronization, Circuit Breaker 1 is manually closed to physically connect the two inverters. During the subsequent power redistribution period, the power ratio shifts from 1:1.5 into 1:1 and then reverts. At time $t_3$, a grid resynchronization command is issued, and the inverters synchronize with the grid instantly. Circuit Breaker 4 is then closed to connect both GFM inverters to the grid. Once the grid-tied operation is verified, Circuit Breaker 4 is manually open to disconnect the inverters from the grid. Finally, Circuit Breaker 1 is opened, preparing the inverters for shutdown. This sequence validates the GFM inverters' ultrafast black start, as well as their islanded and grid-tied modes. The experimental results demonstrate the proposed control capability for instantaneous synchronization and stable, fast, and seamless transitions between islanded and grid-tied modes. The corresponding waveforms and transients are shown below.

- *Ultrafast black start*

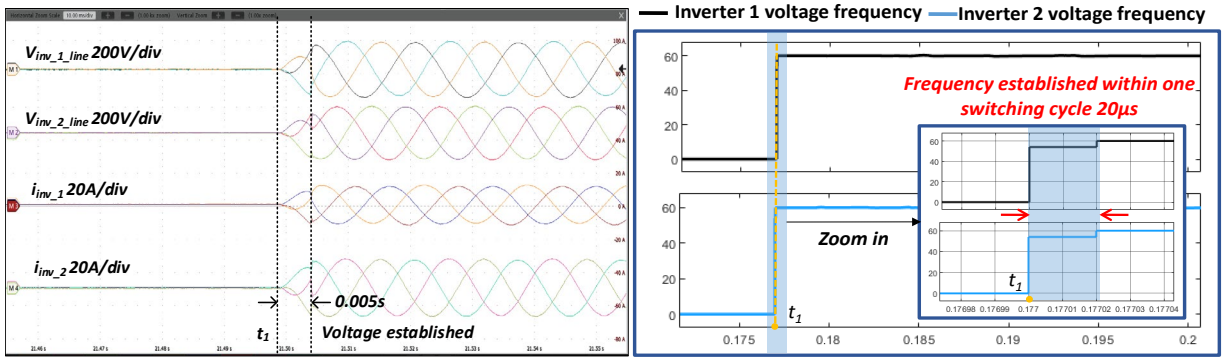


(a) black start transient (b) *frequency establishment*

Fig. 10-6: Two GFM inverters ultrafast black start.

Figure 10-6 shows the zoomed-in black start waveforms. Both voltage and current begin ramping up from time $t_1$. The voltage gradually increases toward its predefined reference value, with the current responding accordingly. Once the voltage reaches the reference,

the system settles at a steady-state condition, where both voltage and current stabilize. Figure 10-6 (a) demonstrates that the voltage is established within *5ms*, while Figure 10-6 (b) shows that the frequency reaches its set point within a single switching cycle (20μs).

- *Two-inverter synchronization*

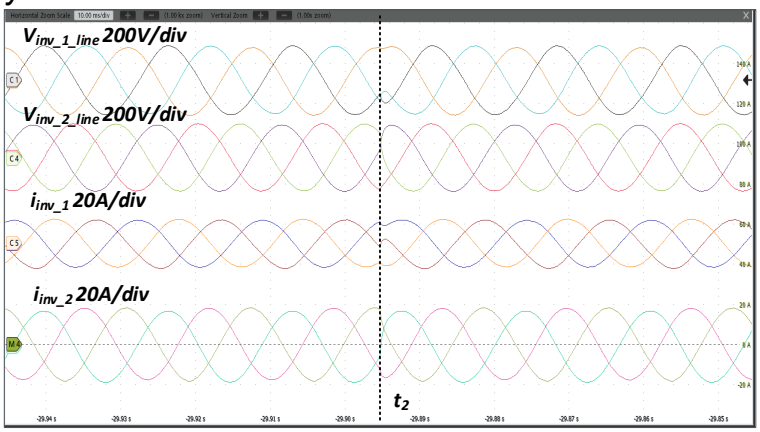


(a) Synchronization transient at $t_2$

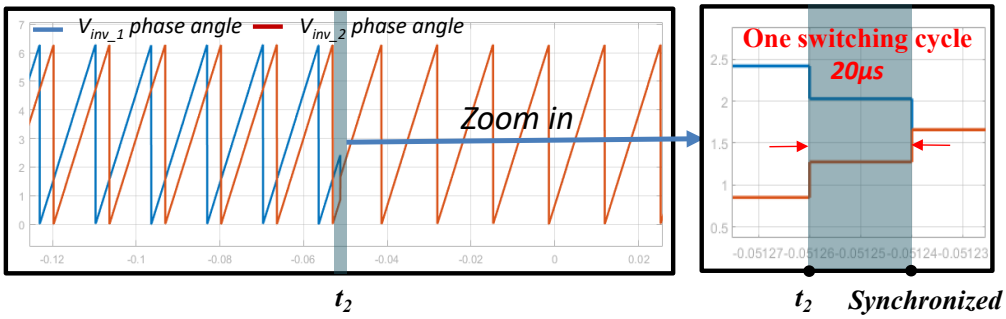


(b) phase angle transient at $t_2$.

Fig. 10-7: Two GFM inverters synchronization process.

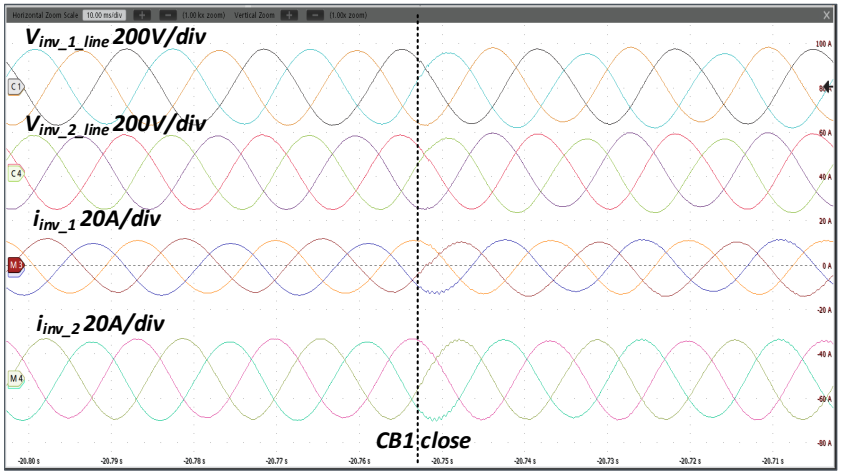


Fig. 10-8: CB1 closing.

Figure 10-7 (a) presents a zoomed-in view of the waveforms at time $t_2$ moment. The two inverters synchronize instantaneously when the synchronization command is issued. As shown in Figure 10-7 (b), the proposed deadbeat control achieves synchronization within

a single switching cycle, which is 20μs. Notably, there is no current or voltage overshoot during the synchronization transient.
Figure 10-8 illustrates the moment when Circuit Breaker 1 is manually closed. Since the two inverters are already synchronized, the connection is seamless, with no observable current or voltage overshoot.

- *GFM Inverters at islanded mode: Power redistribution*

Figure 10-9 shows the power redistribution process between the two GFM inverters during islanded mode, where the power ratio shifts from 1:1.5 to 1:1, and then returns. The entire transition is smooth, with negligible current or voltage overshoot.

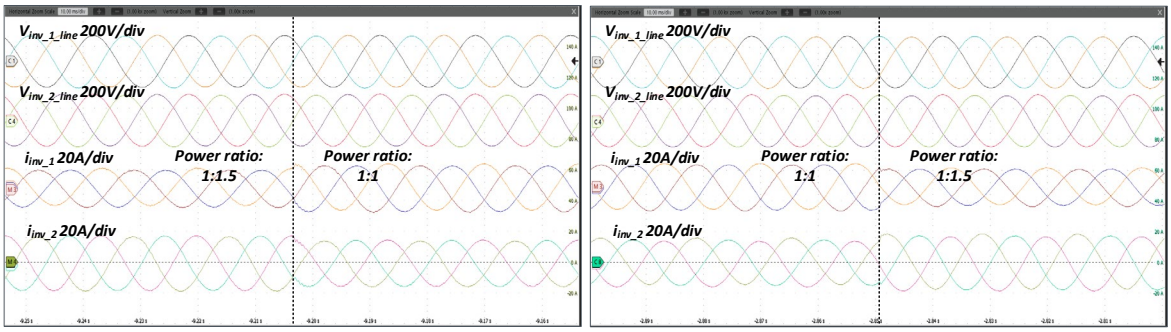


Fig. 10-9: Power redistribution between two GFM inverters during islanded mode.

- *Reconnection to the Grid*

To demonstrate the fast response of the deadbeat based GFM control, Figure 10-10 shows the dynamic performance of the voltage and current waveforms, along with the phase angle, when the grid resynchronization command is issued. As shown in Figure 10-10 (b), the blue curve represents the phase angle of the grid phase A voltage, while the red curve represents the phase angle of the PCC phase A voltage. These curves are derived from experimental data. Before $t_3$, the inverter and grid are not synchronized, resulting in a deviation between two phase angle curves.
Once the synchronization command is issued at $t_3$, the GFM inverters synchronize with the grid within a single cycle, as shown in the right-hand plot. The transient completes within one switching cycle (20 μs), demonstrating the ultrafast dynamic response capability of the proposed deadbeat GFM control.

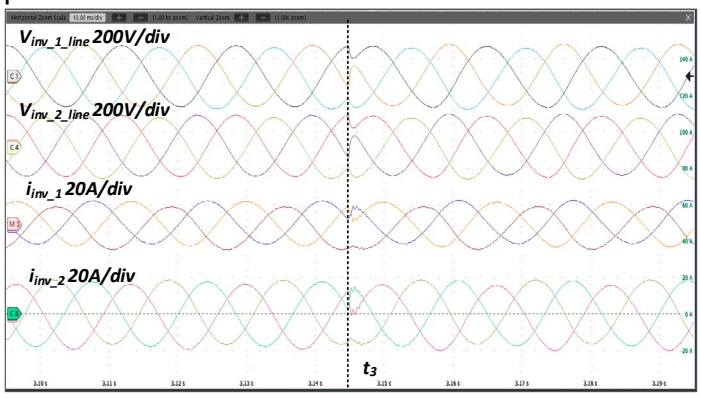


(a) Grid synchronization transient at $t_3$;

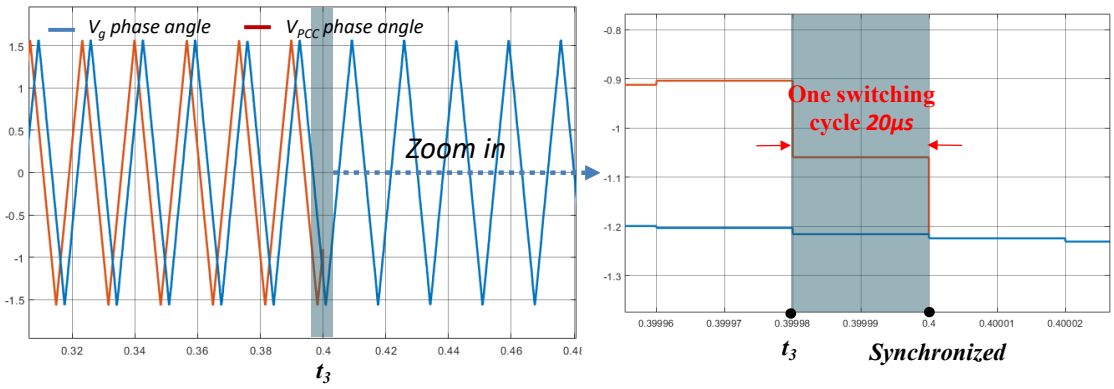


(b) phase angle transient at $t_3$.
Fig. 10-10: Grid synchronization of two GFM inverters

- *Two GFM inverters at grid-connected mode*

Figure 10-11 shows the moment when the Circuit Breaker 4 is closed, smoothly connecting the two inverters to the grid. FFT analysis indicates that the THD of the inverter currents during grid-tied operation was 2.06% and 1.96% for inverter 1 and inverter 2. These low THD values validate the effectiveness of the proposed deadbeat-based GFM control.

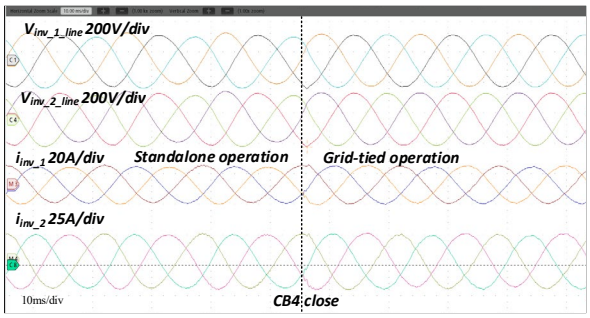


(a) islanded to grid-connected waveforms (b) Current FFT at grid-connected mode
Fig. 10-11: CB 4 closing, GFM inverters transients to grid-tied mode.

- *Disconnected from the grid and shutdown*

After operating in grid-tied mode, CB 4 is opened, disconnecting the inverters from the grid. Subsequently, Circuit Breaker 1 is opened, and the two inverters are prepared for shutdown. Figure 10-12 illustrates the shutdown process of both inverters.

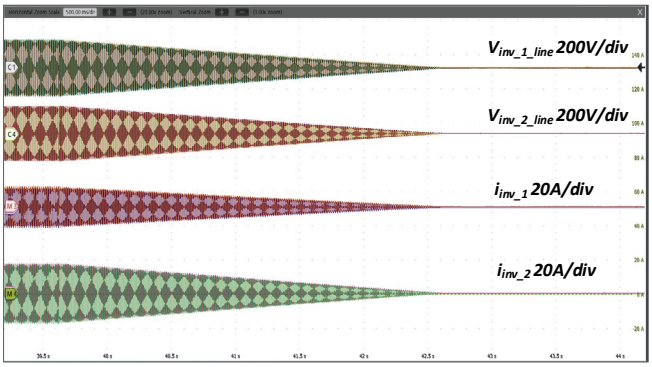


Fig. 10-12: Two GFM inverters shutdown.

10.2.2 Lab validation of VOC-based approach by NU Team

**In this subtask, the NU team made the following progress:**

- ✓ The NEU team paid a two-week visit to the FSU CAPS experimental test facilities to implement and evaluate the black start using the proposed method.
- ✓ Constructed a controller-hardware-in-the-loop (CHIL) test setup for validating uVOC in an ultrafast black start lab testbed.
- ✓ Validated the effectiveness of the uVOC approach for black start through CHIL experiments, demonstrating compliance with black start time requirements in SOPO. The time duration details are shown in the Table 10-1 below.

Table 10-1 Time Comparisons

| Transient Time duration | Support local critical load | Two inverters synchronize | Reconnect to main grid |
|---|---|---|---|
| Requirement | <0.2s | <0.3s | <0.5s |
| Simulation | 0.05s | 0.05s | 0.2s |
| Experiment | 0.08s | 0.016s | 0.016s |

In this task, the Northeastern team implemented the lab validation system at Florida State University (FSU), where we spent two weeks conducting the experiments. The implementation is based on controller-hardware-in-the-loop (CHIL) test setup to test the black start process using the proposed unified virtual oscillator control (uVOC), as illustrated in Fig. 10-13. The PE-Expert 4 system serves as the controller for the two inverters in the black start system. Two PEV modules and two interface boards are used to connect the controller to the Typhoon hardware-in-the-loop (HIL) 606 real-time system. Typhoon HIL 606 executes the programmed black start circuits, receives PWM signals generated by the PE-Expert 4 controller, and outputs the necessary analog signals for closed-loop control and system observation.

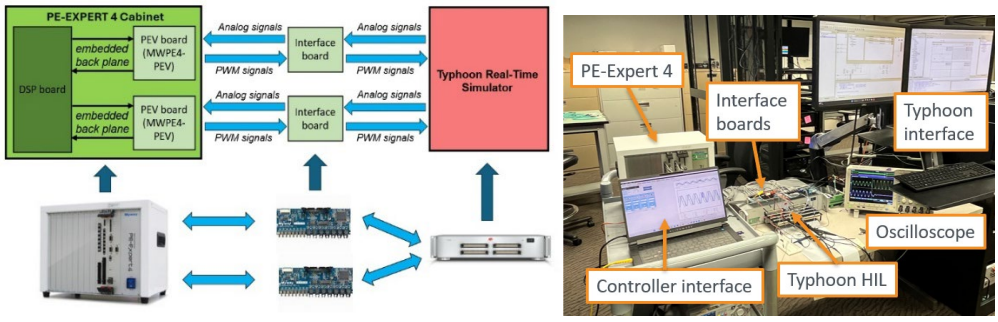


Fig. 10-13: The CHIL test setup

The uVOC essentially mimics the dynamics of coupled nonlinear oscillators. Therefore, to execute the control algorithm in DSP controller in PE-Expert 4, the fourth-order Runge-Kutta (RK4) method is employed to discretize the oscillator and is implemented in C code. The fourth-order Runge-Kutta (RK4) method is a numerical technique for solving nonlinear differential equations with higher accuracy than the traditional Zero-Order Hold (ZOH) method, especially in low sampling frequencies. The block diagram of the black start system embedded in Typhoon HIL system is shown in Fig. 10-14, and the test timeline is shown in Fig. 10-15. Fig. 10-14 also shows the measuring locations for results shown in Fig. 10-16 and Fig. 10-17.

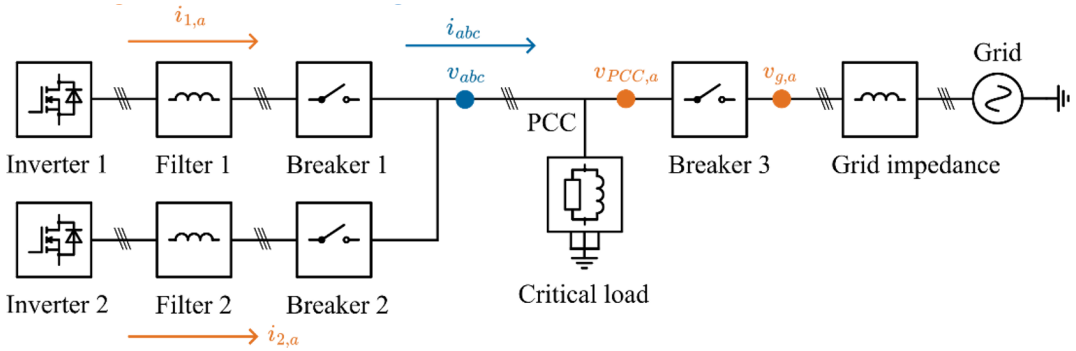


Fig. 10-14: The block diagram of the baseline black start system implemented in Typhoon HIL, along with the measurement locations for lab experiment.

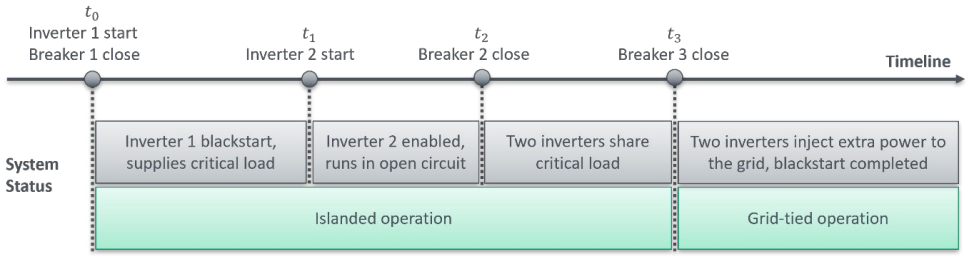


Fig. 10-15: The baseline timeline of the black start sequence.

Several test cases for the VOC under black start process are conducted, which are:

- Two identical inverters with weak grid.
- Two identical inverters with stiff grid.
- Two non-identical inverters with stiff grid.

The parameters used in the CHIL test for the black start are shown in Table 10-2, and the CHIL test results are shown in Fig. 10-16 and Fig. 10-17. In Fig. 10-17, when capturing the three-phase waveforms, only phases A and C were measured directly using the oscilloscope. As shown in Fig. 10-16 (a), Inverter 1 supplies the load and establishes the PCC voltage within approximately five fundamental cycles (~80 ms), which is below the

Table 10-2 Specifications of black start system

| Location | Parameter | Description | Value |
|---|---|---|---|
| Inverters | $V_{DC}$ | DC voltage | 400V |
| | $f_s$ | Switching frequency | 20kHz |
| | $S_{rated,1}$ | Inverter 1 rated power | 10kVAR |
| | $S_{rated,2}$ | Inverter 2 rated power | 10kVAR |
| | $L_{f1}(R_{f1})$ | Inverter 1 filter inductance and resistance | 600uH (50mOhm) |
| | $L_{f2}(R_{f2})$ | Inverter 2 filter inductance and resistance | 800uH (50mOhm) |
| Local load | $P_L$ | Local load power dissipation | 5kW |
| Grid | $L_g(R_g)$ | Grid side inductance and resistance | 0H (0Ohm) |
| | $V_g$ | Grid phase nominal voltage | 100Vrms |
| | $f_{nom}$ | Grid frequency | 60Hz |

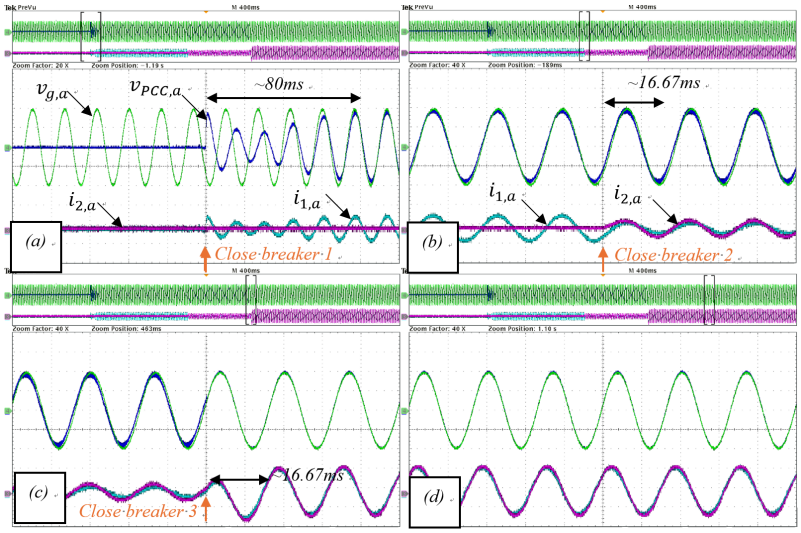


Fig. 10-16: Black start CHIL results. Only phase A is presented. (a) The black start transients for single inverter supplying local critical load. (b) The synchronization transients for two inverters, two inverters share the local load. (c) Transients for grid reconnection. (d) Steady state operation for grid-tied inverters.

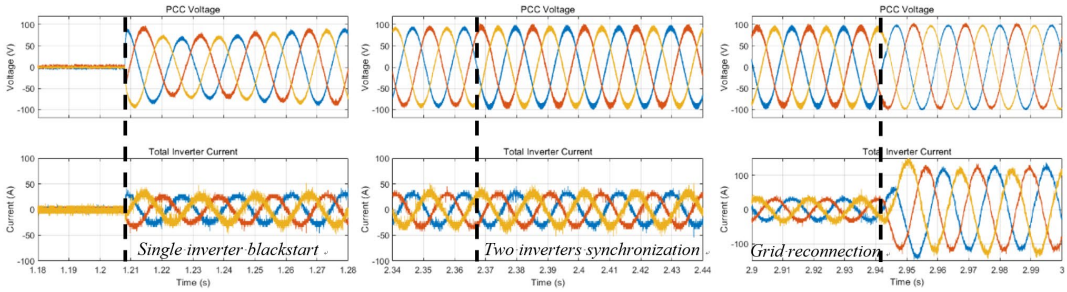


Fig. 10-17: Three-phase PCC voltage and total inverter output current

required time of 0.2s. During this period, it also synchronizes with the grid voltage, even though the grid breaker remains open. There is no inrush current observed. Similarly, in Fig. 10-16 (b), when the second inverter connects to the PCC, there is no noticeable disturbance, and the load sharing is smooth, finished within one fundamental cycle (~16 ms), which is below the required transient time of 0.3s. In Fig. 10-16 (c), upon closing the grid breaker, the PCC voltage seamlessly merges with the grid voltage. Both inverters deliver their rated power, and reached the steady state within one fundamental cycle (~16 ms). Fig. 10-16 (d) illustrates the steady-state operation of uVOC when connected to the grid, and the whole black start process is completed. The overall black start time can be as short as the above three transient time combined, which is around 120ms, which satisfies the required time of 1s of full black start process. Fig. 10-17 presents the three-phase PCC voltage waveforms, and the total output current measured during the black start process. Throughout the three breaker closure events, the PCC voltage builds up rapidly using the proposed uVOC method, with only minimal disturbances observed during each transition. The results in Fig. 10-16 and Fig. 10-17 collectively demonstrate the effectiveness of the proposed uVOC strategy in executing a stable and ultrafast black start procedure, achieving fast PCC voltage restoration and inverter synchronization, even in situations involving non-identical inverters and a stiff grid.

The lab evaluations of developed control methods are summarized in Table 10-3 with Siemens method as base line. Bot VOC method and deadbeat method can achieve ultrafast black start, nearly no steady state errors. The deadbeat approach has advantages to achieve synchronization within switching cycle, both methods can achieve stability for stiff grid condition.

Table 10-3: Lab Evaluations of Developed Grid-Forming Control methods in Hybrid IBR Systems

| Feature | Siemens (Droop-Based GFM) | Virtual Oscillator Control (VOC) | Deadbeat-Based GFM |
|---|---|---|---|
| **Black Start** | | | |
| • *Voltage Establishment Time* | ~5 s | <100 ms | <5 ms |
| • *Steady-State Voltage Error* | <1% | Negligible | Negligible |
| **Islanded Operation** | | | |
| • *Inverter Synchronization Time* | ~1 s | <16 ms after controller enable | Instantaneous (1 switching cycle) |
| • *Synchronization Transient Performance* | Smooth but slow | Minimal inrush current/voltage | Minimal inrush current/voltage |
| • *Power Sharing Capability* | Via droop characteristics | Via shared PCC connection | Dynamically controlled redistribution |
| **Grid-Tied Operation** | | | |
| • *Grid Synchronization Time* | N/A | Pre-synchronized during black start; total <16 ms | Instantaneous (1 switching cycle) |
| • *Grid Synchronization Transients* | N/A | Smooth reconnection | No current or voltage overshoot |
| • *Power Sharing Capability* | N/A | Full rated power; supports grid and local loads | Dynamic power redistribution via control |
| • *Strong Grid Compatibility* | N/A | Stable under weak and strong grid | Stable under weak and strong grid |

## 4. Significant Accomplishments and Conclusions

**FSU: A number of key accomplishments have been achieved in this project:**

- A **virtual resistance-based control method –** an advanced virtual impedance method**,** ensures fast grid following and synchronization capabilities, adds passivity to the overall system to affiliate the stability under weak grid condition. The other advantages of of VR method include the independency of the voltage sensors at the point of common coupling (PCC), and the removal of the traditional phase-locked loop (PLL) circuits.

- A **novel deadbeat-based GFL and GFM control strategy** enabling ultrafast black start capability and instantaneous synchronization for multi-paralleled inverters without PLL loop and voltage sensors. The stability of GFL mode under weak grid and GFM mode under stiff grid were proved through Lyapunov method.
- **Instantaneous synchronization** between inverters and with the grid was achieved, resulting in **seamless transitions** between islanded and grid-connected modes. Notably, voltage and current overshoots during synchronization transients were effectively eliminated.
- A **built-in current-limiting** mechanism was integrated into the control scheme, providing robust low-voltage ride-through (LVRT) performance without requiring additional control mode switching. This enhances overall system resilience and simplifies control architecture.
- Experimental validation confirmed the **technical effectiveness and practical feasibility** of the proposed approach, reinforcing its readiness for deployment in advanced microgrid and distributed energy systems.
- **a 100 kW IBR testbed** was built for our local utility partner to investigate UUCC for hybrid PV+Battery plant in the near future.
- **4 patents filed and 7 journal papers published.**

**NU team has achieved the following accomplishments:**

- **Battery sizing**: We proposed a dynamic programming (DP)-based scheduling method for battery energy storage systems (BESS) to replace internal combustion (IC) units in grid reserve applications, enhancing system flexibility and increasing BESS revenue compared to traditional approaches. It introduces a capacity sweeping technique that optimizes BESS operation, sometimes leading to counterintuitive sizing decisions that outperform conventional methods. Additionally, the research addresses the challenge of power fluctuations from PV plants by evaluating the power and energy requirements of collocated BESS for output smoothing and ramp rate control. The findings aim to establish a standardized approach for BESS sizing, supporting more stable and efficient integration of solar energy into the grid.
- **Ultrafast black start using unified VOC-based IBRs:** We achieved ultrafast black start within 1s using unified VOC for inverter control. A thorough analysis was conducted to identify key barriers to achieving fast and stable dynamics during the black start process, emphasizing that the control strategy must address challenges across all transients and steady-state stages while meeting GFM and microgrid standards. Based on this understanding, a baseline test model was defined to validate the proposed method. The proposed method was validated through both simulation and hardware experiments across various power ratings and different DC sources with/without DCDC converter stage, demonstrating the generalization, robustness, and effectiveness of the control algorithm. This confirms the capability of ultrafast restoring power after a blackout using appropriate control of a PV-battery hybrid plant.

This project achieved significant technical breakthroughs in control strategies, system coordination, and experimental validation of hybrid photovoltaic (PV) and battery energy storage plants using inverter-based resources (IBRs). The work directly advances the operational capabilities of next-generation inverter-dominated power systems and contributes foundational knowledge toward grid resilience, black start readiness, and seamless hybrid control.

Key accomplishments include:

**Unified Universal Control and Coordination (UUCC)**

- The project developed and validated a Unified Universal Control and Coordination (UUCC) framework that enables stable operation of hybrid PV + battery plants in all modes—grid-tied, islanded, and transitional.
- The UUCC architecture is compatible with both grid-forming (GFM) and grid-following (GFL) inverters, and black start.

**Ultrafast Black Start and Synchronization**

- The control algorithms achieved **ultrafast black start capabilities**, with voltage stabilization in less than **0.2 seconds** and full synchronization (including load pick-up and grid reconnection) within **1 second**.
- This performance was achieved even under complex scenarios involving **multiple paralleled inverters operating in both GFL and GFM modes**, and when starting from a dead bus condition.

**Deadbeat and Virtual Oscillator Control Innovations**

- A **novel deadbeat-based GFM control strategy** was introduced, enabling instantaneous synchronization between inverters and seamless transitions between operating modes. Voltage and current overshoots during mode transitions were eliminated.
- An enhanced **virtual oscillator control (VOC)** algorithm with **predictive current feedback** was developed to enable synchronization without output current—a critical advancement for zero-injection black start and connection stability.

**Virtual Resistance-Based Methods**

- A **virtual resistance (VR)-based method** was designed to improve grid-following performance under weak grid conditions. The method adds passivity to enhance system stability, while avoiding the need for traditional PLL circuits or PCC voltage sensors. This greatly simplifies implementation in real-world systems.

**Built-in Low-Voltage Ride-Through (LVRT) and Current Limiting**

- The control strategies include integrated **current-limiting and LVRT features**, which maintain stability during disturbances without the need for mode-switching logic—improving resilience and reliability in both islanded and grid-tied operations.

**Battery Energy Storage Sizing and Optimization**

- The project developed a **dynamic programming (DP)-based scheduling framework** for battery energy storage systems (BESS), enabling the replacement of internal combustion units for reserve power applications. This approach optimizes operational flexibility and long-term revenue potential.
- A **standardized method for BESS sizing** was also proposed, particularly for PV output smoothing and ramp rate control. Reliability-aware sizing strategies were developed and validated on a 20 MW PV plant case study.

**Hardware Testbeds and Commercial Controller Validation**

- The control strategies were validated across multiple platforms:
    - **Custom hardware testbeds** (up to 20 kW), built specifically for this project and intended for further research and development of these control technologies, providing future validation capabilities;
    - A newly constructed **100 kW IBR testbed shown below**, intended for future research and development of these control technologies, and future field demonstrations with utility and industrial partners;

    - **Commercial microgrid controllers**, where the UUCC black start and GFM-GFL coordination logic was successfully deployed and benchmarked;
    - **Real-time and offline simulations** representing realistic PV + battery plant architectures.

These accomplishments represent a **transformational leap in IBR capability**—from slow and rigid responses to **agile, fast, and coordinated behavior**, capable of supporting the grid under normal and emergency conditions. The innovations pave the way for IBRs to deliver services traditionally associated with synchronous machines, including black start, fault ride-through, and transformer energization, but with faster response and greater flexibility.

In conclusion, the project demonstrates the feasibility of using hybrid inverter-based plants as **primary agents in system restoration and grid modernization efforts**, offering a robust platform for future deployment in utility-scale and community-scale microgrids. The groundwork laid by this project will be essential for DOE priorities in resilience, decarbonization, and clean energy integration.

## 5. Path Forward

The technologies developed under this project—particularly the Unified Universal Control and Coordination (UUCC) framework for hybrid PV + battery inverter-based systems—represent a significant advancement in fast black start capability, coordinated GFM/GFL operation, and system resilience. However, additional research and development steps are necessary to transition these innovations from laboratory-scale validation to field deployment and commercial adoption.

**Planned and Recommended R&D Directions**

1. **Scaling to Higher-Power Demonstrations**
   The most critical next step is to validate the UUCC strategies and associated control algorithms on larger power platforms beyond the current ≤20 kW scale.
   - A near-term opportunity is to **scale testing to the 100 kW IBR testbed** developed at Florida State University (FSU), enabling more representative grid-interaction studies under realistic loading and dynamic conditions.
   - Further expansion to **hundreds of kilowatts or megawatt-scale testbeds**, possibly in collaboration with national labs or utility partners, is essential for derisking the technology for utility or commercial use.
2. **Further Development of VR-Based Techniques for Grid-Forming (GFM) Control**
   The virtual resistance methods demonstrated for GFL control show promise for broader application and could be extended to GFM controls in the future research.
3. **Hybrid Plant Demonstration with Commercial Controllers**
   The black start algorithm developed by Siemens and implemented in a commercial microgrid controller was used in this project as a performance benchmark. A logical path forward is to **conduct coordinated hybrid power plant demonstrations** using this controller alongside UUCC-based controls—combining GFL and GFM inverters under grid-connected and islanded modes. This could help refine interoperability requirements and accelerate market readiness.
4. **UUCC Commercialization Opportunities**
   The modular, standards-agnostic nature of the UUCC framework positions it well for **integration into commercial microgrid and hybrid plant controllers**, particularly in markets seeking enhanced resiliency and grid-forming capabilities. Potential commercialization partners include Siemens and other inverter or energy management system vendors. Strategic collaboration for licensing,

product integration, or technology spinout could accelerate adoption, particularly in applications like remote microgrids, critical infrastructure, or resilience hubs.

5. **Exploration of Three-Port Converter Architectures**

   A promising future research is the application of these controls to three-port converter architectures, integrating AC output/input, PV DC output, and battery or ultracapacitor DC output/input within a single converter. Such integration could improve system stability, dynamic response, and reliability, while reducing losses and lowering capital cost per unit through shared packaging and dual-function components. Locating energy storage directly on the DC bus may provide a functional equivalent to electromechanical inertia, potentially reducing spinning reserve requirements for smaller, dispersed units due to their lower incremental risk of loss.

**Remaining Technical Risks and Barriers to Commercialization**

- **Scalability and Certification**: The UUCC has been validated at laboratory scale, but field-level performance—including protection coordination, latency impacts, and fault response—remains to be fully demonstrated. Certification to UL and IEEE standards (e.g., IEEE 1547-2018 for GFM inverters) is also a necessary step before wide-scale commercial adoption.
- **Interoperability with Legacy Systems**: Ensuring the UUCC methods work seamlessly with a wide range of inverter hardware and legacy utility infrastructure will require additional compatibility testing and potential controller firmware customization.
- **Economic Justification and Market Awareness**: Although the technical value is high, successful commercialization will also depend on demonstrating economic benefits such as faster grid restoration, reduced reliance on spinning reserves, or simplified system design. Building compelling business cases and increasing awareness in utility and EPC (Engineering, Procurement and Construction) communities will be important for market traction.

## 6. Products

- **Filed patents**
  1. A Method of Instant Startup and Grid Synchronization of Inverter Based Resources. Filed on Oct. 30, 2023. Provisional application number 63/594,180.
  2. A Method of Instant Black Start and Transformer Energization using Inverter Based Resources. Filed on Oct. 30, 2023. Provisional application number 63/594,177.
  3. Instantaneous Synchronization and Low Voltage Ride Through Methods for Grid-Tied Power Inverters without using Phase-Locked-Loop. Nonprovisional Application No. 19/077,651, March 12, 2025

4. Switching Cycle-Based Unified Control for Paralleled GFM Inverters with Ultrafast Black Start and Instantaneous Seamless Transitions Between Islanded and Grid-Tied Operation. Filed June 6, 2025. Provisional Application No. 63/818,797.

- **Journal paper**
  1. F. Z. Peng, C. -C. Liu, Y. Li, A. K. Jain and D. Vinnikov, "Envisioning the Future Renewable and Resilient Energy Grids—A Power Grid Revolution Enabled by Renewables, Energy Storage, and Energy Electronics," in IEEE Journal of Emerging and Selected Topics in Industrial Electronics, vol. 5, no. 1, pp. 8-26, Jan. 2024, doi: 10.1109/JESTIE.2023.3343291.
  2. Y. He, Y. Li, B. Zhou and F. Z. Peng, "Switching-Cycle-Based Startup for Grid-Connected Inverters," in IEEE Journal of Emerging and Selected Topics in Industrial Electronics, vol. 5, no. 3, pp. 950-961, July 2024, doi: 10.1109/JESTIE.2024.3365031.
  3. Peng, F.Z. Impedance sources (Z sources) with inherent fault protection for resilient and fire-free electricity grids. *Sci Rep* **14**, 3062 (2024). https://doi.org/10.1038/s41598-024-53452-y
  4. X. Quan, X. Dong and H. Li, "A Stable and Ultrafast Control for Multi-Parallel Grid-tied SiC Inverters with LVRT Capability Considering Cable Impedance," in IEEE Transactions on Power Electronics, doi: 10.1109/TPEL.2025.3566287.
  5. Sina Ameli, Ayobami Olajube, Olugbenga Moses Anubi, Robust Adaptive Control for Large-scale Inverter-based Resources with Partial and Complete Loss of Inverters, IFAC-PapersOnLine, Volume 56, Issue 3, 2023, Pages 211-216.
  6. O. M. Anubi and S. Ameli, "Robust Stabilization of Inverter-Based Resources Using Virtual Resistance-Based Control," in IEEE Control Systems Letters, vol. 6, pp. 3295-3300, 2022.
  7. S. Ameli, O. M. Anubi and F. Peng, "Robust Optimal Control of Inverter-Based Resources Under Grid-Forming Operation," in IEEE Transactions on Control Systems Technology, Early access.

- **Conference paper**
  1. Y. He, Y. Li, B. Zhou, Y. Zou and F. Z. Peng, "An Ultrafast Inrush-Current-Free Startup Method for Grid-tie Inverter without Voltage Sensors," 2023 IEEE Applied Power Electronics Conference and Exposition (APEC), Orlando, FL, USA, 2023, pp. 2874-2880, doi: 10.1109/APEC43580.2023.10131356.
  2. U. Selvarasu, M. Amirabadi, Y. Li, C. Crow and B. Lehman, "DP-Based Optimization of BESS to Substitute RICE Reserves for Improved Economic Benefits," 2023 IEEE Energy Conversion Congress and Exposition (ECCE), Nashville, TN, USA, 2023, pp. 188-194, doi: 10.1109/ECCE53617.2023.10362257.
  3. S. Wang, M. Amirabadi and B. Lehman, "A Real-Time Degradation Estimation Approach for Batteries in PV and Battery Hybrid Plant

Operation," 2023 IEEE Energy Conversion Congress and Exposition (ECCE), Nashville, TN, USA, 2023, pp. 493-499, doi: 10.1109/ECCE53617.2023.10362788.
4. Y. He, Y. Li, B. Zhou and F. Z. Peng, "Switching-Cycle-Based Startup for Grid-tied Inverters," 2023 IEEE 17th International Conference on Compatibility, Power Electronics and Power Engineering (CPE-POWERENG), Tallinn, Estonia, 2023, pp. 1-5, doi: 10.1109/CPE-POWERENG58103.2023.10227483.
5. Y. He, B. Zhou, Y. Li and F. Z. Peng, "Impedance Modeling and Stability Analysis for the PLL-less and Voltage Sensor-less Grid-tied Converters," 2023 IEEE 17th International Conference on Compatibility, Power Electronics and Power Engineering (CPE-POWERENG), Tallinn, Estonia, 2023, pp. 1-5, doi: 10.1109/CPE-POWERENG58103.2023.10227472.
6. Y. He et al., "Instant Startup and Grid Synchronization of Inverter Based Resources," 2024 IEEE Applied Power Electronics Conference and Exposition (APEC), Long Beach, CA, USA, 2024, pp. 1647-1653, doi: 10.1109/APEC48139.2024.10509411.
7. S. Wang, U. Selvarasu, M. Amirabadi, Y. Li and B. Lehman, "Enhanced Startup and Synchronization Transients for Virtual-Oscillator Grid-Tie Inverters Using Predictive Feedback-Based Method," 2024 IEEE Energy Conversion Congress and Exposition (ECCE), Phoenix, AZ, USA, 2024, pp. 247-254, doi: 10.1109/ECCE55643.2024.10861098.
8. U. Selvarasu, M. Amirabadi, Y. Li, C. Crow and B. Lehman, "BESS Sizing for PV Power Smoothing," 2024 IEEE Energy Conversion Congress and Exposition (ECCE), Phoenix, AZ, USA, 2024, pp. 546-552, doi: 10.1109/ECCE55643.2024.10860983.
9. X. Quan, X. Dong, M. Bosworth and H. Li, "Equivalent Circuit Model and Stability Analysis of Multi-Paralleled Grid-Tied SiC Inverters with Low Voltage Ride-Through Capability," 2024 IEEE Energy Conversion Congress and Exposition (ECCE), Phoenix, AZ, USA, 2024, pp. 3685-3691, doi: 10.1109/ECCE55643.2024.10861552.
10. Shumeng Wang, et al., “Unified Virtual Oscillator Based Grid-Forming Control for Fast Blackstart,” Accepted by 2025 IEEE Energy Conversion Congress and Exposition (ECCE)

- **Poster for DOE AI/ML workshop (Alexandria, VA, Oct. 29-Nov. 1)**
  1. Artificial Intelligence-based PV Power Forecast and Energy Management Systems of Power Plants and Utility-Scaled Hybrid PV+ BESS

## 7. Project Team and Roles

1. Fang Peng: Professor at Florida State University (FSU), responsible for project management, PI of contract in BP1 and leading research in VR approach;
2. Hui “Helen” Li: Professor at FSU, project PI in BP2, responsible for project management and leading the FSU research in deadbeat approach
3. Olugbenga Anubi: Associate Professor at FSU studying stability for UUCCs

4. Yuan Li: Assistant Professor at FSU, leading team on outer loop supervisory control and forecasting during BP1;
5. Mary Jo Spector: Director of Research Facilities Design, Construction, and Maintenance at FSU leading the construction of the FSU PV array.
6. John Hauer: Facility manager, FSU Center for Advanced Power Systems (CAPS), assistanting 100kW IBR testbed installation

……..

7. Michael Ohlsen: Manager | Clean Energy & Resource Planning, City of Tallahassee (COT) utilities, providing utility guidance installing 100 kW PV based IBR testbed
8. Caleb Crow: Clean Energy& Resource Planning Engineer II, City of Tallahassee (COT) utilities

……

9. Brad Lehman: Professor at NU, responsible for project management, decision-making and advising Ph.D. students of NU group.
10. Mahshid Amirabadi: Associate Professor at Northeastern University, responsible for project management, decision-making and advising Ph.D. students of NU group.

……

11. Nan Xue: Team lead at Siemens performing baseline analysis on commercial inverters in BP1
12. Xiaofan Wu: Siemens researcher performing baseline analysis on commercial inverters in BP2
13. Karl Fetzer: Staff Research Scientist, Siemens, implementing black start in microgrid controller for UUCCs
14. Naresh Nandola: Staff Research Scientist , Siemens, implementing black start in microgrid controller for UUCCs

……..

15. Akanksha Singh: Researcher at NREL in BP1 performing analysis for 1MW microgrid

……..

16. Hector Akuta: Ph.D. student FSU for outer loop control and forecast predictions;
17. Sina Ameli: Ph.D. student at FSU studying stability for UUCCs
18. Xiaofeng Dong: Ph.D. student at FSU studying deadbeat-based GFL&GFM control for UUCCs
19. Yuchen He: Ph.D. student FSU developing VR methods
20. Xuli Quan: Ph.D. student at FSU studying ultrafast black start and deadbeat-based GFL/GFM method for multiple inverter units
21. Xiaorui Liu: Ph.D. student at FSU studying outloop control and microgrid controller for UUCCs
22. Minoo Mohebbifar: Ph.D. student at Northeastern University, focused on switching-cycle-based startup in parallel inverter system.
23. Ayobami Olajube: Ph.D. student at FSU studying stability for UUCCs
24. Uthandi Selvarasu: Ph.D. student at Northeastern University, focused on droop-based baseline method for black start.

25. Shumeng Wang: Ph.D. student at Northeastern University, focused on VOC-based method for ultrafast black start.
26. Bokang Zhou: Ph.D. student FSU developing VR methods
27. Jinli Zhu: Postdoctoral scholar FSU developing outer loop control and VR methods in BP2
28. Yuntao Zou: Postdoctoral scholar FSU developing VR methods and GFL method in UUCC systems in BP1

## 8. References

[1] B. B. Johnson, M. Sinha, N. G. Ainsworth, F. Dörfler and S. V. Dhople, "Synthesizing Virtual Oscillators to Control Islanded Inverters," in IEEE Transactions on Power Electronics, vol. 31, no. 8, pp. 6002-6015, Aug. 2016, doi: 10.1109/TPEL.2015.2497217.

[2] M. Lu, S. Dhople and B. Johnson, "Benchmarking Nonlinear Oscillators for Grid-Forming Inverter Control," in IEEE Transactions on Power Electronics, vol. 37, no. 9, pp. 10250-10266, Sept. 2022, doi: 10.1109/TPEL.2022.3162530.

[3] M. Lu, S. Dutta, V. Purba, S. Dhople and B. Johnson, "A Grid-compatible Virtual Oscillator Controller: Analysis and Design," 2019 IEEE Energy Conversion Congress and Exposition (ECCE), Baltimore, MD, USA, 2019, pp. 2643-2649, doi: 10.1109/ECCE.2019.8913128.

[4] L. Kong, Y. Xue, L. Qiao and F. Wang, "Enhanced Synchronization Stability of Grid-Forming Inverters With Passivity-Based Virtual Oscillator Control," in IEEE Transactions on Power Electronics, vol. 37, no. 12, pp. 14141-14156, Dec. 2022, doi: 10.1109/TPEL.2022.3187402.

[5] M. Lu, R. Mallik, B. Johnson and S. Dhople, "Dispatchable Virtual-oscillator-controlled Inverters with Current-limiting and MPPT Capabilities," 2021 IEEE Energy Conversion Congress and Exposition (ECCE), Vancouver, BC, Canada, 2021, pp. 3316-3323, doi: 10.1109/ECCE47101.2021.9595530.

[6] Z. Zeng, J. Fan, Y. Sun, S. Wang and D. Yang, "A Dispatchable Virtual Oscillator Controller in the dq Frame With Enhanced Grid-Forming Power Reference Tracking Capability," in IEEE Transactions on Power Electronics, vol. 40, no. 8, pp. 10973-10987, Aug. 2025, doi: 10.1109/TPEL.2025.3556325.

[7] M. A. Awal and I. Husain, "Unified Virtual Oscillator Control for Grid-Forming and Grid-Following Converters," in IEEE Journal of Emerging and Selected Topics in Power Electronics, vol. 9, no. 4, pp. 4573-4586, Aug. 2021, doi: 10.1109/JESTPE.2020.3025748.

[8] M. Lu, S. Dutta, V. Purba, S. Dhople and B. Johnson, "A Pre-synchronization Strategy for Grid-forming Virtual Oscillator Controlled Inverters," 2020 IEEE Energy Conversion Congress and Exposition (ECCE), Detroit, MI, USA, 2020, pp. 4308-4313, doi: 10.1109/ECCE44975.2020.9236364.

[9] P. Karamanakos, M. Nahalparvari and T. Geyer, "Fixed Switching Frequency Direct Model Predictive Control With Continuous and Discontinuous Modulation for Grid-Tied Converters With LCL Filters," IEEE Trans. Control Syst. Technol., vol. 29, no. 4, pp. 1503-1518, July 2021.

[10] C. Zheng, T. Dragičević, Z. Zhang, J. Rodriguez and F. Blaabjerg, "Model Predictive Control of LC-Filtered Voltage Source Inverters With Optimal Switching Sequence," IEEE Trans. Power Electron, vol. 36, no. 3, pp. 3422-3436, March 2021.

[11] S. Vazquez, J. Rodriguez,M. Rivera, L. G. Franquelo, andM. Norambuena,"Model predictive control for power converters and drives: Advances and trends," IEEE Trans. Ind. Electron., vol. 64, no. 2, pp. 935–947, Feb. 2017.

[12] M. G. Judewicz, S. A. González, J. R. Fischer, J. F. Martínez and D. O. Carrica, "Inverter-Side Current Control of Grid-Connected Voltage Source Inverters With LCL Filter Based on Generalized Predictive Control," IEEE J. Emerging Sel. Top. Power Electron., vol. 6, no. 4, pp. 1732-1743, Dec. 2018.

[13] J. Castelló, J. M. Espí and R. García-Gil, "A New Generalized Robust Predictive Current Control for Grid-Connected Inverters Compensates Anti-Aliasing Filters Delay," IEEE Trans. Ind. Electron., vol. 63, no. 7, pp. 4485-4494, July 2016.

[14] X. Dong and H. Li, "A PLL-Less Voltage Sensorless Direct Deadbeat Control for a SiC Grid-Tied Inverter With LVRT Capability Under Wide-Range Grid Impedance," IEEE Trans. Power Electron, vol. 38, no. 8, pp. 9469-9481, Aug. 2023.

[15] M. Kermadi et al., "Model-Free Predictive Current Controller for Voltage Source Inverters Using ARX Model and Recursive Least Squares," IEEE Trans. Circuits Syst. II Express Briefs, vol. 71, no. 5, pp. 2619-2623, May 2024.

[16] J. Jongudomkarn, J. Liu and T. Ise, "Virtual Synchronous Generator Control With Reliable Fault Ride-Through Ability: A Solution Based on Finite-Set Model Predictive Control," in IEEE Journal of Emerging and Selected Topics in Power Electronics, vol. 8, no. 4, pp. 3811-3824, Dec. 2020.

[17] Z. Zhang, D. Sun, C. Zhao, Z. Gu and H. Nian, "Enhanced Grid-forming Control Strategy for DFIG Participating in Primary Frequency Regulation Based on Double-layer MPC in Microgrid," in IEEE Transactions on Energy Conversion.

[18] A. Arjomandi-Nezhad, Y. Guo, B. C. Pal and D. Varagnolo, "A Model Predictive Approach for Enhancing Transient Stability of Grid-Forming Converters," in IEEE Transactions on Power Systems, vol. 39, no. 5, pp. 6675-6688, Sept. 2024

[19] S. Niu et al., "A Nonlinear MPC-Based Adaptive Inertia Strategy for Andronov-Hopf Oscillator Controlled Grid-forming Inverters," 2024 IEEE Energy Conversion Congress and Exposition (ECCE), Phoenix, AZ, USA, 2024, pp. 1506-1511.

[20] Z. Chen, X. Pei, M. Yang and L. Peng, "An Adaptive Virtual Resistor (AVR) Control Strategy for Low-Voltage Parallel Inverters," in IEEE Transactions on Power Electronics, vol. 34, no. 1, pp. 863-876, Jan. 2019, doi: 10.1109/TPEL.2018.2815284.

[21] W. Wu et al., "Active damping control of multiple resonances for grid-connected inverter with long transmission cable," 2016 IEEE International Conference on Industrial Technology (ICIT), Taipei, Taiwan, 2016, pp. 263–268, DOI: 10.1109/ICIT.2016.7474762.

[22] Y. Xiang, X. Han, L. Wang, P. Wang and W. Qin, "Resonance characteristics and damping techniques of grid-connected converter with the distributed capacitance of

transmission line," 2018 13th IEEE Conference on Industrial Electronics and Applications (ICIEA), Wuhan, China, 2018, pp. 491–496, DOI: 10.1109/ICIEA.2018.8397767.

[23] S. Zhang, S. Jiang, X. Lu, B. Ge and F. Z. Peng, "Auto-tuning based resonance damping of grid-connected voltage source inverters with long transmission cable," 2013 IEEE Energy Conversion Congress and Exposition, Denver, CO, USA, 2013, pp. 2941–2947, DOI: 10.1109/ECCE.2013.6647084.

[24] "Success Story—Using Renewable Microgrids to Keep the Lights On," July 26, 2023, https://www.energy.gov/eere/solar/articles/success-story-using-renewable-microgrids-keep-lights

[25] "Princeton Resilient Campus", https://www.siemens.com/us/en/products/buildingtechnologies/energy/total-energy-management/case-studies/princeton-resilient-campus.html

[26] "Driving zero fossil fuels for Galápagos", https://www.siemens.com/global/en/products/energy/references/galapagos.html

[27] OM. Anubi, S. Ameli, "Robust Stabilization of Inverter-based Resources using Virtual Resistance-based Control", IEEE Control Systems Letter, vol. 6, pages 3295-3300, 2022.